

# UC San Diego

## UC San Diego Electronic Theses and Dissertations

### Title

Seismic performance of precast concrete dual-shell steel columns for accelerated bridge construction

### Permalink

<https://escholarship.org/uc/item/8kt0p0cx>

### Author

Guerrini, Gabriele

### Publication Date

2014

Peer reviewed|Thesis/dissertation

UNIVERSITY OF CALIFORNIA, SAN DIEGO

**SEISMIC PERFORMANCE OF  
PRECAST CONCRETE DUAL-SHELL STEEL COLUMNS  
FOR ACCELERATED BRIDGE CONSTRUCTION**

A dissertation submitted in partial satisfaction of the requirements for the degree of

Doctor of Philosophy

in

Structural Engineering

by

Gabriele Guerrini

Committee in charge:

Professor José I. Restrepo, Chair  
Professor James H. Fowler  
Professor Peter M. Shearer  
Professor P. Benson Shing  
Professor Chia-Ming Uang

2014

Copyright

Gabriele Guerrini, 2014

All rights reserved

The dissertation of Gabriele Guerrini is approved, and it is acceptable in quality and form for publication on microfilm and electronically:

---

---

---

---

---

Chair

University of California, San Diego

2014

# **DEDICATION**

*To my Family and Friends*

# TABLE OF CONTENTS

<b>SIGNATURE PAGE.....</b>	<b>iii</b>
<b>DEDICATION.....</b>	<b>iv</b>
<b>TABLE OF CONTENTS .....</b>	<b>v</b>
<b>LIST OF TABLES.....</b>	<b>x</b>
<b>LIST OF FIGURES.....</b>	<b>xi</b>
<b>ACKNOWLEDGMENTS .....</b>	<b>xiv</b>
<b>VITA .....</b>	<b>xvii</b>
<b>ABSTRACT OF THE DISSERTATION.....</b>	<b>xxi</b>
<b>CHAPTER 1 INTRODUCTION .....</b>	<b>1</b>
1.1. General Considerations .....	1
1.2. Background on Self-Centering/Rocking Systems .....	3
1.3. Background on Concrete-Filled Tube Columns .....	5
<b>CHAPTER 2 SELF-CENTERING DUAL-SHELL COLUMNS: FEATURES, DESIGN, AND ANALYSIS.....</b>	<b>9</b>
2.1. System Description .....	9

2.2.	Performance Objectives and Design Criteria .....	11
2.2.1.	Criterion (i): Minimum Outer Shell Thickness .....	11
2.2.2.	Criterion (ii): Energy Dissipators Strength .....	12
2.2.3.	Criterion (iii): Composite Action.....	13
2.2.4.	Criterion (iv): Mortar Bed Integrity .....	14
2.2.5.	Criterion (v): Concrete Strain Control and Inner Shell Diameter.....	15
2.2.6.	Criterion (vi): Prevention of Early Dissipator Fracture .....	15
2.2.7.	Criterion (vii): Prevention of Early Loss of Post-Tensioning Force .....	16
2.3.	Design Procedure.....	19
2.4.	Simplified Analysis.....	23
2.4.1.	Material Stress-Strain Relationships.....	23
2.4.1.1.	Outer-Shell Steel.....	23
2.4.1.2.	Post-Tensioning Steel .....	24
2.4.1.3.	Energy-Dissipator Steel .....	24
2.4.1.4.	Concrete .....	25
2.4.1.5.	Mortar.....	27
2.4.2.	Simplified Section Analysis .....	29
2.4.2.1.	Decompression Condition .....	30
2.4.2.2.	Rocking Joint Analysis .....	30
2.4.2.3.	Reference Yield Condition.....	33
2.4.3.	Simplified Pushover Relationship .....	34
2.4.3.1.	First-Order Base Shear .....	34
2.4.3.2.	First-Order Displacement and Drift Ratio.....	34
2.4.3.3.	Simplified Consideration of P-Delta Effects.....	35

2.4.3.4. Elastic Stiffness .....	36
2.5. Energy Dissipator Details.....	36
2.5.1. Internal Dowels.....	36
2.5.2. External Buckling-Restrained Devices .....	37
<b>CHAPTER 3 QUASI-STATIC CYCLIC EXPERIMENTS.....</b>	<b>41</b>
3.1. Test Specimens .....	41
3.1.1. Target Performance Objectives .....	41
3.1.2. Specimens Overview.....	42
3.1.3. Composite Column .....	43
3.1.4. Footing .....	44
3.1.5. Load Stub .....	45
3.1.6. Mortar Bed .....	45
3.1.7. Energy Dissipators.....	46
3.1.7.1. Unit 1A: External Buckling-Restrained Devices.....	46
3.1.7.2. Unit 1B: Internal Dowels .....	47
3.1.8. Post-Tensioning Bars .....	48
3.1.9. Elastomeric Pads.....	49
3.1.9.1. Unit 1A: Natural Rubber Pads.....	49
3.1.9.2. Unit 1B: Polyurethane Pads .....	49
3.2. Material Properties.....	50
3.2.1. Concrete .....	50
3.2.2. Mortar.....	51
3.2.3. Grout .....	52
3.2.4. Energy Dissipator Steel.....	53



3.2.5.	Rubber Pads.....	53
3.2.6.	Polyurethane Pads.....	54
3.3.	Instrumentation.....	54
3.3.1.	Overall Displacement and Rotation Measurements.....	55
3.3.2.	Column Deformation Measurements.....	55
3.3.3.	Outer-Shell Strain Measurements.....	55
3.3.4.	Post-Tensioning Bar Strain Measurements.....	56
3.3.5.	External Energy Dissipator Response Measurements.....	56
3.3.6.	Internal Energy Dissipator Strain Measurements.....	56
3.3.7.	Gravity-Equivalent Load Measurements.....	57
3.3.8.	Miscellaneous.....	57
3.4.	Loading Protocol and Test Outcomes.....	57
3.4.1	Loading Protocol.....	57
3.4.2.	Normalization of Response Parameters.....	58
3.4.3.	Outcomes for Unit 1A.....	59
3.4.3.1.	Mortar Bed.....	59
3.4.3.2.	Energy Dissipators.....	59
3.4.3.3.	Composite Column.....	60
3.4.4.	Outcomes for Unit 1B.....	61
3.4.4.1.	Mortar Bed.....	61
3.4.4.2.	Energy Dissipators.....	61
3.4.4.3.	Composite Column.....	62
3.4.5.	Comparison between Unit 1A and Unit 1B.....	62
<b>CHAPTER 4</b>	<b>NUMERICAL MODELING OF THE TEST UNITS.....</b>	<b>79</b>

4.1. Numerical Model Description .....	79
4.1.1. Composite Column .....	80
4.1.2. Mortar Bed .....	81
4.1.3. Post-Tensioning Bars .....	82
4.1.4. Energy Dissipators .....	82
4.1.4.1. Unit 1A: External Buckling-Restrained Devices.....	83
4.1.4.2. Unit 1B: Internal Dowels .....	83
4.1.5. Analysis Procedure .....	84
4.2. Numerical Analysis Results .....	85
4.2.1. Global Hysteretic Response .....	85
4.2.2. Global Energy Dissipation .....	85
4.2.3. Post-Tensioning Bar Strain History .....	85
4.2.4. Energy Dissipators Hysteretic Response .....	86
4.3. Simplified Analysis.....	87
<b>CHAPTER 5 CONCLUSIONS.....</b>	<b>93</b>
<b>APPENDIX CONSTRUCTION DRAWINGS .....</b>	<b>96</b>
<b>REFERENCES .....</b>	<b>127</b>

## LIST OF TABLES

Table 3.1	– Measured concrete compressive strength.....	50
Table 3.2	– Measured mortar compressive strength, Unit 1A.....	51
Table 3.3	– Measured mortar compressive strength, Unit 1B.....	51
Table 3.4	– Measured grout compressive strength, Unit 1A external dissipator anchorages into footing.....	52
Table 3.5	– Measured grout compressive strength, Unit 1B internal dissipator dowels into footing.....	52
Table 3.6	– Measured grout compressive strength, Unit 1B internal dissipator dowels into column.....	52
Table 3.7	– Measured steel mechanical properties.....	53

## LIST OF FIGURES

Figure 2.1 – Schematics of the proposed system: (a) column typical cross-section; (b) bent components and rocking kinematics; (c) joint rotation.....	39
Figure 2.2 – Hysteretic response: (a) conventional ductile system; (b) purely rocking system; (c) hybrid rocking system.....	39
Figure 2.3 – Design chart for deformable devices (bearings) in series with post-tensioning bars.....	39
Figure 2.4 – Confined concrete equivalent stress-block parameters (Paulay and Priestley, 1992).....	40
Figure 2.5 – Concrete compressive resultant parameters.....	40
Figure 2.6 – Energy dissipator details: (a) wrapped yield segment of an internal dowel; (b) dog-bone milled bar of a buckling-restrained device; (c) milled bar taper detail.....	40
Figure 3.1 – Test configuration and dimensions: (a) side elevation; (b) plan view; (c) overview of Unit 1A; (d) overview of Unit 1B.....	64
Figure 3.2 – Column details: (a) Unit 1A base cross-section; (b) Unit 1B base cross-section; (c) column longitudinal section; (d) outer shell with brackets for connection of external dissipators; (e) concentric shells and ducts for future grouting of internal dissipators; (f) weld beads on the outer-shell internal surface; (g) roughened concrete surface.....	65
Figure 3.3 – Footing details: (a) horizontal section; (b) longitudinal section; (c) reinforcement, ducts, and formwork; (d) steel ducts and spiral reinforcement.....	66
Figure 3.4 – Load-stub details: (a) horizontal section; (b) longitudinal section; (c) reinforcement, ducts, and formwork.....	67
Figure 3.5 – Mortar bed: (a) wood template and nylon-rod shims, during mortar placement; (b) mortar scraped from underneath the outer shell.....	68

Figure 3.6 – External energy dissipators: (a) location around column perimeter; (b) milled-bar dimensions; (c) dog-bone milled steel bar; (d) assembled buckling-restrained device.....	68
Figure 3.7 – Internal energy dissipators: (a) dowels grouted in the footing; (b) ducts in the column; (c) dowel dimensions; (d) detail of bar wrapping across the interface.....	69
Figure 3.8 – Post-tensioning bars: (a) bars screwed into the footing anchorages; (b) sleeved bars inside the hollow core; (c) anchorage components and dimensions; (d) assembled anchorage device.....	70
Figure 3.9 – Rubber bearing of Unit 1A: (a) components; (b) single pad; (c) assembled bearings.....	71
Figure 3.10 – Polyurethane bearing of Unit 1B: (a) components; (b) single pad; (c) assembled bearings.....	71
Figure 3.11 – Measured stress-strain relationships for the energy dissipator steel.....	72
Figure 3.12 – (a) Displacement transducers and (b) inclinometers.....	72
Figure 3.13 – Outer-shell strain gages: (a) Unit 1A; (b) Unit 1B.....	73
Figure 3.14 – Post-tensioning bars strain gages.....	73
Figure 3.15 – Energy dissipators instrumentation: (a) external buckling-restrained devices of Unit 1A; (b) internal dowels of Unit 1B.....	74
Figure 3.16 – Hysteretic lateral force-displacement response: (a) Unit 1A; (b) Unit 1B.....	74
Figure 3.17 – Lateral force-displacement response: (a) Unit 1A up to 3% drift ratio; (b) Unit 1A up to 10% drift ratio; (c) Unit 1B up to 3% drift ratio; (d) Unit 1B up to 10% drift ratio.....	75
Figure 3.18 – Maximum and residual drift ratios: (a) Unit 1A; (b) Unit 1B. Only cycles to positive displacements are reported.....	75
Figure 3.19 – Residual post-tensioning forces at the end of each cycle: (a) Unit 1A, north-east bar; (b) Unit 1B, south-west bar.....	76
Figure 3.20 – Crushed mortar bed at the end of testing: (a) Unit 1A; (b) Unit 1B.....	76
Figure 3.21 – Unit 1A: (a) distortion of external energy dissipators; (b) north-west energy dissipator hysteretic loops up to 5% drift ratio.....	77

Figure 3.22 – Permanent concrete and shell deformations at the end of testing: (a) Unit 1A; (b) Unit 1B.....	77
Figure 3.23 – Outer-shell longitudinal strain profiles in front of the south-west dowel for Unit 1B.....	78
Figure 3.24 – Neutral axis depth at peak lateral displacements: (a) Unit 1A; (b) Unit 1B.....	78
Figure 4.1 – Sketches of the test specimen numerical models: (a) Unit 1A; (b) Unit 1B.....	89
Figure 4.2 – Numerical and experimental lateral force-displacement response: (a) Unit 1A up to 1% drift ratio; (b) Unit 1A up to 5% drift ratio; (c) Unit 1B up to 1% drift ratio; (d) Unit 1B up to 5% drift ratio.....	89
Figure 4.3 – Numerical and experimental cumulative hysteretic energy: (a) Unit 1A; (b) Unit 1B.....	90
Figure 4.4 – Numerical and experimental post-tensioning bar strain history: (a) Unit 1A, north-east bar; (b) Unit 1B, south-west bar.....	90
Figure 4.5 – Numerical and experimental hysteretic response of the north-west energy dissipator in Unit 1A: (a) cycles up to 1% drift ratio; (b) cycles up to 5% drift ratio.....	91
Figure 4.6 – Simplified numerical prediction of the pushover envelope: (a) Unit 1A; (b) Unit 1B.....	91
Figure 4.7 – Simplified numerical and experimental neutral-axis depth: (a) Unit 1A; (b) Unit 1B. Only positive cycles are shown.....	92

## ACKNOWLEDGMENTS

More than six years have passed by since I started my doctoral program at the University of California, San Diego, and many people have shared their road with me during this journey. My sincere gratitude goes to all of them, who made this experience so enjoyable and rewarding.

I would like to express my deepest and most sincere gratitude to my faculty advisor, Professor José Restrepo, whose guidance and support have been the key to my academic, professional and personal growth over the past six years. By involving and exposing me to many aspects of research and teaching, he gave me the opportunity to develop a variety of skills that I believe will prove to be very valuable in my future.

I would also like to thank all the other members of my doctoral committee, Professor Benson Shing, Professor Chia-Ming Uang, Professor Peter Shearer, and Professor James Fowler, for their time, comments, and encouragement during this time.

The Pacific Earthquake Engineering Research Center (PEER) provided research funds and networking opportunities related to the work presented in my thesis. Among many people I had the pleasure to meet through PEER, I would like to particularly thank Prof. Marc Eberhard, Dr. Olafur Haraldsson, Prof. Steven Mahin, Prof. Claudia Ostertag, Prof. Marios Panagiotou, Dr. Matthew Schoettler, Prof. John Stanton, Dr. Vesna Terzic,

and Dr. William Trono.

The outcomes of the research program presented in this thesis would have not been the same without the contributions of Ms. Milena Massari (University of Bologna, Italy), Mr. Athanassios Vervelidis (University of Bologna, Italy), Dr. Giovanni De Francesco (University of Catania, Italy), and Ms. Maura Torres (University of California, Berkeley), who are duly acknowledged for their participation.

As experimental testing constituted a large portion of my research during these years, the support of the staff at UCSD's Powell Structural Engineering Laboratories and Englekirk Structural Engineering Center was essential. In particular, I would like to thank the operations managers, Mr. Paul Greco and Mr. Andrew Gunthardt, for their efforts. I would also like to acknowledge Mr. Noah Aldrich, Mr. Robert Beckley, Mr. Raymond Hughey, Dr. Christopher Latham, Mr. Tim McAuliffe, Dr. Dan Radulescu, Mr. Lawton Rodriguez, Mr. Alex Sherman, and Mr. Hector Vicencio for their help with construction, instrumentation and testing of my specimens.

I would be unjust if I would not mention my fellow students, researchers, and co-workers who shared with me the challenges of UCSD's academic life. Among many other people who made this experience more enjoyable, I would like to thank Dr. Grigorios Antonellis, Mr. Rodrigo Astroza, Prof. Andre Barbosa, Prof. Ivan Bartoli, Dr. Noemi Bonessio, Mr. Francesco Carrea, Mr. Rodrigo Carreno, Dr. Rauno Cavallaro, Ms. Michelle Chen, Dr. Stefano Coccia, Mr. David Duck, Mr. Hamed Ebrahimian, Mr. Alessandro Fasolo, Mr. Andreas Gavras, Dr. Maurizio Gobbato, Dr. Francesco Graziotti, Mr. Andreas Koutras, Prof. Giuseppe Lomiento, Mr. Koorosh Lotfizadeh, Mr. Stefano Mariani, Mr. Giovanni Montefusco, Dr. Flavio Mosele, Dr. Juan Murcia Delso, Mr. Arpit



Nema, Dr. Claudio Nucera, Ms. Elide Pantoli, Mr. Marco Pigazzini, Prof. Salvatore Salamone, Mr. Andrew Sander, Mr. Francesco Selva, Prof. Andreas Stavridis, and Ms. Ilaria Tomassi.

I would like to express my sincere gratitude to all my friends, the ones I left in Italy and the ones I met in San Diego: you've always made me feel home wherever I was. Very special thanks go to my friends from Santo Spirito in Imola, and "I Ragazzi di Villa Lamont" in San Diego: the good times spent with you was the fuel to travel through this rewarding, yet demanding, experience.

Finally, I would like to acknowledge the continuous support I received during all my life from my mother, Anna, my father, Ermete, and my sister, Laura: they have always encouraged me to reach my objectives, even though it wasn't easy for them when I decided to leave Italy. I would also like to deeply thank my maternal grandmother, Lea, who provided for all the financial needs related to my education: she believed in me and in my ability to succeed, and she would have been glad to see me achieving this goal.

# VITA

## EDUCATION

- 2005        Laurea (Bachelor-level degree), Civil Engineering, University of Bologna, Italy.
- 2008        Laurea Magistrale (Graduate-level degree), Civil Engineering, University of Bologna, Italy.
- 2010        Master of Science, Structural Engineering, University of California, San Diego.
- 2012        Candidate in Philosophy, Structural Engineering, University of California, San Diego.
- 2014        Doctor of Philosophy, Structural Engineering, University of California, San Diego.

## EXPERIENCE

- 2006-2007    Education Abroad Program, University of California, San Diego, La Jolla, CA.
- 2007-2014    Teaching Assistant, University of California, San Diego, La Jolla, CA.
- 2007-2007    Teaching Assistant, California State Summer School for Mathematics and Science – University of California, San Diego, La Jolla, CA.
- 2008-2014    Graduate Student Researcher, University of California, San Diego, La Jolla, CA.
- 2009-2009    Instructor, California State Summer School for Mathematics and Science – University of California, San Diego, La Jolla, CA.
- 2009-2009    Teaching Assistant, European School for Advanced Studies in Reduction

of Seismic Risk (ROSE School), Pavia, Italy.

2014-Present Structural engineer intern, City and County of San Francisco – Department of Public Works, San Francisco, CA.

## **HONORS AND AWARDS**

2004-2005 “Arrigo and Anella Focherini Memorial” Scholarship, University of Bologna, Italy.

2006-2007 “Overseas - Education Abroad Program” Scholarship, University of Bologna, Italy.

2008-2009 Structural Engineering Department Fellowship, University of California, San Diego.

2010-2011 “E.K. Rice and W.C. Bailey Memorial” Scholarship, Post-Tensioning Institute.

2013 “Best Presentation Award”, 10<sup>th</sup> International Conference on Earthquake Engineering, Tokyo Institute of Technology, Japan.

## **PROFESSIONAL AFFILIATIONS**

2009-Present Structural Engineers Association of California: Student Member.

2009-Present American Concrete Institute: Student Member.

2010-Present American Institute of Steel Construction: Student Member.

2010-Present Post-Tensioning Institute: Student Member.

2010-Present American Society of Civil Engineers: Student Member.

2010-Present Board for Civil and Environmental Engineers, Bologna, Italy: Licensed Professional Engineer.

2011-Present Board for Professional Engineers, Land Surveyors, and Geologists of California: Engineer-in-Training.

## PUBLICATIONS

**Guerrini, G.** and Restrepo, J.I., “Higher-Mode Effects in Performance-Based Seismic Design of High-Rise Buildings”. *Proc. 78<sup>th</sup> Annual Convention of the Structural Engineers Association of California*, San Diego, CA, USA, September 23-26, 2009.

**Guerrini, G.** and Restrepo, J.I., “Advanced Precast Concrete Dual-Shell Steel Columns”. *Proc. 8<sup>th</sup> Conference on Urban Earthquake Engineering*, Tokyo Institute of Technology, Tokyo, Japan, March 7-8, 2011.

**Guerrini, G.**, Massari, M., Vervelidis, A., and Restrepo, J.I., “Self-Centering Precast Concrete Dual-Shell Steel Columns”. *Proc. 15<sup>th</sup> World Conference on Earthquake Engineering*, Lisbon, Portugal, September 24-28, 2012.

**Guerrini, G.** and Restrepo, J.I., “Seismic Response of Recentering Precast Composite Concrete-Dual-Shell-Steel Columns”. *Proc. 10<sup>th</sup> Conference on Urban Earthquake Engineering*, Tokyo Institute of Technology, Tokyo, Japan, March 1-2, 2013.

Schoettler, M.J, Restrepo, J.I., **Guerrini, G.**, Duck, D.E., and Carrea, F., “Bridge Column Response to Ground Shaking Induced by a Shake Table”. *Proc. 7<sup>th</sup> National Seismic Conference on Bridges & Highways*, Oakland, CA, USA, May 20-22, 2013.

**Guerrini, G.** and Restrepo, J.I., “Seismic Response of Composite Concrete-Dual-Steel-Shell Columns for Accelerated Bridge Construction”. *Proc. 7<sup>th</sup> National Seismic Conference on Bridges & Highways*, Oakland, CA, USA, May 20-22, 2013.

**Guerrini, G.**, Restrepo, J.I., Massari, M., and Vervelidis, A., “Seismic Behavior of Post-Tensioned Self-Centering Precast Concrete Dual-Shell Steel Columns”. *ASCE Journal of Structural Engineering*, July 2014.

Antonellis, G., Gavras, A., Panagiotou, M., Kutter, B., **Guerrini, G.**, Sander, A., and Fox, P., “Shake Table Test of Bridge Columns Supported on Rocking Shallow Foundations”. *ASCE Journal of Geotechnical and Geoenvironmental Engineering*, in press.

## PRESENTATIONS

**Guerrini, G.** and Restrepo, J.I., “Advanced Precast Concrete Dual-Shell Steel Columns”. Poster, *2009 PEER Annual Meeting*, Pacific Earthquake Engineering Research Center, San Francisco, CA, USA, October 15-16, 2009.

**Guerrini, G.**, “Inelastic Behavior of Reinforced Concrete Structures”. *Seminar*, Department of Civil, Environmental, and Materials Engineering, University of Bologna, Italy, December 16, 2009.

**Guerrini, G.**, “Ductile Behavior of Reinforced Concrete Structures”. *Invited Lecture*, Department of Civil, Environmental, and Materials Engineering, University of Bologna, Italy, May 16, 2010.

**Guerrini, G.**, Schoettler, M.J., Carrea, F., Duck, D.E., Mahin, S.A., Restrepo, J.I., and Buckle, I., “Large-Scale Validation of Seismic Performance of Bridge Columns”. Poster, *2010 Quake Summit & PEER Annual Meeting*, Network for Earthquake Engineering Simulation and Pacific Earthquake Engineering Research Center, San Francisco, CA, USA, October 8-9, 2010.

**Guerrini, G.**, Schoettler, M.J., Carrea, F., Duck, D.E., Mahin, S.A., Restrepo, J.I., and Buckle, I., “Large-Scale Validation of Seismic Performance of Bridge Columns”. Poster and oral presentation, *2011 Quake Summit & MCEER Annual Meeting*, Network for Earthquake Engineering Simulation and Multi-Disciplinary Center for Earthquake Engineering Research, Buffalo, CA, USA, June 9-11, 2011.

**Guerrini, G.** and Restrepo, J.I., “Advanced Precast Concrete Dual-Shell Steel Columns”. Poster, *2011 PEER Annual Meeting*, Pacific Earthquake Engineering Research Center, Berkeley, CA, USA, September 30-October 1, 2011.

**Guerrini, G.** and Restrepo, J.I., “Seismic Response of Recentering Low-Damage Precast Concrete Dual-Shell Steel Columns”. Poster, *2012 PEER Annual Meeting*, Pacific Earthquake Engineering Research Center, Berkeley, CA, USA, October 26-27, 2012.

**Guerrini, G.**, “Seismic Performance of Ductile Reinforced Concrete Bridge Piers”. *Seminar*, University of the Republic of San Marino and University of Modena and Reggio Emilia, Italy, December 21, 2012.

**Guerrini, G.**, “Large Scale Validation of Seismic Performance of Reinforced Concrete Bridge Columns”. *Invited Lecture*, Department of Structural Engineering, University of California, San Diego, La Jolla, CA, January 29, 2013.

**Guerrini, G.**, “Seismic Behavior of a Recentering Bridge Column for Accelerated Bridge Construction”. *Presentation for the NEES-REU Orientation*, Department of Structural Engineering, University of California, San Diego, La Jolla, CA, June 20, 2013.

# **ABSTRACT OF THE DISSERTATION**

## **SEISMIC PERFORMANCE OF PRECAST CONCRETE DUAL-SHELL STEEL COLUMNS FOR ACCELERATED BRIDGE CONSTRUCTION**

by

Gabriele Guerrini

Doctor of Philosophy in Structural Engineering

University of California, San Diego, 2014

Professor José I. Restrepo, Chair

This study presents an innovative bridge column technology for application in seismic regions. The proposed technology combines a precast post-tensioned composite steel-concrete hollow-core column with supplemental energy dissipation, in a way to reduce on-site construction burdens and minimize earthquake-induced residual deformations, damage, and associated repair costs. The column consists of two steel

cylindrical shells, with high-performance concrete cast in between. Both shells act as permanent formwork; the outer shell substitutes the longitudinal and transverse reinforcement, as it works in composite action with the concrete, whereas the inner shell removes unnecessary concrete volume from the column, prevents concrete implosion, and prevents buckling of energy dissipating dowels when embedded in the concrete. Large inelastic rotations can be accommodated at the end joints with minimal structural damage, since gaps are allowed to open at these locations and to close upon load reversal. Longitudinal post-tensioned high-strength steel threaded bars, designed to respond elastically, in combination with gravity forces ensure self-centering behavior. Internal or external steel devices provide energy dissipation by axial yielding. This dissertation reviews the main principles and requirements for the design of these columns. The experimental findings from two quasi-static reversed cyclic tests are then presented, and numerical simulations of the experimental response are proposed.

# Chapter 1

## INTRODUCTION

### 1.1. GENERAL CONSIDERATIONS

According to the U.S. Department of Transportation (2012), as of 2011 approximately 11% of the 630,141 United States bridges were considered structurally deficient, while 12% were deemed functionally obsolete: this means that about 145,000 bridges throughout the United States may need some kind of repair, ranging from minor retrofit to full replacement. Many of these structurally deficient or functionally obsolete bridges serve as key links in local and national transportation networks, with severe impacts associated with their closures. A large amount of these structures can be found in densely populated urban areas, where the impacts of construction work on traffic, environment, society, and economy are uneasily tolerated; moreover, lengthy on-site bridge construction projects put construction workers at increased risk. Minimizing construction time therefore becomes essential to reduce the aforementioned consequences on the public, workers, and environment.

Considering that a significant number of bridges is located in earthquake-prone regions, the impact and cost of earthquake-induced damage on these structures have



raised serious questions on whether the current seismic design philosophy can satisfy the needs of modern society. Designing a structure to respond elastically under severe earthquakes has generally been considered impractical for economic reasons; as a result, current bridge seismic design provisions (Caltrans, 2010; AASHTO, 2012) allow columns to respond beyond the elastic limit and to be damaged under the design-basis earthquake, provided that collapse is prevented. Inelastic behavior is typically localized within flexural plastic-hinge regions at the bottom and/or top of the columns: these regions experience structural damage during the design-basis earthquake.

However, the consequences of structural damage in a bridge system can be critical if associated with the temporary interruption of an important road path: obstruction of rescue and recovery operations in the immediate disaster aftermath, and economical losses related to medium- and long-term business interruption and displacement of people and goods (Palermo et al., 2008). While the concept of structural damage is widely accepted in design practices, resilient communities expect strategic structures and bridges to survive moderately strong earthquakes with little or no disturbance to traffic and business.

The significant number of bridge structures requiring replacement, the continuous construction of new infrastructures throughout the country, and the extent of the nation's bridge stock interested by seismic activity, underline the need for innovative design approaches to reduce public and environmental impacts, improve jobsite safety and construction quality, and ultimately save money. As a consequence, research efforts have been directed to the development of bridge technologies that minimize structural damage, encompass self-centering properties (Restrepo et al., 2011; Guerrini et al., 2011), and

reduce construction time and traffic impact (FHWA, 2012; Culmo, 2011).

This dissertation describes the main features of a precast composite concrete-dual steel shell bridge column technology with self-centering behavior induced by unbonded post-tensioning. This column is designed to display only minor incipient damage under the same earthquake demands that would cause extensive damage on conventional columns. Even under demands 50% larger than the design one, damage is maintained at a minimum level. This results in a dramatic reduction of repair cost and downtime.

The remainder of this introductory chapter covers the background on self-centering systems and composite concrete-filled tube columns. Chapter 2 illustrates the main features, design criteria, and simplified analysis tools for the proposed column technology. Findings from experimental investigations are shown in Chapter 3 and Chapter 4. Analytical modeling of the tested specimens is summarized in Chapter 5. The work presented here is an enhancement to the earlier research described in Restrepo et al. (2011).

## **1.2. BACKGROUND ON SELF-CENTERING/ROCKING SYSTEMS**

The term “hybrid system” refers to structural systems that, under the effect of lateral forces such as earthquake-activated inertia, are able to rock and self-center back to their original configuration, while dissipating energy through specifically designed devices. The concept originated from the features of the “stepping” railway bridge over the South Rangitikei River, New Zealand (Cormack, 1988) commissioned in 1981, where rocking is combined with torsional hysteretic energy dissipator devices. Similar features were also provided a few years earlier to an industrial chimney of the Christchurch, New

Zealand airport (Sharpe and Skinner, 1983), built in 1977.

The idea was then expanded by Priestley and Tao (1993), who analytically investigated the behavior of building moment frames incorporating partially unbonded post-tensioning tendons as lateral-force resisting systems for buildings: they pointed out as the main advantage the lack of residual drifts following an earthquake. MacRae and Priestley (1994) subsequently conducted experimental work on beam-column sub-assemblies featuring unbonded post-tensioning details. Stone et al. (1995) proposed a hybrid rocking system that incorporated mild reinforcement across the joint to provide hysteretic energy dissipation. The promising results from these preliminary studies resulted in the “PREcast Seismic Structural Systems” (PRESSS) program, in which an array of precast rocking systems was investigated (El-Sheikh et al., 1999; Kurama et al. 1999). This program culminated with the test of a 60%-scale, five-story building (Nakaki et al., 1999; Priestley et al., 1999): the building incorporated a rocking coupled wall designed to provide lateral force resistance in one direction of loading, and moment frames with and without unbonded tendons in the other direction.

Christopoulos et al. (2002) extended the concept of unbonded post-tensioning combined with energy dissipation to steel moment frames. Pérez et al. (2003) conducted experiments on vertically stacked wall segment, prestressed with unbonded tendons. Holden et al. (2003) tested a precast hybrid wall incorporating mild steel energy dissipators, carbon fiber tendons, and steel-fiber-reinforced concrete. Restrepo and Rahman (2007) performed experiments on self-centering structural walls, developing design strategies and details for energy dissipators. Toranzo et al. (2009) adapted the self-centering wall idea to confined masonry construction, and developed an innovative

external hysteretic energy dissipator device.

Apart from the South Rangitikei River bridge, the early development of hybrid systems was mainly focused on implementation in buildings; however, interest in their application to bridges increased in the past fifteen years. One of the pioneering experimental studies on the use of rocking bridge columns incorporating unbonded post-tensioning was carried out by Mander and Cheng (1997). This project was followed by an experimental program conducted by Hewes and Priestley (2002) in which the response of segmental bridge piers incorporating unbonded post-tensioning was investigated. A number of analytical studies were subsequently carried out considering potential applications of self-centering solutions to bridge columns (Kwan et al., 2003; Kwan et al., 2003; Sakai et al., 2004; Palermo et al., 2005; Heiber et al., 2005; Ou et al., 2006; Palermo et al. 2008). Shake table testing of cast-in-place hybrid concrete bridge columns was performed to investigate the dynamic response characteristics of these systems (Sakai, et al., 2006). Palermo et al. (2007) and Marriott et al. (2009, 2011) carried out analytical studies and quasi-static cyclic tests on monolithic, purely rocking, and hybrid concrete columns, developing different solutions for energy dissipation. Solberg et al. (2009) conducted quasi-static and pseudo-dynamic bidirectional tests on hybrid post-tensioned bridge columns with armored rocking interfaces. Ou et al. (2010) performed large-scale experiments on precast segmental post-tensioned bridge columns.

### **1.3. BACKGROUND ON CONCRETE-FILLED TUBE COLUMNS**

“Concrete-filled tubes” (CFT), also termed “steel columns filled with concrete” or “in-filled composite columns”, are a type of composite steel-concrete columns which has

gained interest for seismic applications in the past three decades (Shanmugam et al., 2001).

Tests conducted by Ghosh (1977) demonstrated the beneficial effect of concrete filling on the axial load and bending moment capacities. Suzuki and Kato (1981) observed that in relatively short CFTs, the confined concrete can act as a diagonal compression strut together with tension field action of the steel side walls. Experiments on circular CFT columns were performed by Prion et al. (1989) to study the effect of steel yield stress, tube thickness, concrete compressive strength, concrete confinement, aspect ratio (length to diameter), and load application on the whole section as opposed to load application on concrete alone. Shakir-Khalil and Zeghiche (1989) tested rectangular in-filled composite columns under pure compression and in combination with uniaxial and biaxial bending, concluding that the failure mode of all columns was overall buckling, with no sign of local buckling of the steel section. Ge and Usami (1992) studied the buckling modes of stiffened and unstiffened in-filled columns, observing the beneficial interaction between stiffeners and concrete in delaying buckling.

Further tests on rectangular CFT columns by Shakir-Khalil and Mouli (1990) showed that the relative carrying capacity of composite-to-steel column increases when the size of the steel section is increased and with the use of high strength concrete. Rangan and Joyce (1992), O'Brien and Rangan (1993), and O'Shea and Bridge (1995) tested eccentrically loaded slender steel tubular columns, filled with high-strength concrete: all specimens failed due to crushing of the compressed concrete, with the extreme tensile strains not reaching the yield strain of steel. Uy and Patil (1996) studied the behavior of concrete-filled high-strength steel fabricated box columns observing a

similar failure mode. A number of analytical methods for the calculation of the ultimate strength of CFT columns have been proposed by Knowles and Park (1969), Neogi et al. (1969), Rangan and Joyce (1992), Ge and Usami (1994), Bradford (1996), Kato (1996), Wang and Moore (1997), Leon et al. (2007).

Virdi and Dowling (1973) investigated the bond between concrete and steel tube. Mechanical connectors are necessary for transferring shear between concrete and steel tube when bond capacity is likely to be exceeded such as in case of significant shear demand or under seismic loading (Gebman et al. 2006).

Sakino and Tomii (1981) and Sakino and Ishibashi (1985) examined the behavior of short and intermediate length square CFT columns, subjected to cyclic lateral forces with a constant axial load: the hysteretic loops indicated a stable response with a considerable amount of energy dissipation and some strength degradation due to local buckling in the steel shell, leading to crushing of the encased concrete. Park et al. (1983) performed an experimental and theoretical investigation into the seismic behavior of steel-encased circular reinforced concrete bridge piles, with variable axial-load level, inclusion or exclusion of internal reinforcing cages, and continuous or discontinuous steel casing at the critical flexural sections. Boyd et al. (1995) found that the ductility for columns with studded and non-studded steel shells is similar, and that the hysteretic energy dissipated by composite columns is higher than that for conventionally reinforced columns, with local steel shell buckling and concrete cracking causing some irregularities in the hysteretic response. A study was conducted by Itani (1996) to determine the adequacy of composite steel-concrete columns for use in seismic areas in terms of ductility; full composite action between the steel jacket and the concrete was ensured by

shear studs, distributed throughout the length of the column.

Kitada (1998) studied the difference in local buckling modes between cross-sections of steel and composite columns in bridge columns and buildings; in particular, he observed that the ductility of the composite beam-column specimen with rectangular cross-section is smaller compared to that with a circular cross-section in the case of large axial compression. In fact, as confirmed by Matsui et al. (1995), circular tubes provide a significant amount of confinement, while this effect is negligible in the case of rectangular tubes as the hoop tension developed along the side walls is not constant.

## Chapter 2

# SELF-CENTERING DUAL-SHELL COLUMNS: FEATURES, DESIGN, AND ANALYSIS

### 2.1. SYSTEM DESCRIPTION

The “dual-shell” composite steel-concrete bridge column described herein consists of two concentric cylindrical steel shells running for its entire height, with high-performance concrete (high strength, high slump, and reduced shrinkage) sandwiched in between (see Fig. 2.1(a)). The outer shell acts as permanent formwork, providing also longitudinal and transverse reinforcement, as it works in composite action with the concrete. Longitudinal reinforcement, if needed, is detailed only in the form of dowels between the column ends and the footing or bent cap. The inner shell provides permanent formwork too, reducing unnecessary weight and making the technology suitable for prefabrication and rapid erection. It also prevents concrete implosion upon crushing under large compressive strains, which may develop upon gap opening, and delays buckling of energy dissipating dowels embedded in the concrete.

Large inelastic rotations can be sustained at the column-footing and column-cap



beam joints with minimal structural damage. These rotations are accommodated within the connections themselves, through the formation of gaps at the member interfaces (Fig. 2.1(*b*) and (*c*)): gaps are allowed to open in tension under severe lateral displacement demand, and to practically close at the end of the excitation. Self-centering/rocking capability is provided by gravity forces and unbonded threaded post-tensioning (PT) bars, designed to remain elastic. The bolted PT bar anchorages at the bent cap and foundation allow for eventual bar replacement, should corrosion or other types of damage be a concern.

Energy dissipation takes place through axial yielding of internal steel dowels (Restrepo and Rahman, 2007; Restrepo et al., 2011), as shown in Figure 2.1(*b*), or external devices (Cormack, 1998; Marriott et al., 2009; Toranzo et al., 2009), preventing the main structural members from experiencing significant inelastic deformations and damage. Under strong-intensity earthquake excitation only these devices may undergo multiple cycles within the inelastic range, with possible need of replacement, but the structure is expected to remain functional overall. Circumferential weld beads are provided on the internal surface of the outer shell, only near its ends (Gebman et al., 2006; Restrepo et al., 2011), to transfer tension between the internal dowels and the outer shell. External dissipators are simply connected to brackets preinstalled on the outer shell and on the footing or bent cap.

The expected hysteretic response of this hybrid structural system is compared to the one of conventional ductile and purely rocking structures on Figure 2.2. A conventional ductile system (Fig. 2.2(*a*)) offers large energy dissipation, represented by “fat” hysteretic loops, at the expenses of structural integrity and significant residual

displacement. A purely rocking solution (Fig. 2.2(b)) is characterized by non-linear elastic behavior with self-centering capability, but insufficient energy dissipation resulting in hard-to-control peak displacement demand (Makris et al. 1998). A hybrid system (Fig. 2.2(c)) provides a trade-off between these two extremes: balancing self-centering forces and energy dissipation, it shows a “flag-shaped” response, with very small residual displacement but peak demand comparable to those of conventional systems.

## **2.2. PERFORMANCE OBJECTIVES AND DESIGN CRITERIA**

Columns of this type can be easily designed for a single performance level, say the design-basis earthquake. Seven criteria should be met to ensure satisfactory performance of the proposed column technology for this performance level: (i) minimum outer shell thickness, (ii) energy dissipators strength, (iii) composite action, (iv) mortar bed integrity, (v) concrete strain control, dowel buckling, and inner shell diameter, (vi) prevention of early dissipator fracture, and (vii) prevention of early loss of post-tensioning force.

### **2.2.1. Criterion (i): Minimum Outer Shell Thickness**

As the external shell provides confinement to the compressed concrete, tensile hoop strains arise in the shell. When the column is subjected to the target lateral displacement, these strains should be kept below the yield strain, to avoid permanent deformation and damage to the shell and to preserve the composite action with the encased concrete. To meet this objective, based on previous experiments (Gebman et al.,

2006; Restrepo et al., 2011) and the tests reported here, the outer shell should satisfy the condition:

$$D_o/t_o \leq 100 \quad (2-1)$$

where  $D_o$  is the outer diameter and  $t_o$  the outer-shell thickness. Such ratio results in a minimum volumetric confinement ratio for the concrete of 4% calculated over the solid volume of the column, which adequately confines the high-strength concrete recommended for this application.

In addition, the shell should possess sufficient strength to ensure that the flexural strength of the composite column, at the section where the interface dowel bars end or where the external energy dissipators are connected to the shell, is equal or greater than that required by capacity design, assuming that flexural overstrength develops at the column ends where joint opening will take place. However, this second condition is not expected to control the design.

### **2.2.2. Criterion (ii): Energy Dissipators Strength**

Recentering forces, provided by gravity and post-tensioning, and energy dissipating forces need to be well tuned, to achieve the desired self-centering response and provide sufficient energy dissipation. Gravity and post-tensioning forces must be large enough to close the gap by overcoming the overstrength capacity of the energy dissipators, thus forcing them to yield in compression at each load reversal (Restrepo and Rahman, 2007); that is:

$$\Lambda_C = \frac{F_{ED,O}}{P_u + F_{PT,e}} \leq 1.0 \quad (2-2)$$

where  $P_u$  is the design gravity force,  $F_{PT,e}$  is the total effective post-tensioning force (after time-dependent losses),  $F_{ED,O}$  is the total ultimate strength of all energy dissipators, and  $\Lambda_C$  is a recentering coefficient. The limitation on  $\Lambda_C$  could theoretically be taken as high as 1.0 (i.e. equality between dissipators overstrength force and recentering forces), but a limit of 0.6 is recommended to account for uncertainties on post-tensioning losses and, primarily, for the presence of debris upon gap opening in the rocking interfaces.

In parallel, enough energy dissipation should be provided to the system, to avoid the large scatter on lateral displacement demands observed on purely rocking systems (Makris et al. 1998). For this reason, a second condition should be satisfied:

$$\Lambda_D = \frac{F_{ED,O}}{P_u + F_{PT,e} + F_{ED,O}} \geq 0.1 \quad (2-3)$$

where  $\Lambda_D$  is an energy dissipation coefficient. Combining together Eq. 2-2 and Eq. 2-3, setting the limitation  $\Lambda_C \leq 0.6$ , yields the following relationship:

$$0.1 \leq \Lambda_D \leq 0.4 \quad (2-4)$$

### 2.2.3. Criterion (iii): Composite Action

If internal dowels are used for energy dissipation, tensile stresses need to be transferred from the dowels to the outer shell through the concrete, in order to develop composite steel-concrete action. As friction between steel and concrete cannot be relied on, mechanical connectors are needed: for this purpose, circumferential weld beads or bars welded on the internal surface of the outer shell can be provided along the

development length of the dowels (Gebman et al., 2006; Restrepo et al., 2011). Weld beads of similar size to the outer shell thickness, spaced at about 10 times their size, proved to be sufficient to develop the stress transfer and ensure composite action (Gebman et al., 2006).

#### **2.2.4. Criterion (iv): Mortar Bed Integrity**

In-situ construction tolerances require a mortar bed to be cast between the column ends and the adjoining footing and superstructure. Under the design-basis earthquake, crushing of the mortar layer between column and footing or column and cap beam should be avoided, as it would lead to post-tensioning losses. The integrity of the mortar could be ensured by checking that, at the smeared curvature corresponding to the joint opening under the target lateral displacement, the neutral axis depth should meet the condition:

$$c/D_o \leq 0.25 \quad (2-5)$$

where  $c$  is the neutral axis depth. This upper-bound value is suggested to limit the area of mortar subjected to large compressive strain demand and to retain enough stiffness.

The use of high-performance (high strength, high fatigue resistant, low shrinkage) materials is recommended; grout mixes incorporating metallic aggregate and/or polypropylene fibers are suitable for this application. Embedding headed bars in the column and in the adjoining members, with the heads matching each other at the interface, can help significantly in relieving the mortar bed from carrying high compressive stresses. Care needs to be taken to avoid direct contact between the mortar bed and the stiffer steel outer shell, which may cause early crushing; it is recommended to remove any excess mortar from below (or above ) the outer shell, so that compression

is transferred only between concrete and mortar, and between headed bars.

### 2.2.5. Criterion (v): Concrete Strain Control and Inner Shell Diameter

To prevent significant inner shell plastic deformations due to column concrete dilation, the neutral axis under the design-basis lateral displacement should not cut the hollow core, even though a compressive strain of 0.001 can be tolerated on the column concrete at the inner circle; this limitation defines the maximum diameter allowed for the inner shell.

In practical applications, a readily available lock-seam, helical corrugated steel pipe conforming to ASTM A760 (2010) can be used as the inner shell. Strength and stiffness of the thinnest commercially available corrugated drainage pipes are expected to be sufficient to prevent inward buckling of embedded energy dissipating dowels.

### 2.2.6. Criterion (vi): Prevention of Early Dissipator Fracture

Gap opening will induce significant elongation on the energy dissipators (Fig. 2.1(c)). Internal or external steel devices have to yield along a specific segment of length  $L_y$  to accommodate this elongation, without fracturing under the design-basis lateral displacement. To prevent low-cycle fatigue fracture, the strain along the yield segment should be limited to half the value  $\varepsilon_{ED,O}$  corresponding to the peak tensile stress. For a joint rotation  $\theta_j$ , the required yield length  $L_y$  is given by:

$$L_y = \frac{2 \times \left[ \theta_j \times (d_{ED}^{(e)} - c) - 12 \times \Lambda_s \times \varepsilon_{ED,y} \times d_{b,ED} \right]}{\varepsilon_{ED,O}} \quad (2-6)$$

where  $d_{ED}^{(e)}$  is the distance of the extreme tensile dissipator  $e$  from the extreme compressive fiber,  $\varepsilon_{ED,y}$  is the yield strain of the dissipator steel,  $d_{b,ED}$  is the diameter of the energy dissipating bar (the reduced diameter for dog-bone milled bars), and  $c$  is the neutral axis depth at the design-basis lateral displacement demand, which can be determined as for Criterion (iv).

The second term at the numerator of Eq. 2-6 accounts for yield strain penetration along the development length of non-milled energy dissipators embedded in concrete, which is assumed to be 6 times the bar diameter at each end (Park and Paulay, 1990).  $\Lambda_s$  is a strain-penetration coefficient:  $\Lambda_s = 1$  for non-milled unbonded bars, in which strain penetration out of the yield segment occurs;  $\Lambda_s = 0$  for dog-bone milled bars, where strain penetration is prevented.

### **2.2.7. Criterion (vii): Prevention of Early Loss of Post-Tensioning Force**

When the gap opens at the column-footing and/or column-cap interface, the post-tensioning bars will elongate as Figure 2.1(c) shows. If any of the post-tensioning bars yields, that bar will display a permanent plastic elongation when the gap closes, causing a loss of post-tensioning force and compromising the system self-centering ability. To delay yielding of these bars under the design-basis earthquake, and maintain self-centering behavior, the effective post-tensioning force after time-dependent losses should range between 20% and 25% of the bar tensile strength.

When limiting the post-tensioning force is not sufficient, additional deformability can be added to each post-tensioning bar by placing elastic devices in series with the bars.

Elastomeric bearing pads, inserted between the top anchor plate and the cap beam, have proved to be satisfactory for this scope. With this configuration the tensile deformation demand on the bars is partially transformed into compressive deformation of the bearing pads.

If  $F_{PT,e}^{(b)}$  and  $F_{PT,y}^{(b)}$  are the effective (after time-dependent losses) and yield post-tensioning force on the extreme tensile bar  $b$ , located at a distance  $d_{PT}^{(b)}$  from the extreme compressive fiber, the yield condition under a joint rotation  $\theta_j$  is given by:

$$F_{PT,y}^{(b)} = F_{PT,e}^{(b)} + \frac{n_j \times \theta_j \times (d_{PT}^{(b)} - c)}{\frac{L_U}{E_{PT} \times A_{PT}^{(b)}} + \frac{1}{K_B^{(b)}}} \quad (2-7)$$

where  $n_j$  is the number of column end joints subjected to gap opening ( $n_j=1$  for cantilever columns,  $n_j=1$  for fixed-fixed columns);  $c$  is the neutral axis depth from the extreme compressive fiber;  $L_U$ ,  $E_{PT}$ , and  $A_{PT}^{(b)}$  are the unbonded length, the elastic modulus, and the cross-sectional area of post-tensioning bar  $b$ ; and  $K_B^{(b)}$  is the stiffness of the bearing or other deformable device in series with bar  $b$ .

For a design-basis total joint rotation  $\theta_j^* = n_j \times \theta_j$  (sum of the top and bottom joint rotations) the required bearing-to-bar stiffness ratio can be found from Eq. 2-7 as:

$$\frac{K_B^{(b)}}{K_{PT}^{(b)}} = \frac{1}{n_j \times \theta_j \times \frac{d_{PT}^{(b)} - c}{(\varepsilon_{PT,y}^{(b)} - \varepsilon_{PT,e}^{(b)}) \times L_U} - 1} = \frac{1}{\theta_j^* \times \Lambda_B - 1} \quad (2-8)$$

where  $K_{PT}^{(b)} = E_{PT} \times A_{PT}^{(b)} / L_U$  is the axial stiffness of post-tensioning bar  $b$ ;  $\varepsilon_{PT,e}^{(b)}$  and  $\varepsilon_{PT,y}^{(b)}$  are the strains on bar  $b$  at the effective post-tensioning and yield conditions; and



$$\Lambda_B = \frac{d_{PT}^{(b)} - c}{\left(\varepsilon_{PT,y}^{(b)} - \varepsilon_{PT,e}^{(b)}\right) \times L_U} \quad (2-9)$$

is a non-dimensional coefficient. Smaller values of  $\Lambda_B$  denote systems less sensitive to post-tensioning bar yielding.

If Eq. 2-8 gives a negative value, bearings are not required. Furthermore, a positive value larger than 10 calculated from Eq. 2-8 indicates that the bearing pad would be very stiff compared to the bar, and would accommodate very small deformations, thus providing negligible additional flexibility.

A design chart derived from Eq. 2-8 is plotted on Figure 2.3. It can be observed that, for large total joint rotations  $\theta_j^*$ , very flexible bearings are required (low required stiffness ratios), and their stiffness is quite insensitive to the rotation demand. However, because of the inverse proportionality relationship between the stiffness ratio and the total joint rotation, when  $\theta_j^*$  decreases the need of bearings becomes suddenly negligible (high required stiffness ratios), as the curves become very steep. The threshold between these two regions depends on the coefficient  $\Lambda_B$ ; it can be noted that the bearings become completely ineffective (required stiffness ratio going to infinity) when  $\theta_j^* = 1/\Lambda_B$ .

The force-deformation characteristics of some elastomers, belonging to the Voigt materials family, is sensitive to loading rate and temperature. The bearing stiffness  $K_B^{(b)}$  should then be based on material properties evaluated at temperature and loading rate comparable to the expected ones. The loading rate under seismic excitation can be estimated dividing the difference  $F_{PT,y}^{(b)} - F_{PT,e}^{(b)}$  by one quarter of the structure's fundamental period.

Creep properties of the elastomeric material should be accurately known and accounted for, as time-dependent deformations of the bearings may affect significantly the long-term magnitude of the post-tensioning force. Time-dependent post-tensioning losses in the order of 20% to 40% of the initial force (after lock-off losses) may be anticipated, depending on the applied force, on the area and thickness of the bearing, and on the length of the post-tensioning bar. Incremental post-tensioning can help reducing the amount of losses due to bearing creep: most of the creep deformation happens during the first few hours after loading, and can be partially compensated by staged post-tensioning.

Implementing deformable devices made of other materials, such as steel ring springs, may reduce the influence of loading rate and creep. However, space constraint could make these alternative options not viable in some cases.

### **2.3. DESIGN PROCEDURE**

A step by step procedure for the proportioning of a dual-shell post-tensioned column is presented here, based on the seven criteria illustrated in the previous paragraphs and on a number of design assumptions.

#### ***Step 1: Determine the outer and inner shell diameters***

Several approaches can be adopted to select the outer-shell diameter. One of them consists in sizing an equivalent solid conventional reinforced-concrete column, with the same diameter as the dual-shell column. Assuming for example a concrete strength  $f'_{c,eq} = 35 \text{ MPa}$  (5 ksi) for the equivalent column, the outer diameter can be determined

by limiting the axial-force ratio to 10% of the capacity of the equivalent column:

$$A_{g,eq} \geq \frac{P_u}{0.1 \times f'_{c,eq}} \Rightarrow D_o \geq 3.6 \times \sqrt{\frac{P_u}{f'_{c,eq}}} \quad (2-10)$$

Alternatively, the designer may choose the outer-shell diameter from geometric considerations, such as limiting the shear span-to-diameter ratio, or following other proportioning criteria.

The inner-shell diameter can be sized based on initial guesses on Criteria (iv) and (v): assuming a neutral axis depth equal to  $(0.20 \sim 0.25) \times D_o$  and trying to prevent it from cutting through the hollow core, the inner diameter can be taken as:

$$D_i = (0.5 \sim 0.6) \times D_o \quad (2-11)$$

***Step 2: Determine the outer shell thickness***

The required outer shell thickness can be determined based on the considerations summarized in Criterion (i).

***Step 3: Calculate the post-tensioning force and dissipators strength***

An equivalent reinforced-concrete column as defined in Step 1, with a longitudinal reinforcement ratio of 2%, can be considered for this purpose. The total strength of the longitudinal reinforcement is:

$$T_{O,eq} = 0.02 \times A_{g,eq} \times f_{u,eq} \quad (2-12)$$

where the ultimate (peak) steel strength for conventional Grade 60 reinforcing steel,  $f_{u,eq}$ , can be taken equal to 630 MPa (90 ksi).

The force  $T_{O,eq}$  needs to be divided into effective post-tensioning force,  $F_{PT,e}$ , and energy dissipators strength,  $F_{ED,O}$ , in a proportion that satisfies Criterion (ii) requirements:

$$F_{PT,e} + F_{ED,O} = T_{O,eq} \quad (2-13)$$

***Step 4: Design the post-tensioning bars and elastomeric bearings***

Post-tensioning bars layout shall account for the space required by anchorage devices and jacking operations. The ideal location of post-tensioning bars is close to the section centroid, to reduce the elongation demand upon gap opening; however, this may not always be possible due to space constraints. Criterion (vii) must be checked to determine if elastomeric bearings (or other deformable devices) are needed and, if this is the case, what stiffness to provide. At this stage of the design, the neutral axis depth  $c$  can be conservatively taken equal to zero, and the target joint rotation  $\theta_j$  can be approximated by the corresponding drift-ratio in Eq. 2-8.

***Step 5: Design the energy-dissipator devices***

Energy dissipators are typically placed close to the perimeter of the column, embedded in the concrete or externally connected to the outer shell. Criterion (vi) can be used to determine the required yield length  $L_y$  of these devices. For design purposes, it is conservative to determine  $L_y$  by assuming  $c=0$  and  $\Lambda_s=0$  in Eq. 2-6. Moreover, the joint rotation  $\theta_j$  at the design earthquake can be made equal to the column drift ratio, thus, ignoring the elastic flexibility of the dual-shell column. For internal dowels,

Criterion (iii) provides guidelines to size the weld beads on the internal surface of the outer shell.

***Step 6: Check Criterion (iv)***

For design purposes, the neutral axis depth can be determined under the assumption that upon gap opening the extreme compressive fiber shortens by  $\theta_j \times c$  over a length equal to  $c$  (Restrepo and Rahman, 2007), where  $\theta_j$  is the joint rotation. In other words the extreme mortar compressive strain at the outer shell is taken equal to the joint rotation:

$$\varepsilon_{cm} = \frac{\theta_j \times c}{c} = \theta_j \quad (2-14)$$

Given the target joint rotation  $\theta_j$ , the cross-section geometry, the unbonded length  $L_U$  of the post-tensioning bars, the yield length  $L_Y$  of the energy dissipators, and the material properties, the forces on the post-tensioning bars and on the dissipators can be calculated; conventional reinforced-concrete section analysis methods can be applied to determine the neutral axis depth (see Section 2.4 for details). Care must be taken in these calculations if the neutral axis cuts the hollow core.

If Criterion (iv) is not satisfied, possible mitigations are increasing the outer diameter or the mortar compressive strength.

***Step 7: Check Criterion (v)***

The same section analysis carried out in Step 6 can be used to determine the concrete strain at the inner circle. To further simplify these calculations, it can be

assumed that within the strain range of interest ( $\varepsilon_c \leq 0.001$ ) concrete and mortar have the same elastic modulus. If Criterion (v) is not satisfied, possible solutions are reducing the inner diameter or increasing the mortar compressive strength.

## **2.4. SIMPLIFIED ANALYSIS**

Once the column cross-sections and its components have been sized, it is possible to derive a pushover relationship for the bent from the moment-rotation response of the column end sections at a few loading stages. The pushover curve provides information on the reference yield displacement and the elastic stiffness of the system, from which the its elastic period of the and the corresponding lateral displacement demand can be evaluated for comparison with the capacity of the system. The proposed simplified analysis method can be easily implemented in a spreadsheet.

### **2.4.1. Material Stress-Strain Relationships**

#### ***2.4.1.1. Outer-Shell Steel***

The composite steel-concrete section shall be capacity designed to remain elastic when the rocking kinematics develops. The outer shell needs also to provide adequate confinement to the column concrete. As a consequence, it is necessary to know the following properties of the outer-shell steel:

- elastic modulus  $E_{os}$
- yield stress  $f_{os,y}$

The relationship between outer-shell steel stress  $f_{os}$  and strain  $\varepsilon_{os}$ , for both

tensile and compressive deformations, is then:

$$f_{OS} = E_{OS} \times \varepsilon_{OS} \leq f_{OS,y} \quad (2-15)$$

#### ***2.4.1.2. Post-Tensioning Steel***

The design of elastomeric bearings or other deformable devices in series with the post-tensioning bars should ensure a linear-elastic response up to the target drift ratio. For this reason, post-tensioning bars are modeled as elasto-plastic. Only two parameters need to be assigned:

- elastic modulus  $E_{PT}$
- yield stress  $f_{PT,y}$  (or strain  $\varepsilon_{PT,y}$ )

The relationship between post-tensioning steel stress  $f_{PT}$  and strain  $\varepsilon_{PT}$ , for both tensile and compressive deformations, is then:

$$f_{PT} = E_{PT} \times \varepsilon_{PT} \leq f_{PT,y} \quad (2-16)$$

#### ***2.4.1.3. Energy-Dissipator Steel***

Energy-dissipator steel is represented by a bilinear material. The following parameters need to be defined:

- elastic modulus  $E_{ED}$
- yield stress  $f_{ED,y}$  (or strain  $\varepsilon_{ED,y}$ )
- peak stress  $f_{ED,o}$
- peak strain  $\varepsilon_{ED,o}$

The relationship between energy-dissipator steel stress  $f_{ED}$  and strain  $\varepsilon_{ED}$ , for both tensile and compressive deformations, is then:

$$f_{ED} = \begin{cases} E_{ED} \times \varepsilon_{ED} & \text{for } 0 \leq \varepsilon_{ED} \leq \varepsilon_{ED,y} \\ f_{ED,y} + \left( \frac{\varepsilon_{ED} - \varepsilon_{ED,y}}{\varepsilon_{ED,O} - \varepsilon_{ED,y}} \right) \times (f_{ED,O} - f_{ED,y}) & \text{for } \varepsilon_{ED,y} < \varepsilon_{ED} \leq \varepsilon_{ED,O} \end{cases} \quad (2-17)$$

#### 2.4.1.4. Concrete

The column concrete is very effectively confined by the outer steel shell. Its behavior is represented by Mander's model parameters (Mander et al., 1988) and by Paulay and Priestley's (1992) equivalent stress-block formulation illustrated in Figure 2.4. Analytical equations for the confined stress-block parameters have also been formulated by Karthik and Mander (2011). The designer needs to define two parameters:

- unconfined compressive strength  $f'_{c,c}$
- confinement efficiency coefficient  $K_{C,e} = 1.0$

The efficiency coefficient is set to 1.0 because arching does not affect confinement provided by a continuous shell. Once these values are chosen, the following set of parameters can be calculated:

- unconfined elastic modulus:

$$E_{C,c} = \begin{cases} 1800 \times \sqrt{f'_{c,c}} & \text{(ksi)} \\ 4,700 \times \sqrt{f'_{c,c}} & \text{(MPa)} \end{cases} \quad (2-18)$$

- unconfined peak strain:



$$\varepsilon_{C,c0} = \begin{cases} 0.0017 + \frac{f'_{C,c}}{8700} & \text{(ksi)} \\ 0.0017 + \frac{f'_{C,c}}{60,000} & \text{(MPa)} \end{cases} \quad (2-19)$$

- volumetric confinement ratio:

$$\rho_s = \frac{4 \times t_o}{D_o} \quad (2-20)$$

- effective lateral confining pressure:

$$f'_{C,\ell} = K_{C,e} \times f_{os,y} \times \frac{\rho_s}{2} \quad (2-21)$$

- confined-to-unconfined strength ratio:

$$K_C = -1.254 + 2.254 \times \sqrt{1 + 7.94 \times \frac{f'_{C,\ell}}{f'_{C,c}} - 2 \times \frac{f'_{C,\ell}}{f'_{C,c}}} \quad (2-22)$$

- confined compressive strength:

$$f'_{C,cc} = K_C \times f'_{C,c} \quad (2-23)$$

- confined peak strain:

$$\varepsilon_{C,cc0} = \varepsilon_{C,c0} \times [1 + 5 \times (K_C - 1)] \quad (2-24)$$

- secant modulus at peak confined strength, and ratios:

$$E_{C,sec} = \frac{f'_{C,cc}}{\varepsilon_{C,cc0}} \quad (2-25)$$

$$r_C = \frac{E_{C,c}}{E_{C,c} - E_{C,sec}} \quad (2-26)$$

$$n_C = \frac{E_{C,c}}{E_{C,sec}} \quad (2-27)$$

- confined crushing strain, and ratio:

$$\varepsilon_{C,ccu} = 0.004 + 2.5 \times \rho_s \quad (2-28)$$

$$x_{C,u} = \frac{\varepsilon_{C,ccu}}{\varepsilon_{C,cc0}} \quad (2-29)$$

- confined crushing strength:

$$f_{C,ccu} = \frac{f'_{C,cc} \times x_{C,u} \times r_C}{r_C - 1 + x_{C,u}^{r_C}} \quad (2-30)$$

Knowing these values, for a given extreme compressive strain  $\varepsilon_{cm}$  on the cross-section, or its ratio  $x_{C,m} = \varepsilon_{cm} / \varepsilon_{C,cc0}$ , one can use the charts of Figure 2.4 or the equations by Karthik and Mander (2011) to determine the equivalent stress-block parameters  $\alpha_{cc}$  and  $\beta_{cc}$ .

#### 2.4.1.5. Mortar

The mortar bed is partially confined by the outer steel shell, thanks to the friction developed with the column concrete. Its behavior is also represented by Mander's model parameters (Mander et al., 1988) and by Paulay and Priestley's (1992) equivalent stress-block formulation illustrated in Figure 2.4. Analytical equations for the confined stress-block parameters have been formulated by Karthik and Mander (2011). As for the confined concrete, the designer needs to define two parameters:

- unconfined compressive strength  $f'_{M,c}$
- confinement efficiency coefficient  $K_{M,e} = 0.1$

The efficiency coefficient is set to 0.1 because the low confining effect transferred through friction. Once these values are chosen, the following set of parameters can be calculated:

- unconfined elastic modulus:

$$E_{M,c} = \begin{cases} 1800 \times \sqrt{f'_{M,c}} & \text{(ksi)} \\ 4,700 \times \sqrt{f'_{M,c}} & \text{(MPa)} \end{cases} \quad (2-31)$$

- unconfined peak strain:

$$\varepsilon_{M,c0} = \begin{cases} 0.0017 + \frac{f'_{M,c}}{8700} & \text{(ksi)} \\ 0.0017 + \frac{f'_{M,c}}{60,000} & \text{(MPa)} \end{cases} \quad (2-32)$$

- volumetric confinement ratio:

$$\rho_s = \frac{4 \times t_o}{D_o} \quad (2-33)$$

- effective lateral confining pressure:

$$f'_{M,\ell} = K_{M,e} \times f_{OS,y} \times \frac{\rho_s}{2} \quad (2-34)$$

- confined-to-unconfined strength ratio:

$$K_M = -1.254 + 2.254 \times \sqrt{1 + 7.94 \times \frac{f'_{M,\ell}}{f'_{M,c}}} - 2 \times \frac{f'_{M,\ell}}{f'_{M,c}} \quad (2-35)$$

- confined compressive strength:

$$f'_{M,cc} = K_M \times f'_{M,c} \quad (2-36)$$

- confined peak strain:

$$\varepsilon_{M,cc0} = \varepsilon_{M,c0} \times [1 + 5 \times (K_M - 1)] \quad (2-37)$$

- secant modulus at peak confined strength, and ratios:

$$E_{M,sec} = \frac{f'_{M,cc}}{\varepsilon_{M,cc0}} \quad (2-38)$$

$$r_M = \frac{E_{M,c}}{E_{M,c} - E_{M,sec}} \quad (2-39)$$

$$n_M = \frac{E_{M,c}}{E_{M,sec}} \quad (2-40)$$

- confined crushing strain, and ratio:

$$\varepsilon_{M,ccu} = 0.004 + 2.5 \times \rho_s \quad (2-41)$$

$$x_{M,u} = \frac{\varepsilon_{M,ccu}}{\varepsilon_{M,cc0}} \quad (2-42)$$

- confined crushing strength:

$$f_{M,ccu} = \frac{f'_{M,cc} \times x_{M,u} \times r_M}{r_M - 1 + x_{M,u}^m} \quad (2-43)$$

Knowing these values, for a given extreme compressive strain  $\varepsilon_{cm}$  on the cross-section, or its ratio  $x_{M,m} = \varepsilon_{cm} / \varepsilon_{M,cc0}$ , one can use the charts of Figure 2.4 or the equations by Karthik and Mander (2011) to determine the equivalent stress-block parameters  $\alpha_{cc}$  and  $\beta_{cc}$ .

#### 2.4.2. Simplified Section Analysis

For this simplified analysis, the concrete material properties are based either on the column confined concrete or on the mortar bed, whichever is weaker: if  $f'_{C,cc} < f'_{M,cc}$  the column concrete controls and  $f'_{cc} = f'_{C,cc}$ , otherwise the mortar bed does and  $f'_{cc} = f'_{M,cc}$ . All other parameters are defined accordingly.

### 2.4.2.1. Decompression Condition

At this loading stage, the gaps at the column ends are still closed and all materials are still elastic. Thus, from basic elastic section analysis methods, the decompression moment can be calculated as:

$$M_{dec} = (P_u + F_{PT,e}) \times \frac{S_C}{A_C} \quad (2-44)$$

where  $P_u$  is the design gravity force,  $F_{PT,e}$  is the total effective post-tensioning force (after time-dependent losses), and the cross-section properties are based on the concrete ring alone (the thickness of the shells can be ignored):

$$A_C = \frac{\pi}{4} \times (D_o^2 - D_i^2) \quad (2-45)$$

$$I_C = \frac{\pi}{64} \times (D_o^4 - D_i^4) \quad (2-46)$$

$$S_C = \frac{2 \times I_C}{D_o} \quad (2-47)$$

### 2.4.2.2. Rocking Joint Analysis

Once the decompression moment is exceeded at a joint, a gap starts opening and the rocking mechanism develops. At any joint rotation  $\theta_j$ , a trial-and-error approach is needed to determine the neutral-axis depth  $c$ , so that translation equilibrium is satisfied:

$$P_u + F_{PT} + F_{ED} - C_C = 0 \quad (2-48)$$

where  $P_u$  is the design gravity force (compression positive),  $F_{PT}$  is the total post-tensioning force at joint rotation  $\theta_j$  (tension positive),  $F_{ED}$  is the total energy-dissipator

force at joint rotation  $\theta_j$  (tension positive), and  $C_c$  is the compressive resultant force on the concrete or mortar (compression positive).

For a given joint rotation  $\theta_j$  and a trial neutral-axis depth  $c$ , the elongation on any single post-tensioning bar  $b$  located at a distance  $d_{PT}^{(b)}$  from the extreme compressive fiber (Fig. 2.1.(c)) is:

$$\Delta L_{PT}^{(b)} = n_j \times \theta_j \times (d_{PT}^{(b)} - c) \quad (2-49)$$

and the corresponding resultant force on that bar is:

$$F_{PT}^{(b)} = F_{PT,e}^{(b)} + \frac{n_j \times \theta_j \times (d_{PT}^{(b)} - c)}{\frac{L_U}{E_{PT} \times A_{PT}^{(b)}} + \frac{1}{K_B^{(b)}}} \leq F_{PT,y}^{(b)} \quad (2-50)$$

where the symbols have the same meaning illustrated earlier in this chapter. The total post-tensioning force due to  $n_{PT}$  bars becomes:

$$F_{PT} = \sum_{b=1}^{n_{PT}} F_{PT}^{(b)} \quad (2-51)$$

Similarly, for a given joint rotation  $\theta_j$  and a trial neutral-axis depth  $c$ , the strain increment on any single energy dissipator  $e$  located at a distance  $d_{ED}^{(e)}$  from the extreme compressive fiber (Fig. 2.1.(c)) is:

$$\epsilon_{ED}^{(e)} = \frac{\theta_j \times (d_{ED}^{(e)} - c)}{L_Y} \quad (2-52)$$

from which the corresponding stress can be calculated based on Eq. 2-17. The resultant force on that dissipator is then:

$$F_{ED}^{(e)} = f_{ED}^{(e)} \times A_{ED}^{(e)} \quad (2-53)$$

where  $A_{ED}^{(e)}$  is the area of energy dissipator  $e$  while all other symbols have the same meaning illustrated earlier in this chapter. The total energy-dissipator force due to  $n_{ED}$  devices bars becomes:

$$F_{ED} = \sum_{e=1}^{n_{ED}} F_{ED}^{(e)} \quad (2-54)$$

As mentioned earlier, the extreme concrete or mortar compressive strain is assumed to have the same value as the joint rotation  $\theta_j$ . Knowing  $\varepsilon_{cm} = \theta_j$ , or the ratio  $x_m = \varepsilon_{cm} / \varepsilon_{cc0}$ , one can use the charts of Figure 2.4 or the equations by Karthik and Mander (2011) to determine the equivalent stress-block parameters  $\alpha_{cc}$  and  $\beta_{cc}$ . For a trial neutral-axis depth  $c$ , the compressive resultant can be calculated as follows (Fig. 2.5):

$$\gamma_C = \cos^{-1} \left( \frac{D_o - 2 \times \beta_{cc} \times c}{D_o} \right) \quad (2-55)$$

$$C_C = \alpha_{cc} \times f'_{cc} \times D_o^2 \times \frac{\gamma_C - \sin \gamma_C \times \cos \gamma_C}{4} \quad (2-56)$$

After the neutral-axis depth is established, the section moment capacity corresponding to the given joint rotation  $\theta_j$  can be calculated as:

$$M = \sum_{b=1}^{n_{PT}} \left( F_{PT}^{(b)} \times y_{PT}^{(b)} \right) + \sum_{e=1}^{n_{ED}} \left( F_{ED}^{(e)} \times y_{ED}^{(e)} \right) + C_C \times y_C \quad (2-57)$$

where  $y_{PT}^{(b)}$  is the distance of post-tensioning bar  $b$  from the section centroid (positive if away from the compression side),  $y_{ED}^{(e)}$  is the distance of energy dissipator  $e$  from the section centroid (positive if away from the compression side), and  $y_C$  is the distance of the concrete or mortar compressive resultant from the section centroid (positive if

towards the compression side):

$$y_c = \frac{D_o \times \sin^3 \gamma_c}{3 \times (\gamma_c - \sin \gamma_c \times \cos \gamma_c)} \quad (2-58)$$

Note that if  $\beta_{cc} \times c$  falls within the hollow core, the concrete area in compression in Eq. 2-56, as well as the location of the compressive resultant, shall be modified to account for the removed material.

#### **2.4.2.3. Reference Yield Condition**

Even though yielding begins when the furthestmost energy dissipator from the compression side reaches its yield strain, stiffness reduction becomes significant when yielding propagates to the location of the tensile resultant. This loading stage can be taken as a reference point to establish yielding at the cross-section level. Under this conditions, it can be assumed that the strain on the extreme tensile dissipator is twice the yield strain:

$$\theta_{jy} = \frac{2 \times \varepsilon_{ED,y} \times L_Y}{d_{ED}^{(e)} - c} \quad (2-59)$$

where  $d_{ED}^{(e)}$  is the distance of the extreme tensile dissipator from the most compressive fiber.

This relationship can be implemented in the above rocking joint analysis to determine by trial-and-error the neutral-axis depth and the corresponding reference yield moment  $M_y$ .



### 2.4.3. Simplified Pushover Relationship

Knowing the moment-rotation relationship for the end joints at a few significant points (e.g. decompression, reference yield, and target drift), a simplified relationship between base-shear and drift-ratio can be quickly derived.

#### 2.4.3.1. First-Order Base Shear

The first-order base shear  $V$  corresponding to a given end moment  $M$ , resisted by a column of length  $H$ , is:

$$V = \frac{n_j \times M}{H} \quad (2-60)$$

where  $n_j = 1$  for a cantilever column and  $n_j = 2$  for a fixed-fixed column.

#### 2.4.3.2. First-Order Displacement and Drift Ratio

End joint rotation, elastic flexural deformation, and elastic shear deformation contribute to the total lateral displacement (Restrepo and Rahman, 2007; Tobolski, 2010):

$$\Delta = \Delta_j + \Delta_f + \Delta_v \quad (2-61)$$

The joint-rotation contribution is given by a rigid-body rotation of the column:

$$\Delta_j = \theta_j \times H \quad (2-62)$$

while the elastic contributions due to flexural and shear deformations are:

$$\Delta_f = \frac{V \times H^3}{3 \times n_j^2 \times E_{C,c} \times I_T} \quad (2-63)$$

$$\Delta_v = \frac{V \times H}{G_{C,c} \times A_{T,s}} \quad (2-64)$$

Assuming reasonable approximations for the concrete shear modulus  $G_{c,c} \cong 0.4 \times E_{c,c}$ , and for the shear area  $A_{T,s} \cong 0.9 \times A_T$ , the elastic displacement becomes:

$$\Delta_f + \Delta_v \cong \frac{V \times H}{E_{c,c}} \times \left( \frac{H^2}{3 \times n_j^2 \times I_T} + \frac{2.8}{A_T} \right) \quad (2-65)$$

where the transformed area and moment of inertia are:

$$A_T = \pi \times \left[ \frac{D_o^2 - D_l^2}{4} + \left( \frac{E_{os}}{E_{c,c}} - 1 \right) \times D_o \times t_o \right] \quad (2-66)$$

$$I_T = \pi \times \left[ \frac{D_o^4 - D_l^4}{64} + \left( \frac{E_{os}}{E_{c,c}} - 1 \right) \times \frac{D_o^3 \times t_o}{8} \right] \quad (2-67)$$

The total drift ratio becomes:

$$\theta = \frac{\Delta}{H} \cong \theta_j + \frac{V}{E_{c,c}} \times \left( \frac{H^2}{3 \times n_j^2 \times I_T} + \frac{2.8}{A_T} \right) \quad (2-68)$$

#### 2.4.3.3. Simplified Consideration of P-Delta Effects

Given the moment at the column base, one can think that part of it balances the overturning induced by the lateral force (second-order base shear  $V_{II}$ ), but another part resists the overturning caused by lateral displacement of the gravity force (P-Delta effect):

$$M = V_{II} \times H + P_u \times \Delta_{II} \quad (2-69)$$

This effect can be approximated by calculating the lateral displacement based on first-order principles, as illustrated earlier; then subtracting from the first-order base shear the amount of overturning resistance taken by P-Delta effects:

$$V_u \cong V - \frac{P_u \times \Delta}{H} = \frac{n_j \times M}{H} - P_u \times \theta \quad (2-70)$$

#### 2.4.3.4. Elastic Stiffness

Following the methods exposed above, the lateral displacement  $\Delta_y$  and the base shear  $V_{u,y}$  corresponding to the reference yield moment  $M_y$  can be calculated. The elastic stiffness can be taken as the secant stiffness through the reference yield point:

$$K = \frac{V_{u,y}}{\Delta_y} \quad (2-71)$$

This stiffness can be used to calculate the elastic period of the bent.

## 2.5. ENERGY DISSIPATOR DETAILS

Particular care needs to be placed into the design and fabrication of energy dissipators, as they are expected to yield and sustain significant inelastic deformations before fracturing. Two alternatives for hysteretic energy dissipators are explored in this thesis: internal dowels with uniform section; and external buckling-restrained devices, with a dog-bone milled bar encased and grouted within a steel pipe. For both solutions Criterion (vi) dictates the minimum yield length  $L_y$  to be provided.

### 2.5.1. Internal Dowels

When using internal dowels, such as stainless-steel deformed bars, as hysteretic dissipators, it is sufficient to unbond the yield segment across the rocking interface by wrapping it with tape (Fig. 2.6(a)). Stainless steel is recommended for this application

because of its high ductility and low sensitivity to corrosion. In fact, cracking concentrates at the rocking interface and the dowels may become exposed to corrosive environment; reducing the dowels sensitivity to corrosion appears to be essential to guarantee a durable performance, as replacing them may be challenging. Beyond the yield segment, enough development length shall be provided within column and footing concrete, to develop the full tensile strength of the dowel bar.

### 2.5.2. External Buckling-Restrained Devices

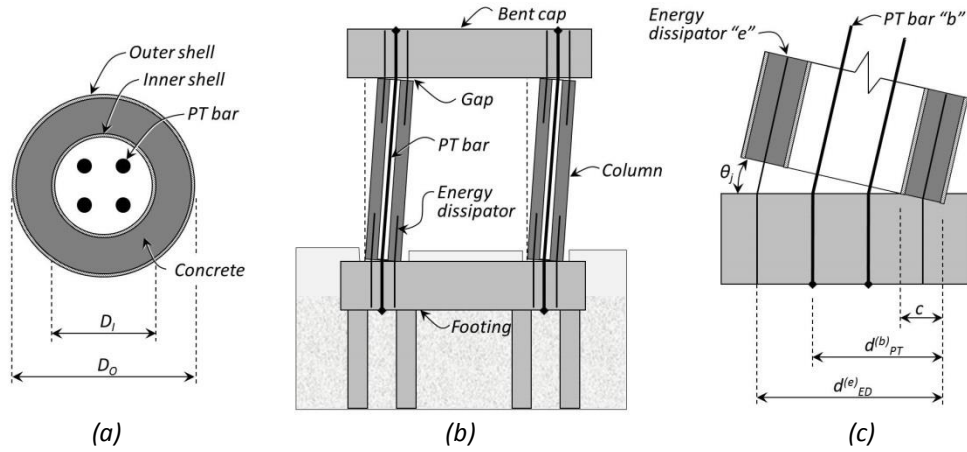
In the case of externally connected buckling-restrained devices, very ductile carbon steel bars can be used. These devices can be easily inspected and replaced, so corrosion sensitivity does not represent an issue. Yielding is forced within a dog-bone milled segment of reduced diameter  $d_{bR}$  (Fig. 2.6(b)) by ensuring that, when it reaches its maximum tensile strength  $f_{ED,O}$ , the stress on the virgin bar ends of diameter  $d_{bV}$  is below  $f_{ED,y}$ . In other words:

$$d_{bR} \leq d_{bV} \times \sqrt{\frac{f_{ED,y}}{f_{ED,O}}} \quad (2-72)$$

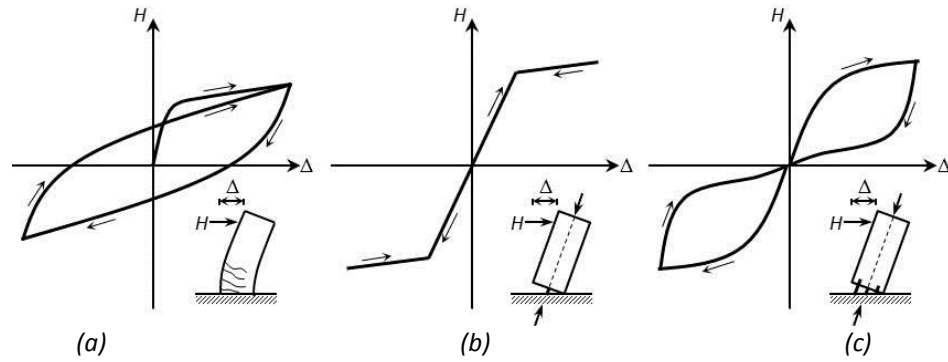
Holden et al. (2003) recommend a circular-tapered transition from  $d_{bR}$  to  $d_{bV}$ , with a taper radius  $r_t = d_{bR}$ , as shown on Figure 2.6(c). A pocket should be created between the bar taper and the grout fill to avoid direct bearing and undesired overstrength when the device is in compression.

Welded connections between the virgin bar ends and brackets attached to the outer shell and the footing have been used for the experimental work described in the

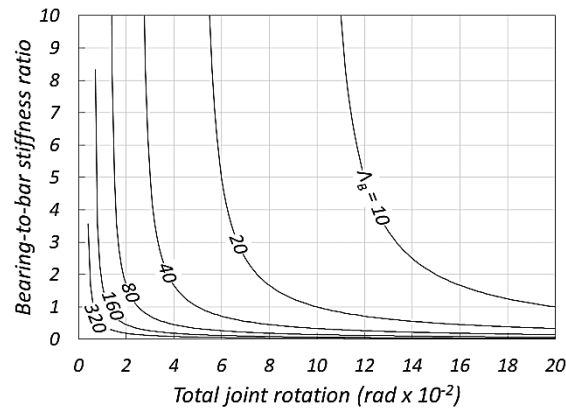
next sections. An undesired effect of welded connections lays in their capacity of transferring moments to the bar ends, while these buckling-restrained devices work better if subjected to axial force only. As a consequence, it is recommended to use true-pin connections between dissipator ends and brackets.



**Figure 2.1** – Schematics of the proposed system: (a) column typical cross-section; (b) bent components and rocking kinematics; (c) joint rotation.



**Figure 2.2** – Hysteretic response: (a) conventional ductile system; (b) purely rocking system; (c) hybrid rocking system.



**Figure 2.3** – Design chart for deformable devices (bearings) in series with post-tensioning bars.

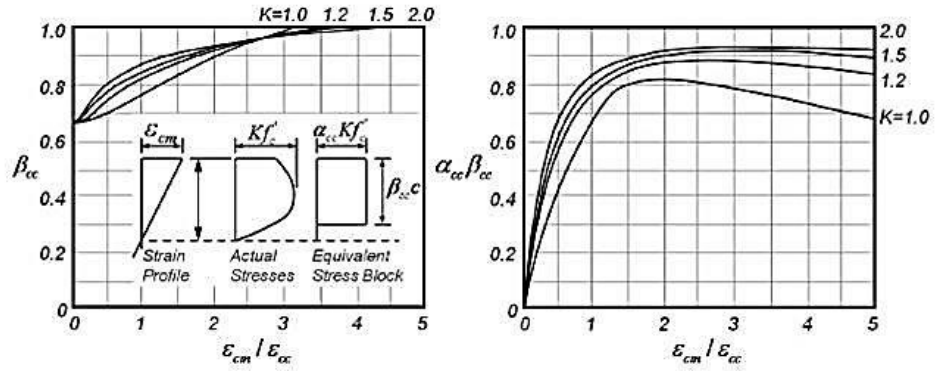


Figure 2.4 – Confined concrete equivalent stress-block parameters (Paulay and Priestley, 1992).

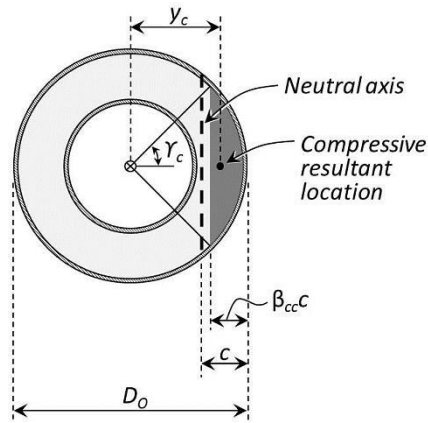


Figure 2.5 – Concrete compressive resultant parameters.

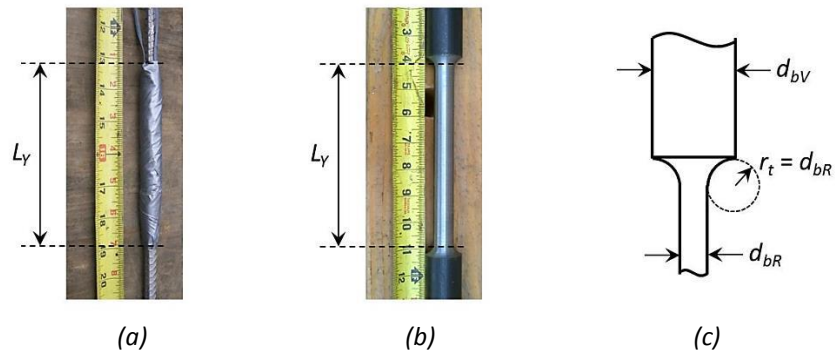


Figure 2.6 – Energy dissipator details: (a) wrapped yield segment of an internal dowel; (b) dog-bone milled bar of a buckling-restrained device; (c) milled bar taper detail.

## Chapter 3

### QUASI-STATIC CYCLIC EXPERIMENTS

#### 3.1. TEST SPECIMENS

Two dual-shell column test units, named Unit 1A and Unit 1B, were tested at the UC San Diego Powell Structural Engineering Laboratories. The specimens were built at 1-to-2.4 length scale. Detailed construction drawings can be found in the Appendix.

##### 3.1.1. Target Performance Objectives

The test specimens were designed for a target drift ratio of 3% without structural damage. At this drift ratio, post-tensioning bars were expected to remain elastic, and the stiffness of the elastomeric bearings was determined accordingly. Also, the energy dissipators were designed not to fracture at the target drift ratio: the milled length of the external buckling-restrained devices and the unbonded length of the internal dowels were calculated on this basis. In order to preserve the system self-centering behavior at the target drift ratio, the mortar bed was designed to crush under larger lateral displacements. Energy dissipation coefficients  $\Lambda_D = 0.30$  and  $\Lambda_D = 0.37$  were provided to Unit 1A and Unit 1B, respectively.



### 3.1.2. Specimens Overview

The test configuration for the two dual-shell column units is shown in Figure 3.1.

Both test units included:

- composite column
- footing
- load stub
- mortar bed
- energy dissipators
- post-tensioning bars
- elastomeric pads.

Unit 1A was equipped with external buckling-restrained energy dissipators, while Unit 1B incorporated internal dowel bars. Given their precast nature, footing, column, and load stub were cast separately; after concrete had hardened, they were initially assembled as Unit 1A. When testing of Unit 1A was completed, the three components were taken apart, the column was flipped upside-down, and they were reassembled as Unit 1B. In fact, only the bottom region of the column was subjected to large strains and minor damage during the first test, while the other end was still free of any damage. By doing this, it was possible to take advantage of both ends of the element.

The overall column diameter was  $D_o = 0.51$  m (20 in.), its clear height was  $H_c = 0.84$  m (33 in.), and the total cantilever span from the base to the point of lateral load application was  $H = 1.13$  m (44.5 in.). A low aspect ratio of  $H/D_o = 2.2$  was chosen to subject the specimens to more critical conditions of shear sliding at the base.

Moreover, a short element can accommodate short post-tensioning bars, which are more susceptible to yielding due to their lower axial deformability.

### 3.1.3. Composite Column

The column outer shell had a diameter  $D_o = 0.51$  m (20 in.) and a thickness  $t_o = 6.4$  mm (0.25 in.), that is  $D_o/t_o = 80$ . The inner shell had a diameter  $D_i = 0.36$  m (14 in.) and a thickness  $t_i = 3.2$  mm (0.125 in.), that is  $D_i/t_i = 112$ . Details are shown in Figure 3.2. The shells were obtained by folding and welding plates made of Grade 50 A572 steel, with yield stress of 345 MPa (50 ksi). In practice, the inner shell would be a corrugated drainage pipe (Restrepo et al., 2011).

The outer shell was equipped with six radially distributed 12.7-mm (0.5-in.) thick steel brackets, welded to the external surface (Fig. 3.2(d)), for the connection of the buckling-restrained dissipators of Unit 1A. Six 50.8-mm (2-in.) diameter, 0.46-m (18-in) long, corrugated metal ducts were embedded in the concrete for the installation of the internal dowels of Unit 1B (Fig. 3.2(e)). Three circumferential 9.5-mm (3/8-in.) weld beads on the internal surface of the outer shell provided tensile stress transfer between the dowels and the shell (Fig. 3.2(f)).

High-performance, normal-weight concrete was used to cast the column, with a specified compressive strength of 62 MPa (9.0 ksi) at 56 days. The compressive strengths measured at 28 days, 49 days (day of testing of Unit 1A) and 96 days (day of testing of Unit 1B) were 66 MPa (9.5 ksi), 70 MPa (10.2 ksi), and 72 MPa (10.4 ksi), respectively. After hardening, the concrete surfaces were roughened to improve shear-friction between column and mortar bed, as shown on Figure 3.2(g). A bond-breaker film was applied to

the bottom surface of the column, to allow separation from the mortar bed and opening of the gap.

#### **3.1.4. Footing**

The footing consisted of a 1.83-m (6-ft) long, 1.22-m (4-ft) wide, 0.61-m (2-ft) deep reinforced concrete block (Fig. 3.3), cast with the same concrete used for the column.

Ten #6 (19-mm diameter) top and bottom “U” bent bars provided longitudinal reinforcement, while ten #3 (9.5-mm diameter) 4-legs stirrups constituted the transverse reinforcement. Two #3 bars were placed along each side face of the foundation as skin reinforcement. All the reinforcement consisted of Grade 60 A615 steel bars, with a specified yield strength of 420 MPa (60 ksi).

Two series of six 50.8-mm (2-in) diameter corrugated steel ducts were placed in the footing for future installation of the energy dissipators. Four PT bars anchorages were also preassembled and embedded in the footing. A #3 (9.5-mm diameter) spiral at 76.2-mm (3-in) pitch, with a diameter of 660 mm (26 in), was placed around the corrugated steel ducts and PT-bar anchorages to confine the concrete (Fig. 3.3(d)). After concrete hardened, the footing surface below the column base was roughened to improve shear-friction between footing and mortar bed.

The footing was connected to the strong floor by means of four 44.5-mm (1.75-in) diameter tie-down rods tensioned at 979 kN (220 kips) each. Four 63.5-mm (2.5-in) diameter PVC pipes were provided in the footing to accommodate these rods.

### **3.1.5. Load Stub**

The load stub on the top of the column consisted of a 2.44-m (8-ft) long, 0.76-m (30-in) wide, 0.51-m (20-in) deep reinforced concrete beam (Fig. 3.4), cast with the same concrete used for the column.

Four #6 (19-mm diameter) top and bottom “U” bent bars provided longitudinal reinforcement, while sixteen #3 (9.5-mm diameter) 2-legs stirrups at 150-mm (6-in) on-center constituted the transverse reinforcement. All the reinforcement consisted of Grade 60 A615 steel bars, with a specified yield strength of 420 MPa (60 ksi).

Four horizontal 63.5-mm (2.5-in) diameter PVC pipes were provided in the load stub for connecting the actuator. Four vertical 50.8-mm (2-in) diameter PVC ducts allowed the post-tensioning bars to run through the load stub. After concrete hardened, the load-stub surface right above the column top was roughened to improve shear-friction between load stub and hydrostone.

Two vertical 63.5-mm (2.5-in) diameter PVC pipes were placed close to the beam ends; tie-down rods ran through these pipes, to apply vertical forces simulating gravity.

### **3.1.6. Mortar Bed**

A 12.7-mm (0.5-in.) thick mortar bed was cast at the column-to-footing connection, to compensate for expected in-situ construction tolerances. A high-performance metallic grout mix placed at plastic consistency in the form of a mortar bed was used in Unit 1A. The mortar compressive strengths were 45.8 MPa (6.6 ksi) and 50.4 MPa (7.3 ksi) at 21 and 23 days (day of testing of Unit 1A), respectively. For the column-footing joint of Unit 1B the same product was used, but polypropylene fibers were added

in the proportion of 0.035% by weight to increase the mortar toughness; strengths of 53.4 MPa (7.8 ksi) and 52.9 MPa (7.7 ksi) were obtained at 28 and 35 days (day of testing Unit 1B).

A wood template was employed to guide the column, and 12.7-mm (0.5-in.) diameter nylon rods were used as shims to hold the column in place while the mortar was wet (Fig. 3.5(a)). The mortar was scraped from underneath the outer shell (Fig. 3.5(b)), to prevent the shell from causing premature crushing under direct compression transfer, a problem noted in earlier experiments (Restrepo et al., 2011). All interface surfaces had been previously roughened to improve shear-friction transfer. Since the upper joint between column and load stub was not critical because of the low bending moment at this location, hydrostone was placed to match the two pieces there.

### **3.1.7. Energy Dissipators**

#### ***3.1.7.1. Unit 1A: External Buckling-Restrained Devices***

Six external, buckling-restrained energy dissipators were incorporated in test Unit 1A, radially distributed around the column perimeter (Fig. 3.6). These devices consisted of steel bars with a reduced diameter over a specific length, where dissipation was provided by material hysteresis. Each 343-mm (13.5-in.) long steel bar had an original diameter of 25.4 mm (1 in.), which was reduced to 14.3 mm (9/16 in.) in the 165-mm (6.5-in.) long milled portion. Hot-rolled A576 steel was used, with a measured yield strength of 331 MPa (48 ksi), ultimate (peak) tensile strength of 490 MPa (71 ksi), and strain of 20% at the ultimate tensile strength.

In order to prevent buckling, the milled part was encased and grouted within a

steel pipe; grease was used to reduce friction between bar and grout. Mastic tape, about 3-mm (0.125-in.) thick, was applied along the tapered segments, to create pockets and reduce bearing of the non-milled ends on the grout.

The external dissipators were welded to brackets connected to the footing and to the column outer-shell. All brackets were obtained from 12.7-mm (0.5-in.) thick A572 Grade 50 steel plates, with a specified yield stress of 345 MPa (50 ksi), and were proportioned to resist the ultimate strength of the devices. The footing brackets were welded to #6 Grade 60 A706 steel reinforcing bars, grouted within prepositioned ducts. The grout, mixed at fluid consistency, had compressive strength equal to 47.1 MPa (6.8 ksi) on the day of testing.

All welds were performed with an E70 electrode (strength at least equal to 480 MPa or 70 ksi) and were designed to withstand the ultimate strength of the dissipators.

#### ***3.1.7.2. Unit 1B: Internal Dowels***

Unit 1B was equipped with six internal dowels at the column-footing joint, acting as internal energy dissipators (Fig. 3.7). Grade 75 316LN stainless steel #4 deformed bars were used for this purpose. The bars were wrapped with duct-tape for a length of 178 mm (7 in.) across the column-footing interface to inhibit the bond along it. Material testing showed a yield stress for the stainless steel bars of 745 MPa (108 ksi), an ultimate (peak) tensile strength of 889 MPa (129 ksi), and a strain of 15% at the ultimate tensile strength.

The dowels were first grouted within corrugated steel ducts predisposed in the footing, then, after column placement on the footing, they were grouted within the column ducts. The footing grout, mixed at fluid consistency, had compressive strength of

52.7 MPa (7.6 ksi) on the day of testing, while the column grout attained a compressive strength of 59.2 MPa (8.6 ksi).

### 3.1.8. Post-Tensioning Bars

Four 34.9-mm (1-3/8 in.) diameter, A722 Grade 150 threaded bars provided the post-tensioning force to both units (Fig. 3.8). The total effective post-tensioning force was 845 kN (190 kips) in Unit 1A and 890 kN (200 kips) in Unit 1B, after all losses. Jacking forces of 311 kN (70 kips) were applied to each bar, to compensate for lock-off and bearing creep losses. The post-tensioning bars were screwed into anchorage devices prearranged in the footing, allowing for bar replacement (Fig. 3.8(a)). They ran inside the column hollow core, sleeved in ducts filled with fluid grout to protect them from corrosion (Fig. 3.8(b)). Additional bar deformability was provided by placing, in series with the post-tensioning bars, rubber (Unit 1A) or polyurethane (Unit 1B) bearings, between the top anchorage plates and the load stub.

Each PT-bar anchorage was made of a PT-bar segment, with the same 34.9 mm (1-3/8 in) diameter as the connecting PT bar, and a length of 0.5 m (19.5 in). A plate and a nut were provided at the lower end, while a coupler was provided at the upper end to accommodate the bar (Fig. 3.8(c) and (d)). In order to rely exclusively on bearing of the bottom plate against the concrete, the bar segment was unbonded by duct-tape wrapping. This detail was intended to prevent post-tensioning losses due to bar slippage following bond failure. Summing the main bar and the anchorage segment, the total unbonded bar length was 2.16 m (85 in.).

### **3.1.9. Elastomeric Pads**

#### ***3.1.9.1. Unit 1A: Natural Rubber Pads***

A bearing consisting of five square 80-Shore-A hardness rubber pads was provided to each post-tensioning bar in test Unit 1A (Fig. 3.9). The pads were 190.5 mm (7.5 in.) square by 25.4 mm (1 in.) thick and had a central hole with diameter of 41.3 mm (1-5/8 in.) to accommodate the PT bars. These pads were stacked and alternated with 3.2 mm (1/8 in.) thick square steel shims of the same plan dimensions. These shims were bonded to the pads by an epoxy adhesive, with the scope of limiting lateral dilation of the rubber pads under compression; however this practice proved to be ineffective, with bond failure between the connected parts. Each bearing had stiffness equal to  $1.46 \times 10^5$  kN/m (836 kip/in) when tested at ambient temperature and at a rate varying between 40 and 120 kips/sec.

#### ***3.1.9.2. Unit 1B: Polyurethane Pads***

A bearing consisting of four 90 Shore-A hardness polyurethane pads was provided to each post-tensioning bar in test Unit 1B (Fig. 3.10). The pads had diameter of 190.5 mm (7.5 in.), thickness of 47.6 mm (1-7/8 in.), and a central hole with diameter of 47.6 mm (1-7/8 in.) to accommodate the PT bars. The pads were stacked and alternated with 190.5 mm (7.5 in.) diameter by 3.2 mm (1/8 in.) thick circular steel shims. These shims were bonded to the pads by an epoxy adhesive, with the scope of limiting lateral dilation of the polyurethane pads under compression; however this practice proved to be ineffective, with bond failure between the connected parts. Each bearing had stiffness equal to  $4.38 \times 10^4$  kN/m (250 kip/in) when tested at ambient temperature and at a rate of



0.5 kips/sec.

## 3.2. MATERIAL PROPERTIES

### 3.2.1. Concrete

High-performance concrete was used to cast column, load stub, and footing. The compressive strength was measured on standard cylinders with diameter of 152 mm (6 in) and height of 305 mm (12 in). Tests were performed at 28 days after casting, at 49 days (day of test of unit 1A) and at 96 days (day of test of unit 1B). Results are listed in Table 3.1. Each value is the average from three specimens. The measured values were larger than the specified strength of 62 MPa (9 ksi) at 28 days.

Consistency and workability of the concrete were assessed through the standard slump (Abram's cone) test. The resulting slump was equal to 216 mm (8.5 in), indicating high workability of the concrete. A value larger than 200 mm (8 in) was required to ensure adequate consolidation.

**Table 3.1** – Measured concrete compressive strength.

Age (days)	Compressive strength	
	(MPa)	(ksi)
28	65.5	9.5
49 (DoT Unit 1A)	70.2	10.2
96 (DoT Unit 1B)	71.8	10.4

### 3.2.2. Mortar

The mortar layer between column and footing for both test units was obtained from BASF Embeco 885 cementitious grout at plastic consistency. This material is a prepackaged hydraulic cement-based, metallic-aggregate, high strength, non-shrink grout, with an extended working time. This grout meets the requirements of ASTM C 1107. For the specific application it was mixed with a low percentage of water (20% in volume).

The mortar bed in Unit 1B was reinforced with Durafiber polypropylene fibers, meeting ASTM C 1116-00 standards. Fibers were added in a proportion of 0.037% by weight. Fibers inhibit the growth of cracks once they form, thus maintaining the integrity of the mortar and delaying crushing under large compressive strains.

Compressive strengths were measured on standard cylinders with diameter of 51 mm (2 in) and height of 102 mm (4 in). Values are reported in Tables 3.2 and 3.3 for Unit 1A and Unit 1B, respectively. Each value is the average from three specimens. For comparison, the manufacturer-specified strengths for the grout with plastic consistency at 7 and 28 days were 62 MPa (9 ksi) and 76 MPa (11 ksi), respectively.

**Table 3.2** – Measured mortar compressive strength, Unit 1A.

Age (days)	Compressive strength	
	(MPa)	(ksi)
23 (DoT Unit 1A)	50.4	7.3
29	46.4	6.7

**Table 3.3** – Measured mortar compressive strength, Unit 1B.

Age (days)	Compressive strength	
	(MPa)	(ksi)
28	53.4	7.8
35 (DoT Unit 1B)	52.9	7.7

### 3.2.3. Grout

BASF Embeco 885, mixed at fluid consistency with a larger percentage of water (16.8% in weight) was employed for grouting:

- buckling-restrained energy dissipators
- post-tensioning bar ducts for corrosion protection
- external dissipator anchorages into the footing
- internal dissipator into footing and column ducts.

Compressive strengths were measured on standard cylinders with diameter of 51 mm (2 in) and height of 102 mm (4 in). Values are reported in Tables 3.4 to 3.6. Each value is the average from three specimens. For comparison, the manufacturer-specified strengths for the grout with fluid consistency at 7 and 28 days were 48 MPa (7 ksi) and 62 MPa (9 ksi), respectively.

**Table 3.4** – Measured grout compressive strength, Unit 1A external dissipator anchorages into footing.

Age (days)	Compressive strength	
	(MPa)	(ksi)
18 (DoT Unit 1A)	47.1	6.8

**Table 3.5** – Measured grout compressive strength, Unit 1B internal dissipator dowels into footing.

Age (days)	Compressive strength	
	(MPa)	(ksi)
41 (DoT Unit 1B)	52.7	7.6

**Table 3.6** – Measured grout compressive strength, Unit 1B internal dissipator dowels into column.

Age (days)	Compressive strength	
	(MPa)	(ksi)
27 (DoT Unit 1B)	59.2	8.6

**Table 3.7** – Measured steel mechanical properties.

Material	Yield stress		Yield strain	Elastic modulus		Peak stress		Peak strain
	(MPa)	(ksi)	(%)	(MPa)	(ksi)	(MPa)	(ksi)	(%)
A576	331	48	0.15	220,632	32,000	490	71	20.0
316LN	745	108	0.37	200,000	29,000	889	129	15.0

### 3.2.4. Energy Dissipator Steel

Hot rolled, ASTM A576 Grade 1018 carbon steel bars were used for the external dissipators; a 25.4-mm (1-in) diameter bar was tested in monotonic tension to characterize the material. The internal dissipators consisted of of 316LN, Grade 75 stainless-steel reinforcing bars; a 12.7-mm (0.5-in) diameter bar was tested in monotonic tension to characterize the material. Since 316LN steel does not exhibit a yield plateau, the yield point has been determined with the 0.2% offset method.

Yield stresses and strains, elastic moduli, and ultimate stresses and strains (at peak) are reported in Table 3.7 for the two materials. The corresponding full stress-strain curves are shown on Figure 3.11.

### 3.2.5. Rubber Pads

The rubber bearings provided to the post-tensioning bars of Unit 1A consisted of SA-47 rubber pads, produced by Fabreeka International. These pads are made of recycled rubber compounds and synthetic fiber reinforcement. Randomly oriented fibers enhance compressive strength, stiffness, and tensile strength when compared to unreinforced or virgin rubber.

The design of the bearings was initially based on the stiffness provided by manufacturer's specifications; then it was refined on the basis of cyclic compressive tests

performed on two rubber pads. The resulting elastic modulus under cyclic loading was 524 MPa (76 ksi). During testing the material underwent significant creep deformations, even under cyclic loading. Moreover, the behavior appeared to depend on the loading rate, with larger stiffness at higher rates.

### **3.2.6. Polyurethane Pads**

The polyurethane bearings provided to the post-tensioning bars of Unit 1B consisted of adiprene pads. This material, a thermosetting elastomer characterized by elevated toughness, combines resilience and high load-bearing capacity with resistance to impact, abrasion, compression set and degradation by oxygen, ozone and oil. In addition to the properties distinguishing it from conventional elastomers, Adiprene also differs in its physical form: it is a liquid polymer which is mixed with a curing agent and can be fabricated by casting.

The design of the bearings was initially based on the stiffness provided by manufacturer's specifications; then it was refined on the basis of a cyclic compressive test performed on one polyurethane disc. The resulting elastic modulus under cyclic loading was 331 MPa (48 ksi). During testing the material underwent significant creep deformations, even under cyclic loading. Moreover, the behavior appeared to depend on the loading rate, with larger stiffness at higher rates.

## **3.3. INSTRUMENTATION**

The test specimens were instrumented to measure deformations, displacements, and forces during testing. Strain gages, potentiometers, and load cells were used at this

scope, respectively. More details about sensor locations can be found in the Appendix.

### **3.3.1. Overall Displacement and Rotation Measurements**

A cable-extension displacement transducer, referred to as a horizontal string potentiometer, was connected to the load stub at the lateral loading point, to record the lateral displacement of the column and control the actuator (Fig. 3.12(a)).

Two inclinometers were mounted one on the foundation and one on top of the load stub as shown on Figure 3.12(b), to measure these components rotations.

### **3.3.2. Column Deformation Measurements**

Four vertical spring-loaded displacement transducers were installed on the north face and four on the south face of the column (Fig. 3.12(a)), to evaluate the average column curvature between their mounting rods.

Two horizontal spring-loaded displacement transducers were added at the column base in Unit 1B, to monitor eventual shear sliding.

### **3.3.3. Outer-Shell Strain Measurements**

Figures 3.13(a) and 3.13(b) show the strain gage locations on the outer shell for Units 1A and 1B, respectively. Five 5-mm horizontal strain gages, attached to the north and south faces of the outer shell, were used to record hoop stresses induced on the shell by lateral dilation of compressed concrete. Five 5-mm vertical strain gages were applied to the north face of the column to measure longitudinal stresses on the shell. Finally, three 5-mm strain gages, arranged in a delta-rosette configuration, were attached to the

east and west sides of the specimen to determine the shear strains.

In Unit 1B eight additional 5-mm vertical strain gages were applied to the north-east and south-west faces of the outer shell, in front of the internal dissipators; these sensors were intended to record the strain induced on the shell by the stresses transferred from the internal dowels.

#### **3.3.4. Post-Tensioning Bar Strain Measurements**

Strain gages were used to measure the elongation of two diametrically opposite post-tensioning bars (north-east and south-west) in both Units 1A and 1B (Fig. 3.14). Two sensors were applied to each bar, in order to capture axial and flexural deformations.

#### **3.3.5. External Energy Dissipator Response Measurements**

Two diametrically opposite external dissipators (north-west and south-east) were instrumented in Unit 1A, as illustrated on Figure 3.15(a). Each device was provided with two strain gages and a spring-loaded displacement transducer. The strain gages, attached to the virgin portion of the bar which was expected to remain elastic, were used to obtain the dissipator forces through elasticity relationships. The displacement transducer, connected to the dissipator bar ends right above and below the casing, recorded the axial deformation and allowed to capture the hysteretic response of the device.

#### **3.3.6. Internal Energy Dissipator Strain Measurements**

Strain gages were applied to two diametrically opposite internal dissipators (north-east and south-west) in Unit 1B, as shown on Figure 3.15(b). Four sensors were

mounted on each bar, to measure axial and flexural deformations at two locations of the unbonded segment.

### **3.3.7. Gravity-Equivalent Load Measurements**

Load cells were used to monitor the axial force on two tie-down rods, tensioned by vertical hollow plunger jacks, intended to apply a gravity-equivalent load to the specimen. They were mounted between the load stub and the jacks, as shown on Figure 3.1.

### **3.3.8. Miscellaneous**

In addition to active measurement provided by the instrumentation described above, three video cameras were mounted on site: one zooming on the column-footing joint from north; one recording the whole column from the east side; and the last one, installed on the reaction wall, and recording the whole test unit. Furthermore, the specimen response was documented through digital photos and notes.

## **3.4. LOADING PROTOCOL AND TEST OUTCOMES**

### **3.4.1 Loading Protocol**

A vertical force, simulating gravity loads, was applied to the test units by two vertical hollow hydraulic plunger jacks, positioned above the load stub and connected to the strong floor by one 31.8-mm (1-1/4 in) diameter tie-down rod each (Fig. 3.1). Actual axial forces of 293 kN (63 kips) and 268 kN (60 kips) were applied to Unit 1A and Unit 1B, respectively.



Keeping the gravity force constant, the test unit was subjected to quasi-static reversed cyclic loading by a horizontal actuator in the north-south direction, with positive values to the north. After three lateral force-controlled cycles to a base shear coefficient of  $\pm 0.4$  and three to  $\pm 0.8$  (Fig. 3.16(a)), the test proceeded in lateral displacement control (Fig. 3.16(b)). Three cycles to  $\pm 0.5\%$  drift ratio and three to  $\pm 0.75\%$  were completed. Subsequent cycles consisted of two large-amplitude cycles, followed by a lower one at a level corresponding to the previous large drift level: drift ratios of  $\pm 1\%$ ,  $\pm 1.5\%$ ,  $\pm 2\%$ ,  $\pm 3\%$ ,  $\pm 5\%$ ,  $\pm 7.5\%$ , and  $\pm 10\%$  were targeted.

### **3.4.2. Normalization of Response Parameters**

Lateral displacements have been normalized by the height of the lateral force application point above the column base, and thus, expressed as drift ratios; lateral forces have been normalized by the applied vertical load (equivalent to the weight) and thus transformed into base shear coefficients. Post-tensioning forces have been normalized by their initial value after application of gravity loads. Energy-dissipator stresses have been normalized by the material yield stress, while the neutral axis depth has been normalized by the column outer diameter.

For drift ratios larger than 0.3%, it was observed that the base joint rotation was contributing to more than 90% of the lateral displacement: as a consequence, drift ratios and joint rotations practically coincided and only drift ratios have been considered in the result analysis.

### 3.4.3. Outcomes for Unit 1A

#### 3.4.3.1. Mortar Bed

Testing of Unit 1A resulted in joint opening at the column-mortar bed interface during the cycles to a base shear coefficient of  $\pm 0.8$ ; as a consequence a first loss of stiffness was observed on the diagram of Figures 3.17(a) and 3.17(b). The mortar bed started to flake off during the  $\pm 1.5\%$  drift ratio cycles, and showed large flaking off and some visible permanent plastic deformation, without crushing, on the north and south sides (extreme fibers) during the  $\pm 3\%$  drift ratio cycles, causing a loss of stiffness.

The mortar bed started to crush during the  $\pm 5\%$  drift ratio cycles, with significant loss of stiffness and self-centering ability. This corresponds to cycles 25 and 26 in Figure 3.18(a), where residual drift ratios larger than 1.5% can be observed. A significant loss of post-tensioning force was recorded upon mortar crushing during cycle 26, as shown on Figure 3.19(a) where the normalized residual post-tensioning force at the end of each cycle is plotted; it was also observed that post-tensioning bars were always far from yielding throughout the test. Extensive crushing of the mortar bed was visible at the end of the test, as shown on Figure 3.20(a).

#### 3.4.3.2. Energy Dissipators

External dissipators started bending between the buckling-restrained central portion and the end connections during the  $\pm 3\%$  drift ratio cycles, due to the rotation imposed by the rocking body motion (Fig. 3.21(a)). The north-west dissipator fractured during the first negative cycle to  $-7.5\%$  drift ratio, nearly at peak displacement. Two other dissipators fractured on the south side during subsequent cycles. Each fracture

corresponded to a sudden jump on the graph of Figure 3.17(b). Due to failure of three out of six dissipators, the test was interrupted after the first cycle to  $\pm 10\%$  drift ratio.

The hysteretic stress-strain response of the north-west external dissipator is shown on Figure 3.21(b) up to the first cycle to  $+5\%$  drift ratio. Average strains were determined with a linear potentiometer, connected to the dissipator bar right above and below the casing. Stresses were calculated from the elastic strains, measured with paired strain gages along the non-disturbed ends of the steel bar. It can be noticed that the compressive stresses on the device are larger than the tensile ones; this is due to partial composite behavior between the milled bar and the grout-and-pipe casing, induced by friction along the milled segment and by bearing of the bar non-milled ends on the grout.

A non-conventional shape of the hysteretic loops may also be observed; this may be attributed to two sources of inaccuracy. First, the dissipator axial force was calculated from the axial strains measured by strain gages applied to the elastic non-milled end segments; however, these segments were subjected to bending during the test, which may have affected the determination of the axial force. Second, the average axial strain of the yielding segment was calculated from the relative displacement between two sections right outside the casing; bending of the end segments caused relative rotations between these two sections, which in turn affected the measurement of the relative displacement.

#### ***3.4.3.3. Composite Column***

Residual compressive deformation of the column concrete between the shells, and permanent deformation of the shells themselves due to concrete dilation, was observed at the column base when the column was taken apart from the footing at the end of the test

(Fig. 3.22(a)).

### **3.4.4. Outcomes for Unit 1B**

#### ***3.4.4.1. Mortar Bed***

Similarly to Unit 1A, joint opening occurred in Unit 1B at the column-mortar bed interface during the cycles to a base shear coefficient of  $\pm 0.8$ ; as a consequence a first loss of stiffness was observed on the diagram of Figures 3.17(c) and 3.17(d). The mortar bed started to flake off during the  $\pm 2\%$  drift ratio cycles, and showed large flaking off and some visible permanent compressive deformation, without crushing, on the north and south sides (extreme fibers) during the  $\pm 3\%$  drift ratio cycles, causing a loss of stiffness.

Mortar bed crushing progressed during the  $\pm 5\%$  drift ratio cycles, but not abruptly; it became extensive under the  $\pm 7.5\%$  drift ratio cycles, when the stiffness was evidently reduced as well as the self-centering capacity. This corresponds to cycles 28 and 29 in Figure 3.18(b), where residual drifts in the order of 1.5% can be observed. A comparison between the residual post-tensioning force of Figures 3.19(a) and 3.19(b) shows that post-tensioning losses due to mortar crushing in Unit 1B were less pronounced than in Unit 1A; it was also observed that post-tensioning bars were always far from yielding throughout the test. Extensive crushing of the mortar bed was visible at the end of the test, as shown on Figure 3.20(b).

#### ***3.4.4.2. Energy Dissipators***

The first dissipator fractured on the north side during the second negative cycle to  $-7.5\%$  drift ratio, nearly at peak displacement. A second dissipator fractured on the north

side and two on the south side during subsequent cycles. Each fracture corresponded to a sudden jump on the graph of Figure 3.17(d).

Longitudinal strains were measured on the outer shell in correspondence of two diametrically opposite dissipating dowels. The longitudinal strain profiles measured in front of the south-west dowel, from the base of the shell to the end of the dowel, are plotted in Figure 3.23. Positive cycles induce tension while negative cycles compression. It can be observed that during cycles up to  $\pm 1\%$  drift ratio transfer of tension from the dowel to the shell is distributed within 0.4 times the outer diameter from the base; at larger amplitude cycles it concentrates within 0.2 diameters; above this length, strains remain about constant. Large compressive strains tend to develop close to the base, but no yielding was observed up to  $\pm 5\%$  drift ratio cycles.

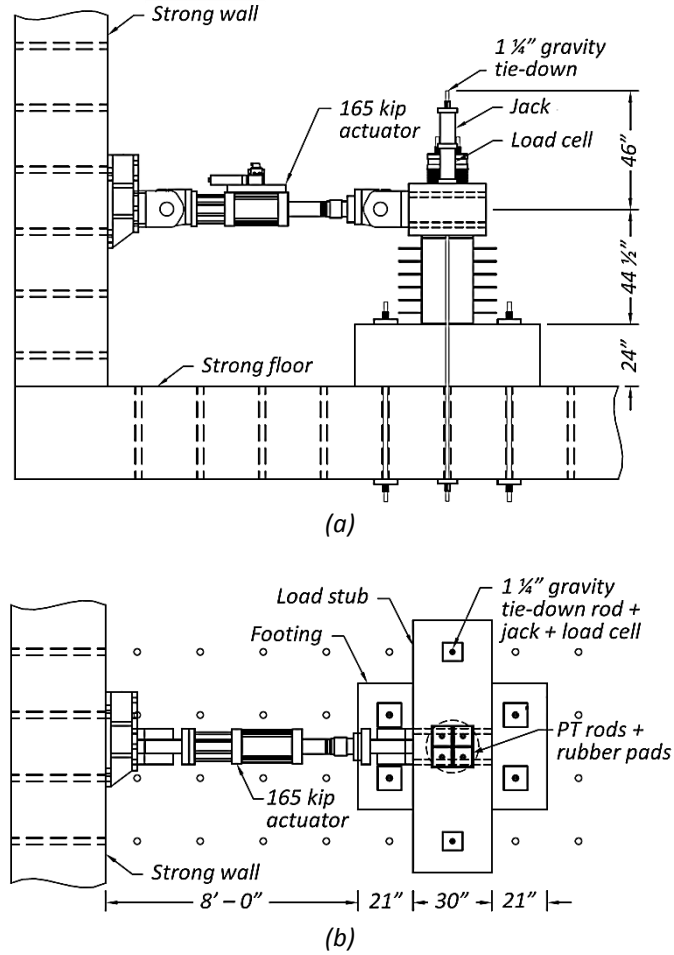
#### **3.4.4.3. Composite Column**

Residual compressive deformation of the column concrete between the shells, and permanent deformation of the shells themselves due to concrete dilation, was observed at the column base when the column was taken apart from the footing at the end of the test (Fig. 3.22(b)).

#### **3.4.5. Comparison between Unit 1A and Unit 1B**

The main difference in the hysteretic response between Units 1A and 1B shows the importance of preventing mortar bed crushing in order to maintain self-centering behavior. Adding polypropylene fibers to the grout mix used in Unit 1B improved the material toughness, thus delaying its crushing and the consequent loss of post-tensioning

force. This resulted in self-centering capacity extended to cycles to  $\pm 5\%$  drift ratio, where Unit 1A was already displaying significant residual displacements. Moreover, larger neutral axis depths were measured on Unit 1B for cycles 7 and beyond compared to Unit 1A (Fig. 3.24), meaning that under the same joint rotations larger compressive strains were sustained by the mortar in Unit 1B before crushing.

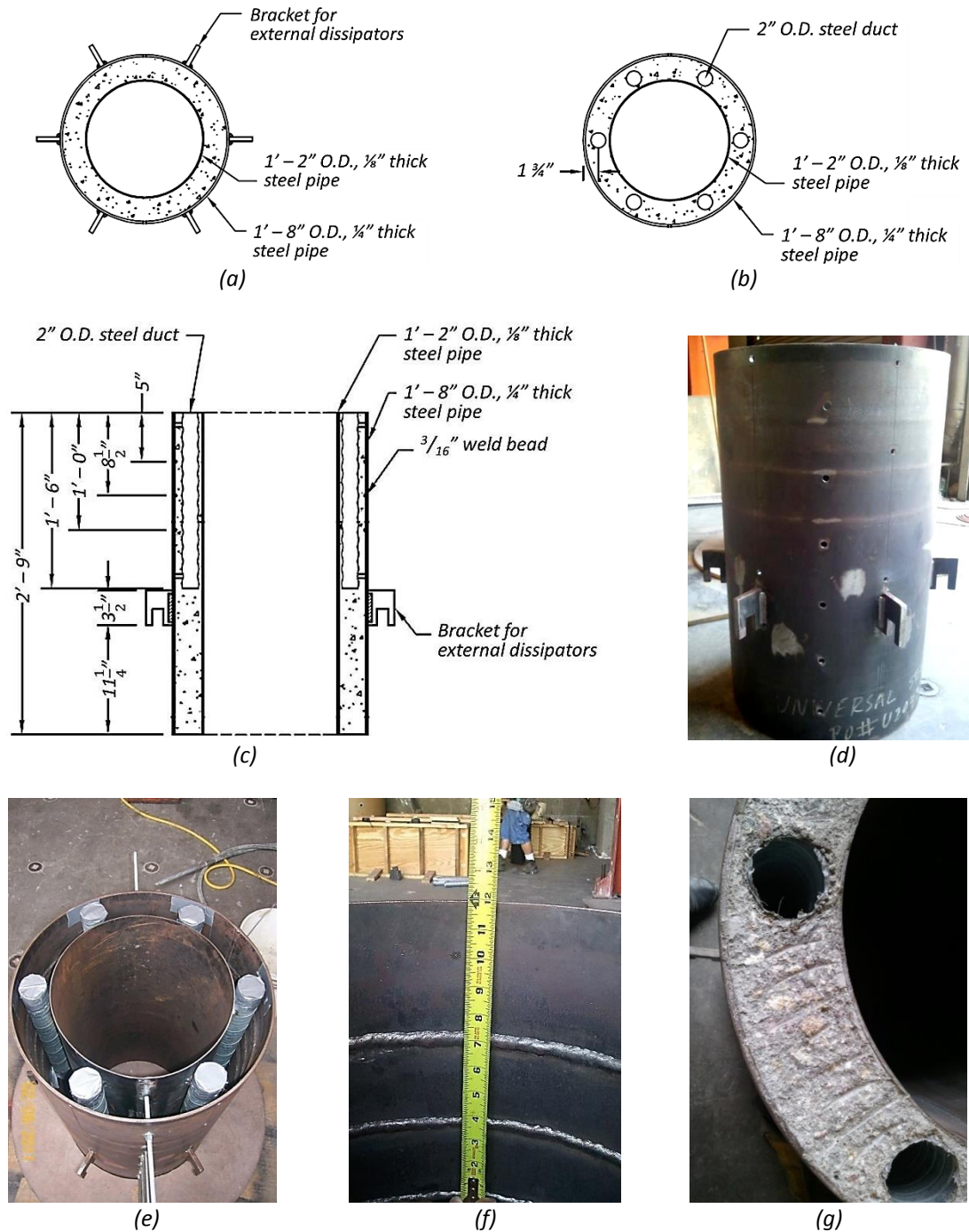


(c)



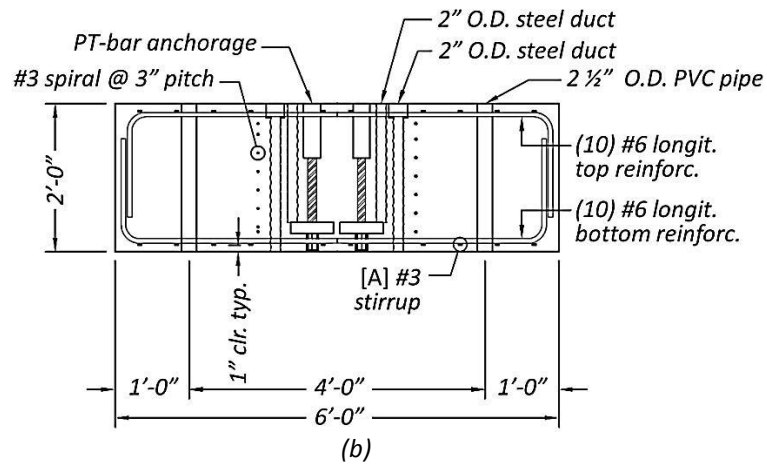
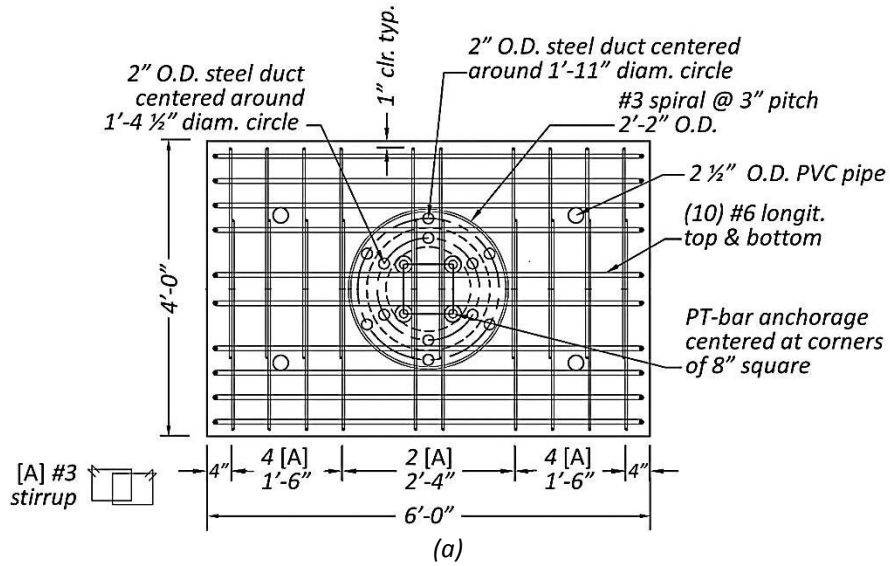
(d)

**Figure 3.1** – Test configuration and dimensions: (a) side elevation; (b) plan view; (c) overview of Unit 1A; (d) overview of Unit 1B.



**Figure 3.2** – Column details: (a) Unit 1A base cross-section; (b) Unit 1B base cross-section; (c) column longitudinal section; (d) outer shell with brackets for connection of external dissipators; (e) concentric shells and ducts for future grouting of internal dissipators; (f) weld beads on the outer-shell internal surface; (g) roughened concrete surface.



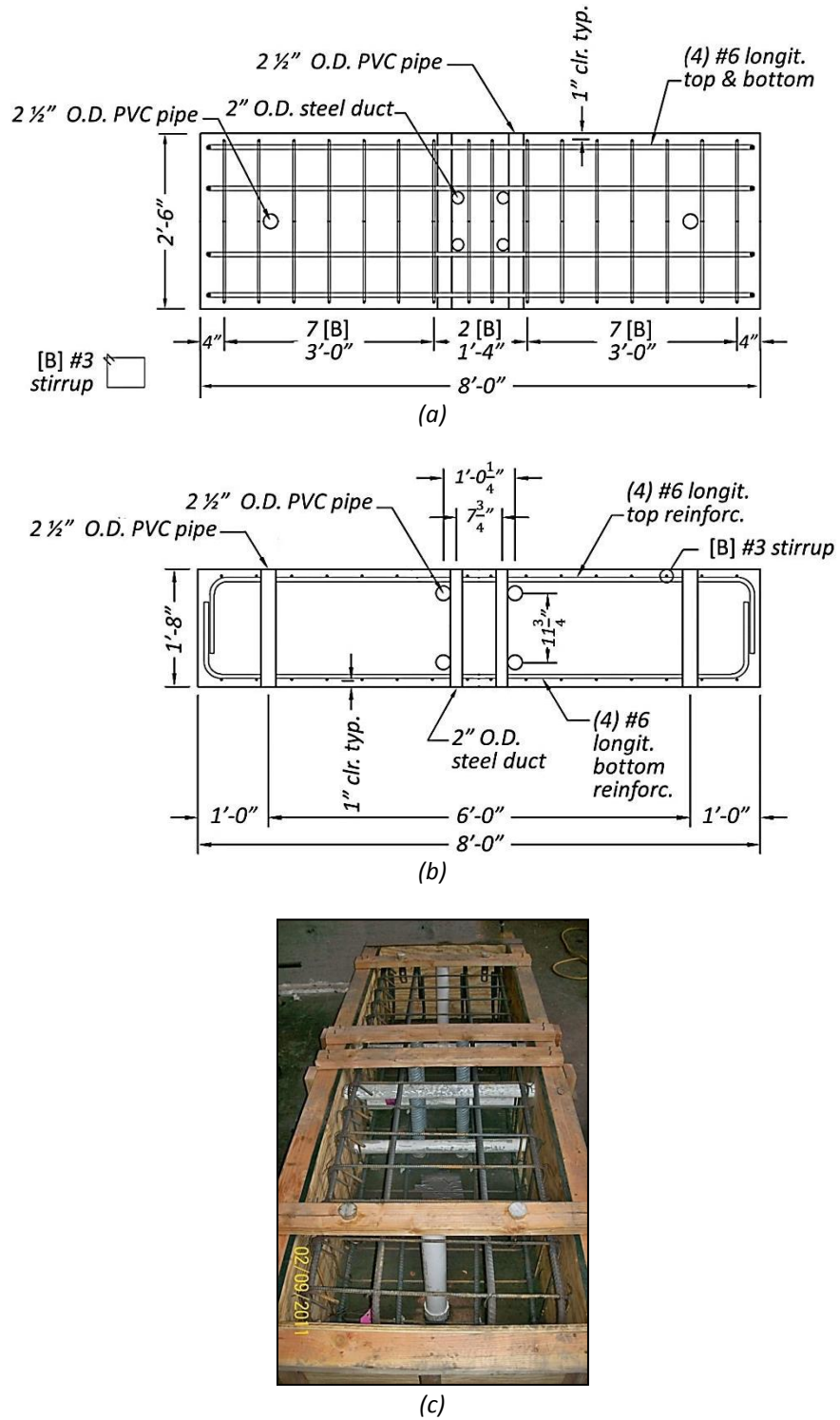


(c)



(d)

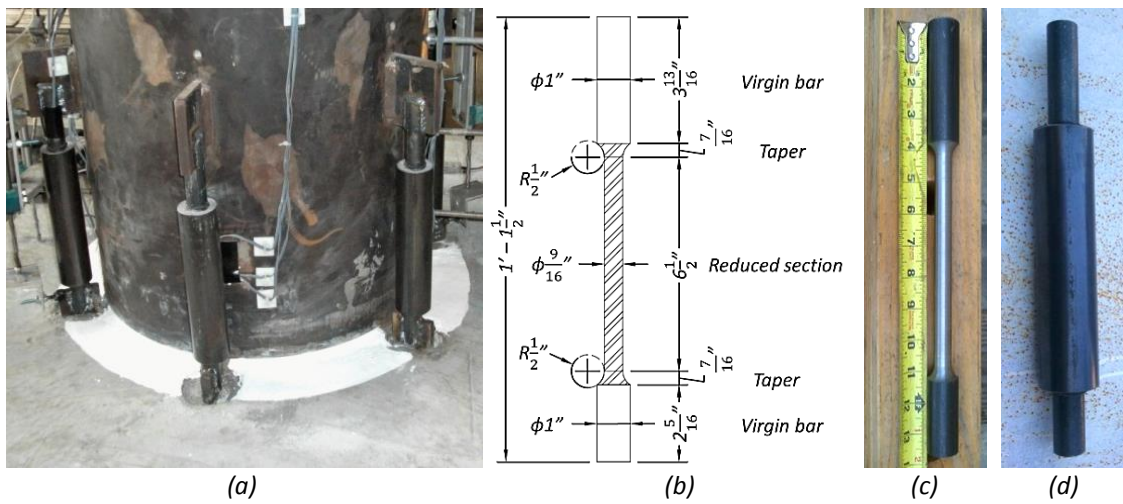
**Figure 3.3** – Footing details: (a) horizontal section; (b) longitudinal section; (c) reinforcement, ducts, and formwork; (d) steel ducts and spiral reinforcement.



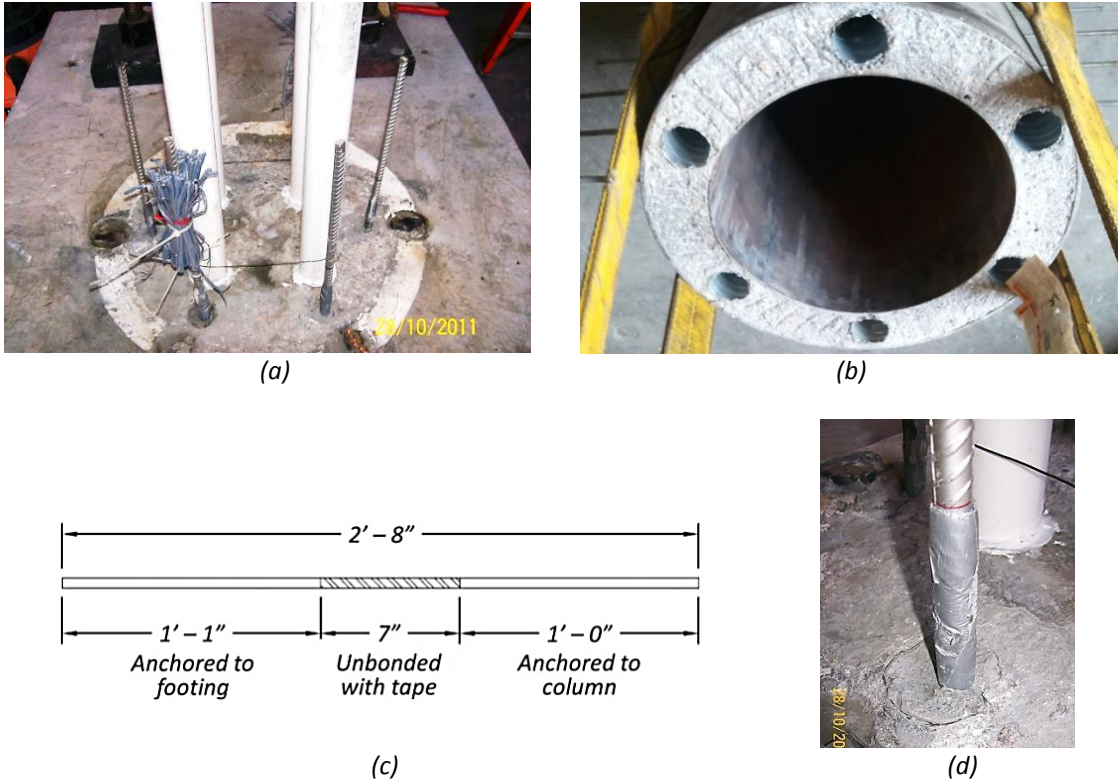
**Figure 3.4** – Load-stub details: (a) horizontal section; (b) longitudinal section; (c) reinforcement, ducts, and formwork.



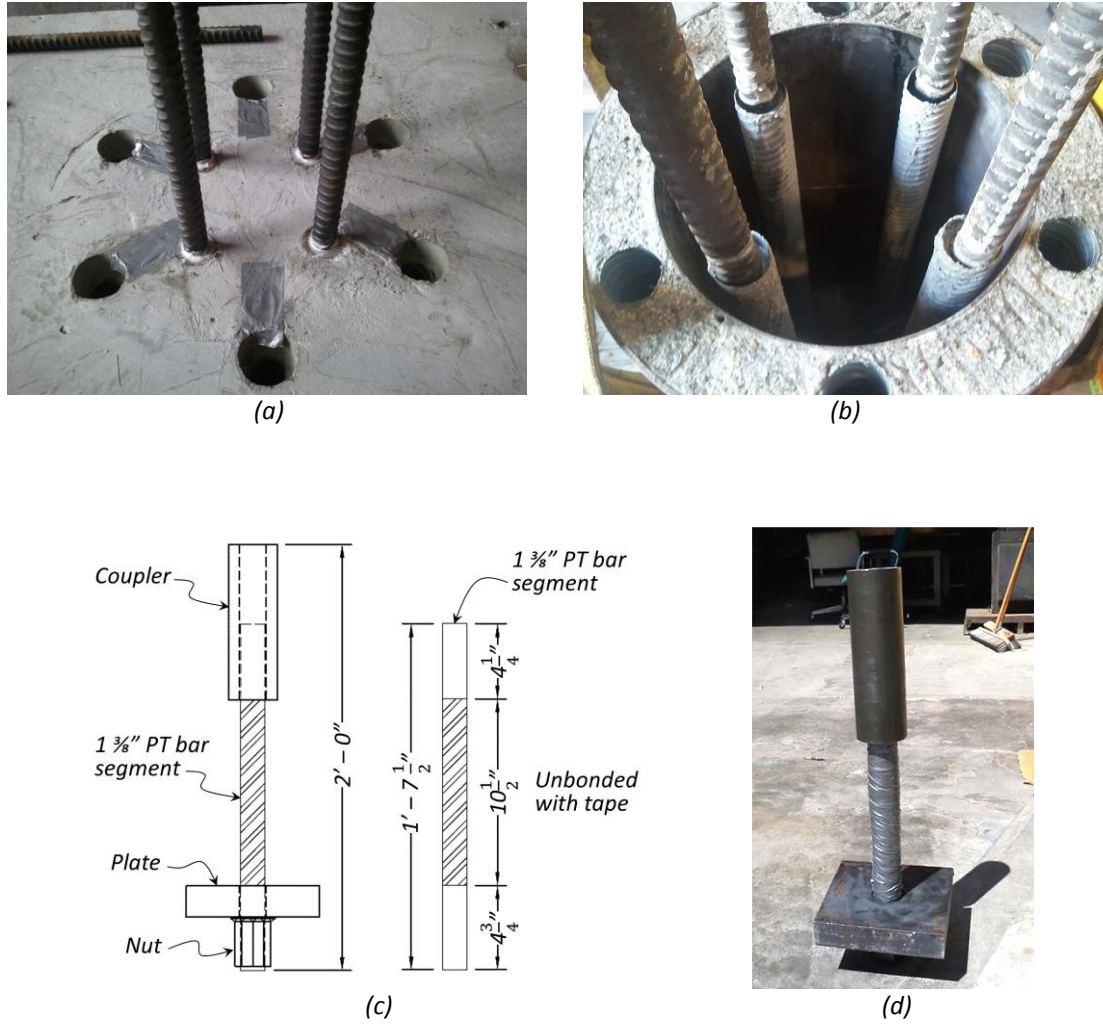
**Figure 3.5** – Mortar bed: (a) wood template and nylon-rod shims, during mortar placement; (b) mortar scraped from underneath the outer shell.



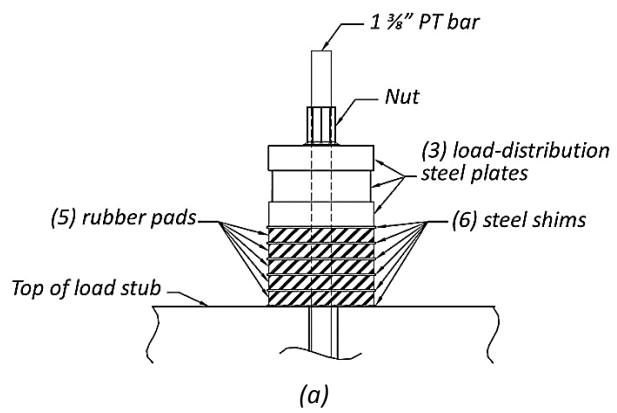
**Figure 3.6** – External energy dissipators: (a) location around column perimeter; (b) milled-bar dimensions; (c) dog-bone milled steel bar; (d) assembled buckling-restrained device.



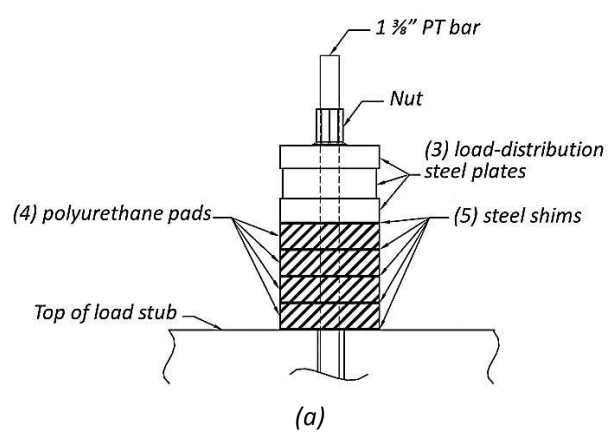
**Figure 3.7** – Internal energy dissipators: (a) dowels grouted in the footing; (b) ducts in the column; (c) dowel dimensions; (d) detail of bar wrapping across the interface.



**Figure 3.8** – Post-tensioning bars: (a) bars screwed into the footing anchorages; (b) sleeved bars inside the hollow core; (c) anchorage components and dimensions; (d) assembled anchorage device.



**Figure 3.9** – Rubber bearing of Unit 1A: (a) components; (b) single pad; (c) assembled bearings.



**Figure 3.10** – Polyurethane bearing of Unit 1B: (a) components; (b) single pad; (c) assembled bearings.

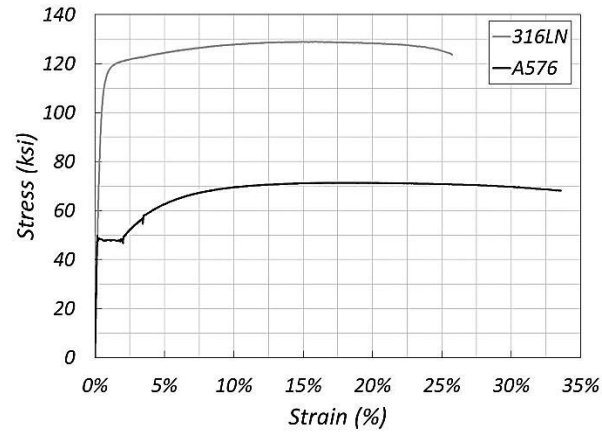


Figure 3.11 – Measured stress-strain relationships for the energy dissipator steel.

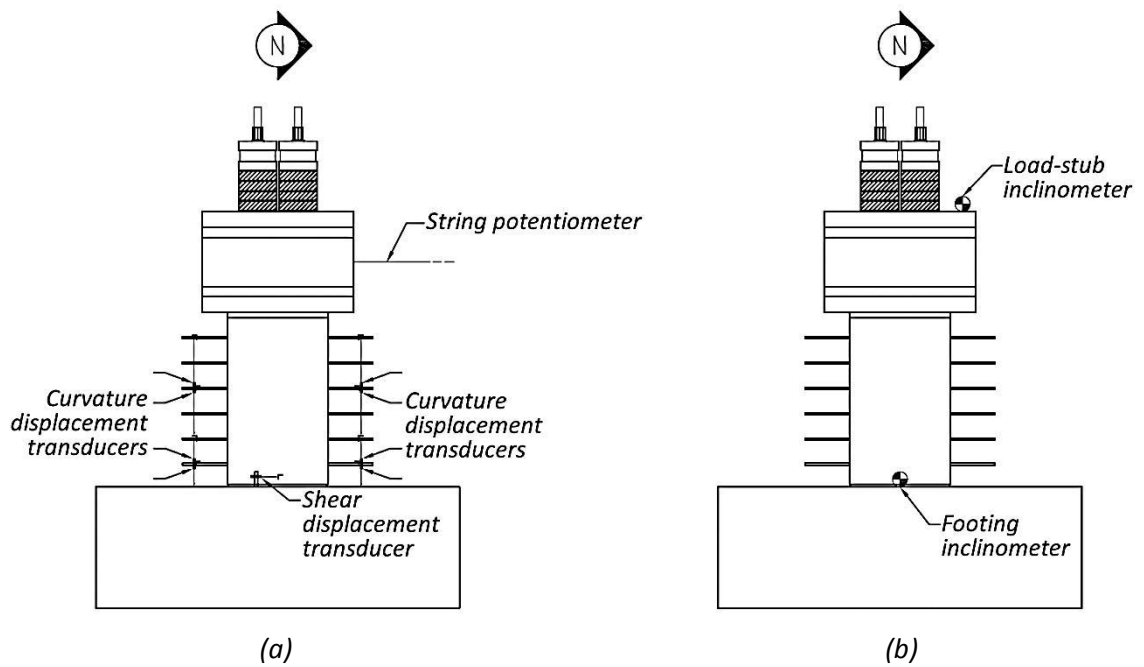


Figure 3.12 – (a) Displacement transducers and (b) inclinometers.

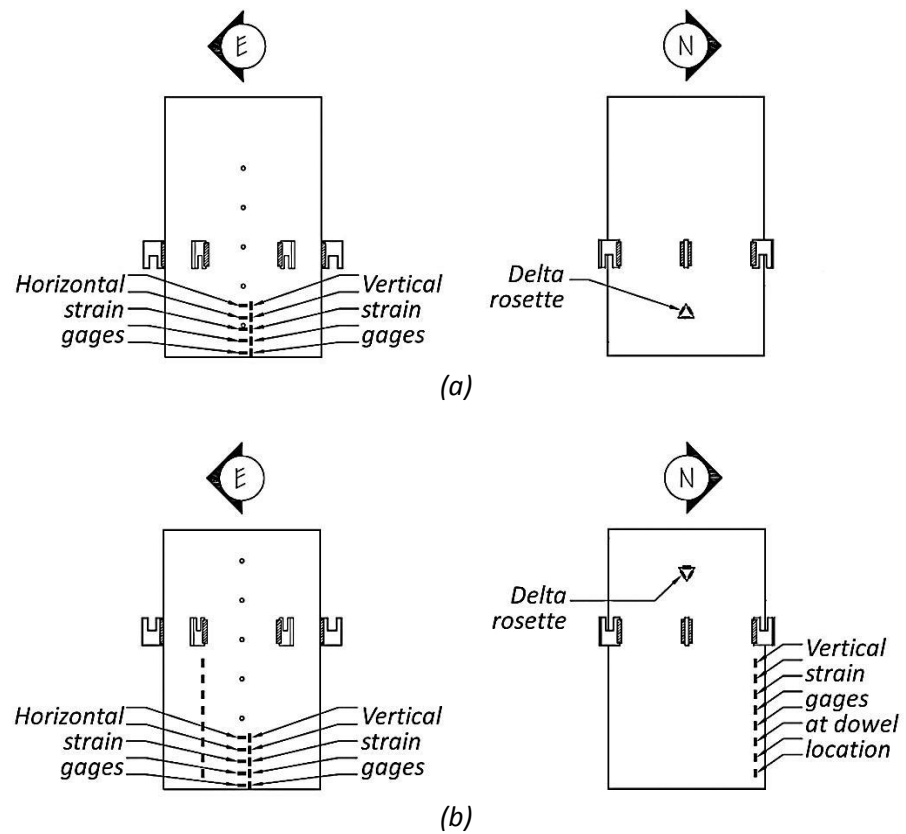


Figure 3.13 – Outer-shell strain gages: (a) Unit 1A; (b) Unit 1B.

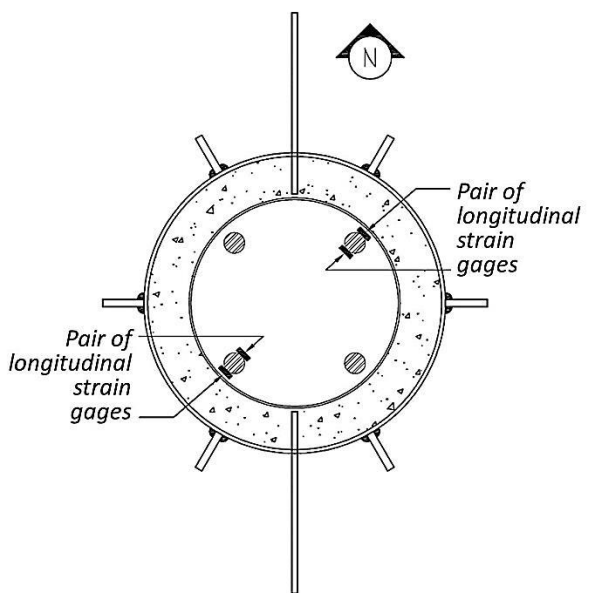
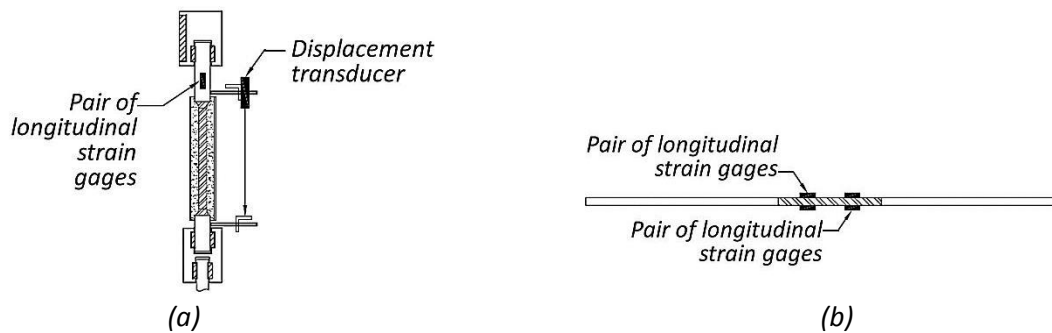
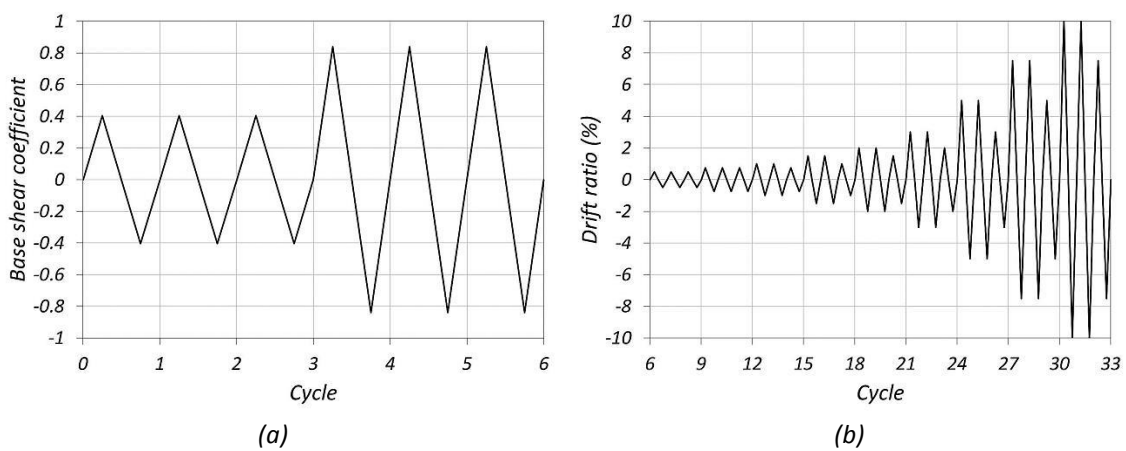


Figure 3.14 – Post-tensioning bars strain gages.

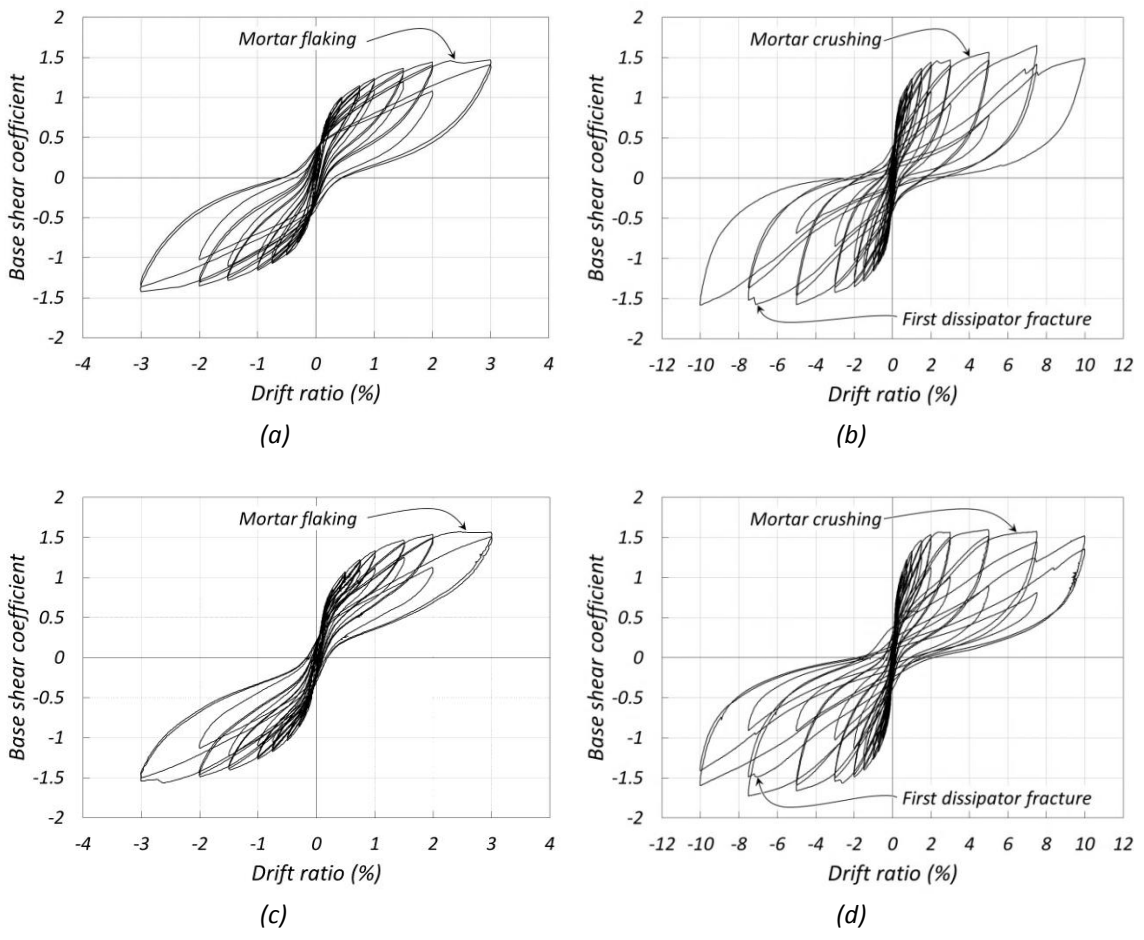




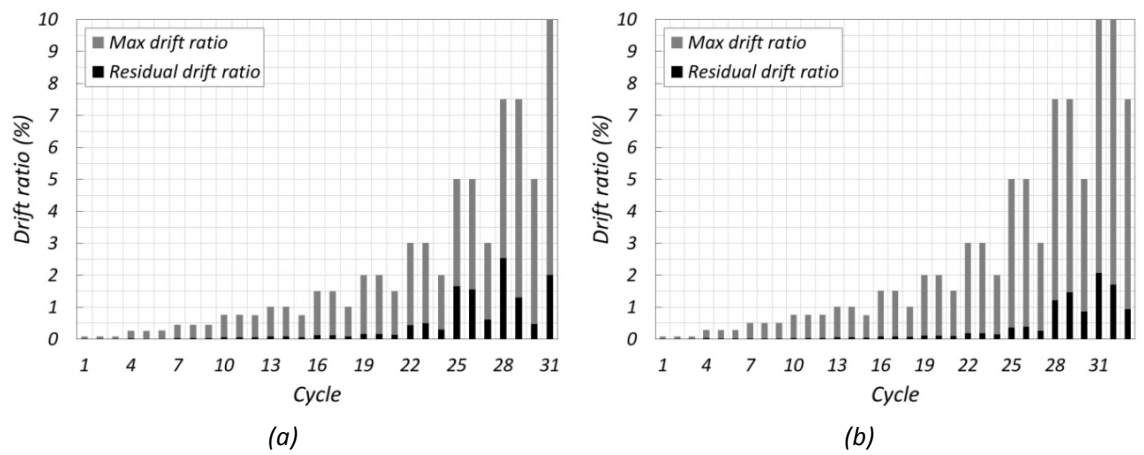
**Figure 3.15** – Energy dissipators instrumentation: (a) external buckling-restrained devices of Unit 1A; (b) internal dowels of Unit 1B.



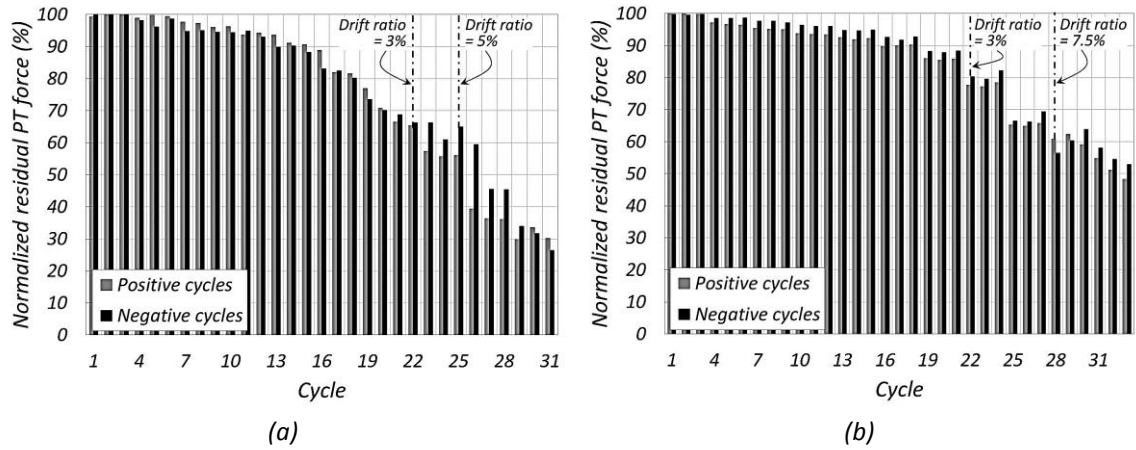
**Figure 3.16** – Hysteretic lateral force-displacement response: (a) Unit 1A; (b) Unit 1B.



**Figure 3.17** – Lateral force-displacement response: (a) Unit 1A up to 3% drift ratio; (b) Unit 1A up to 10% drift ratio; (c) Unit 1B up to 3% drift ratio; (d) Unit 1B up to 10% drift ratio.



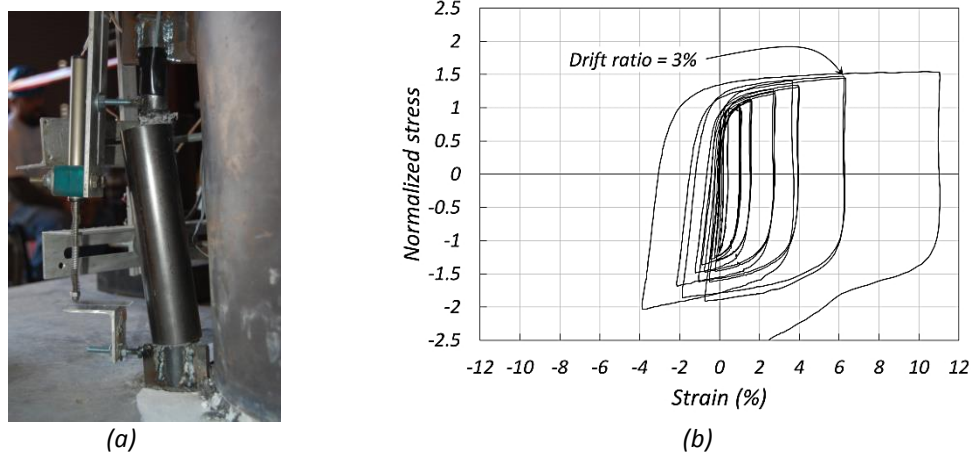
**Figure 3.18** – Maximum and residual drift ratios: (a) Unit 1A; (b) Unit 1B. Only cycles to positive displacements are reported.



**Figure 3.19** – Residual post-tensioning forces at the end of each cycle: (a) Unit 1A, north-east bar; (b) Unit 1B, south-west bar.



**Figure 3.20** – Crushed mortar bed at the end of testing: (a) Unit 1A; (b) Unit 1B.



**Figure 3.21** – Unit 1A: (a) distortion of external energy dissipators; (b) north-west energy dissipator hysteretic loops up to 5% drift ratio.



**Figure 3.22** – Permanent concrete and shell deformations at the end of testing: (a) Unit 1A; (b) Unit 1B.

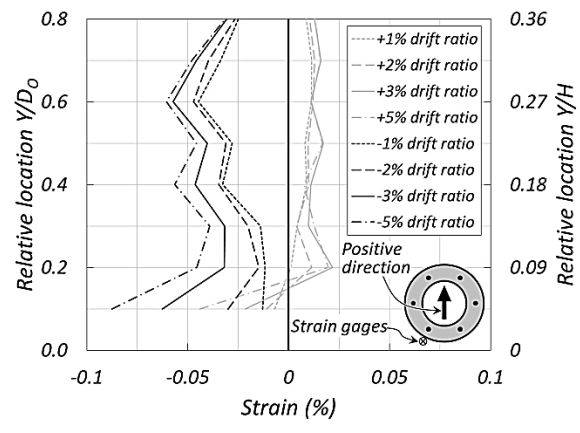


Figure 3.23 – Outer-shell longitudinal strain profiles in front of the south-west dowel for Unit 1B.

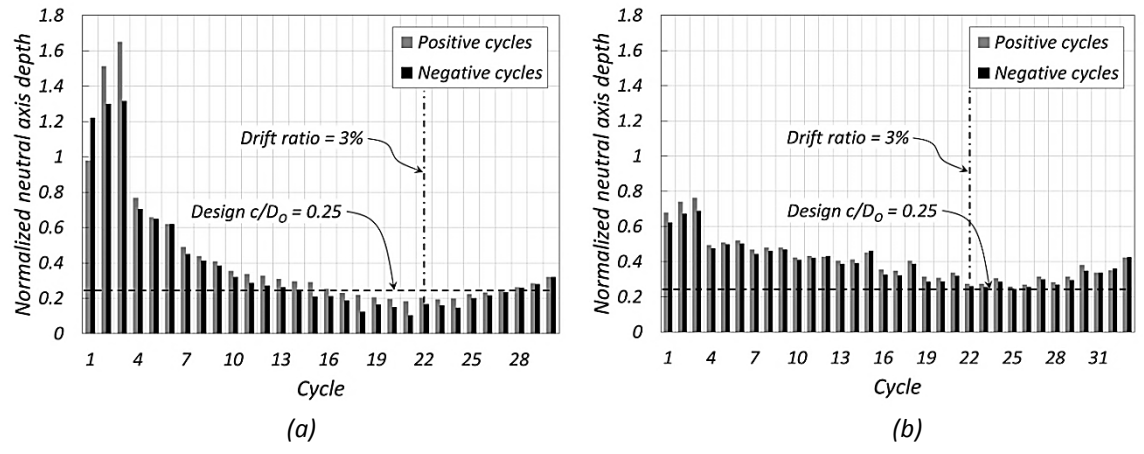


Figure 3.24 – Neutral axis depth at peak lateral displacements: (a) Unit 1A; (b) Unit 1B.

## Chapter 4

### NUMERICAL MODELING OF THE TEST UNITS

#### 4.1. NUMERICAL MODEL DESCRIPTION

A three-dimensional numerical model of the test units was built and validated with the experimental results. For this purpose the software OpenSees (Mazzoni et al., 2007; McKenna et al., 2010), developed by the Pacific Earthquake Engineering Research Center (PEER), was used.

A sketch illustrating the main model components is shown on Figure 4.1. The column was modeled with elastic frame elements, connected to the mortar bed at the base and to the point of application of the load at the top. Multiple non-linear truss elements represented the mortar at the column-footing joint; they were fixed at the base and connected to the bottom node of the column by rigid links. Post-tensioning bars were modeled as non-linear truss elements, with an initial stress equal to the effectively applied prestress; they were fixed at the base and connected to the top node of the column by rigid links. External energy dissipating devices were represented by non-linear frame elements, with the lower ends fixed to the footing, and the upper ends connected to a column intermediate node by rigid links. Since the deformations within the load stub are

negligible, the loading point was linked to the column top with a rigid link. All rigid links mentioned in this chapter were modeled as elastic elements with very high stiffness compared to the adjoining elements.

#### 4.1.1. Composite Column

The column was modeled with two elastic beam-column elements in series, connected to the mortar bed at the base and to the loading point at the top; the intermediate node was needed to connect the energy dissipator elements. The stiffness of the lower segment was based on the concrete hollow section only, as the outer shell does not transfer directly compression at the interface (contact with the mortar is avoided) and tension is resisted by the energy dissipators at that location. Instead, the transformed-section stiffness was assigned to the upper segment, where the outer steel is effective in composite action with the concrete.

The concrete elastic modulus was taken as  $E_c = 4,700 \times \sqrt{f'_c}$  (MPa) or  $E_c = 1800 \times \sqrt{f'_c}$  (ksi), where  $f'_c$  is the concrete compressive strength on the day of testing, while for the steel shell  $E_s = 200$  GPa (29000 ksi) was used. A node was defined just above the column, at a distance equal to half the load stub height, for the application of the vertical load and lateral displacement histories; since the deformations of the loading stub are expected to be negligible, this node was linked to the top of the column with a rigid element.

#### 4.1.2. Mortar Bed

Multiple non-linear truss elements (Taylor, 1977; Vulcano and Bertero, 1987; Carr, 2008) represented the mortar at the interface between column and footing; their length was set equal to the actual mortar thickness, i.e. 12.7 mm (0.5 in.).

“Concrete01” non-linear material model was applied to these elements; this concrete-specific rule includes no tensile strength, consistently with gap opening. Peak compressive stress and strain, and ultimate stress and strain need to be input. A parabola connects the origin to the peak point, and a straight line goes from the peak to the ultimate point; for strains larger than the ultimate one, stresses drop to zero. The initial tangent elastic modulus is automatically derived by fitting a parabola through the origin, being its vertex the peak point.

Peak stresses of 56 MPa (8.1 ksi, Unit 1A) and 59 MPa (8.5 ksi, Unit 1B), and peak strains of 0.4% (Units 1A and 1B) were obtained from Mander’s model for confined concrete (Mander et al., 1988), assuming a confinement efficiency coefficient equal to 0.1; such a low value is consistent with confinement being provided only by friction with column and footing surfaces, as discussed in Chapter 2. The ultimate strain was set to 15%, with a residual stress of 6.9 MPa (1 ksi).

Strains in the stress-strain relationship were amplified by the ratio of the theoretical neutral axis depth, taken equal to 127 mm (5 in.), to the actual thickness of the mortar bed. With this transformation, the spread of inelastic behavior within the column, assumed to extend uniformly for a length equal to the neutral axis depth (Restrepo and Rahman, 2007), was approximately taken into account.



#### 4.1.3. Post-Tensioning Bars

Post-tensioning bars were modeled as non-linear truss elements, fixed at the base and connected to the top node of the column by rigid elements. An equivalent initial tangent elastic modulus and an equivalent bilinear factor were calculated, to account for the stiffness of rubber or urethane bearings in series with the bars.

“Steel02” material hysteretic rule (Filippou et al., 1983), based on Giuffré-Menegotto-Pinto model, was assigned to these elements. Initial stresses of 207 MPa (30 ksi) for Unit 1A and 216 MPa (31 ksi) for Unit 1B were set to simulate the effective prestress after losses. The yield stress was set equal to 827 MPa (120 ksi). Curvature parameters  $R_0 = 18$ ,  $c_{R1} = 0.925$ , and  $c_{R2} = 0.15$  were chosen, while no isotropic hardening was introduced.

#### 4.1.4. Energy Dissipators

Energy dissipators were modeled as non-linear displacement-based beam-column elements. The lower ends were fixed to the footing, while the upper ends were connected to the column intermediate node by rigid links.

The element non-linear properties were assigned in terms of internal forces rather than using fiber discretization, which is computationally burdensome; thus axial, flexural, and torsional behaviors were assigned to these elements at the cross-section level. “Steel02” non-linear material model (Filippou et al., 1983) was assigned to the dissipator axial and flexural relationships, while the torsional response was considered elastic. Decoupling axial and flexural behavior was particularly justified for external buckling-restrained devices, where the yielding segment was mainly subjected to axial

deformations, while the non-milled ends were mainly interested by bending.

Three integration points were defined along each element, two at the ends and one in the middle; even though, the element is mainly subject to axial force, providing a minimum number of integration points would avoid numerical issues under bending.

#### ***4.1.4.1. Unit 1A: External Buckling-Restrained Devices***

External energy dissipating devices for test Unit 1A were represented by three beam-column elements in series, to include the section variation between non-yielding ends and milled segment.

The material parameters were selected to match the experimental hysteretic behavior of the device and considering the different behavior shown by the dissipators in tension and compression, due to partial composite action with the grout. A fictitious yield stress equal to 469 MPa (68 ksi) and peak strain equal to 0.06 were assigned for this scope, in combination with curvature parameters  $R_0 = 18$ ,  $c_{R1} = 0.925$ , and  $c_{R2} = 0.15$ , and isotropic-hardening parameters  $a_1 = 0.07$ ,  $a_2 = 3$ ,  $a_3 = 0$ , and  $a_4 = 1$ .

#### ***4.1.4.2. Unit 1B: Internal Dowels***

Internal dowel bars for Unit 1B were instead modeled with single beam-column elements, with length equal to the yielding debonded segment.

In this case the material parameters were calibrated with the results of a cyclic test conducted on a stainless-steel reinforcing bar with a length-to-diameter aspect ratio of 3. A fictitious yield stress equal to 827 MPa (120 ksi) was assigned for this scope, in combination with curvature parameters  $R_0 = 18$ ,  $c_{R1} = 0.925$ , and  $c_{R2} = 0.15$ , and isotropic-

hardening parameters  $a_1 = 0$ ,  $a_2 = 1$ ,  $a_3 = 0$ , and  $a_4 = 1$ .

#### **4.1.5. Analysis Procedure**

The analysis was performed in two stages: first, the vertical load was applied and held constant; then the cyclic quasi-static lateral displacement history was assigned to the load stub centroid. The Newton-Raphson algorithm was chosen to solve the nonlinear residual equation.

The analysis was performed under the hypothesis of small displacements, or linear geometric transformation in OpenSees language. This choice was justified by the vertical load being applied through tie-down rods, which were rotating together with the column under lateral displacement; as a consequence, the applied gravity-equivalent force was always acting along the column axis with no significant interaction between axial load and lateral displacement.

The numerical analysis was run up to 5% drift ratio. Modeling the near-failure material behavior requires the implementation of more elaborated routines and the knowledge of a number of parameters that were not available from these experimental tests. Moreover, larger drift ratios would be extremely demanding for other components of a bridge, such as superstructure or abutments, and typically the design would target drift ratios within this range. Thus, care was paid at accurately capturing the response up to this extent.

## **4.2. NUMERICAL ANALYSIS RESULTS**

### **4.2.1. Global Hysteretic Response**

Figure 4.2 shows a comparison between experimental and numerical force-displacement relationships up to 1% and 5% drift ratios. The model captures accurately strength, stiffness, and self-centering characteristics of the system, as well as progressive stiffness degradation and loss of self-centering capacity. In the case of Unit 1A the numerical model slightly overestimates the stiffness of the system, predicting higher lateral forces in particular after 2% drift ratio cycles (Fig. 4.2(b)). In the case of Unit 1B, instead, the model underestimates the stiffness for drift ratios between 1% and 3% (Fig. 4.2(d)).

### **4.2.2. Global Energy Dissipation**

Figure 4.3 confirms the good agreement between numerical and experimental response, in terms of cumulative energy dissipated. In these plots, the energy has been normalized by the product of the maximum lateral displacement times the maximum lateral force measured during the test.

### **4.2.3. Post-Tensioning Bar Strain History**

Figure 4.4 shows a comparison between numerical and experimental strain histories of the north-east post-tensioning bar of Unit 1A and of the south-west post-tensioning bar of Unit 1B, up to 5% drift ratio. Generally good agreement with the experimental results is observed; a slight overestimation of the peak tensile strains is evident at higher drift ratios.

The different amount of prestress loss measured for the two test units at 5% drift ratio, due to more extensive crushing of the mortar bed in Unit 1A, is well captured by the model, contributing to a good prediction of the overall behavior of the system.

#### **4.2.4. Energy Dissipators Hysteretic Response**

The numerical hysteretic axial strain-stress response of the north-west external dissipator of Unit 1A is compared to the experimental one on Figure 4.5. A lower degree of accuracy was observed in the predicted hysteretic response of the energy dissipators, compared to the global system response. Overestimation of the dissipator strength, both in tension and compression, is visible at low strains. Some numerical issues were experienced with the material model, especially at low deformations, where unexpected jumps can be observed on the plots. However, the higher compressive strength compared to the tensile one, due to partial composite action with grout in the buckling-restrained segment, was correctly reproduced with the selected isotropic hardening parameters.

It should be noted that also the experimental measurement of the response of these devices was affected by two sources of inaccuracy, as discussed in Chapter 3. First, the dissipator axial force was calculated from the axial strains measured by strain gages applied to the elastic non-milled end segments; however, these segments were subjected to bending during the test, which may have affected the determination of the axial force. Second, the average axial strain of the yielding segment was calculated from the relative displacement between two sections right outside the casing; bending of the end segments caused relative rotations between these two sections, which in turn affected the measurement of the relative displacement.

For these reason, considering the overall satisfactory prediction of the test units behavior, the energy dissipator model was considered acceptable.

### **4.3. SIMPLIFIED ANALYSIS**

For design purposes, a simplified section analysis can be carried out to determine the joint moment-rotation relationship, as outlined in Chapter 2. Five points were considered to build the monotonic moment-rotation and pushover relationships for Units 1A and 1B:

- decompression at the base section
- first-yielding of the extreme energy dissipator in tension
- compressive strain of 0.003 on the extreme mortar fiber
- base joint rotation of 0.02 rad
- base joint rotation of 0.04 rad
- fracture of the most tensile dissipator, associated to reaching  $2/3$  of the peak strain.

The measured steel mechanical properties (yield point, peak point, and elastic modulus) were assigned to the dissipators, and the mortar bed properties were derived from the experimental compressive strength and Mander's model (Mander et al., 1988). The stiffness of the elastomeric bearings conformed to the one presented in Chapter 3. Nominal properties were used for the post-tensioning bars and outer shell steel.

The pushover envelopes obtained from this simplified approach are in good agreement with the recorded experimental responses (Fig. 4.6), underestimating the real strength by less than 15%. However, the neutral axis depth predicted by this simplified

approach was not always well matching the measured one (Fig. 4.7). This may be partially due to the approximation in the stress-strain relationships, and especially to the lack of consideration for damage accumulation in the monotonic constitutive laws.

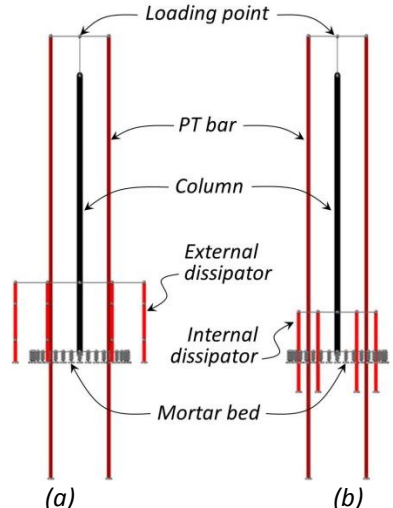


Figure 4.1 – Sketches of the test specimen numerical models: (a) Unit 1A; (b) Unit 1B.

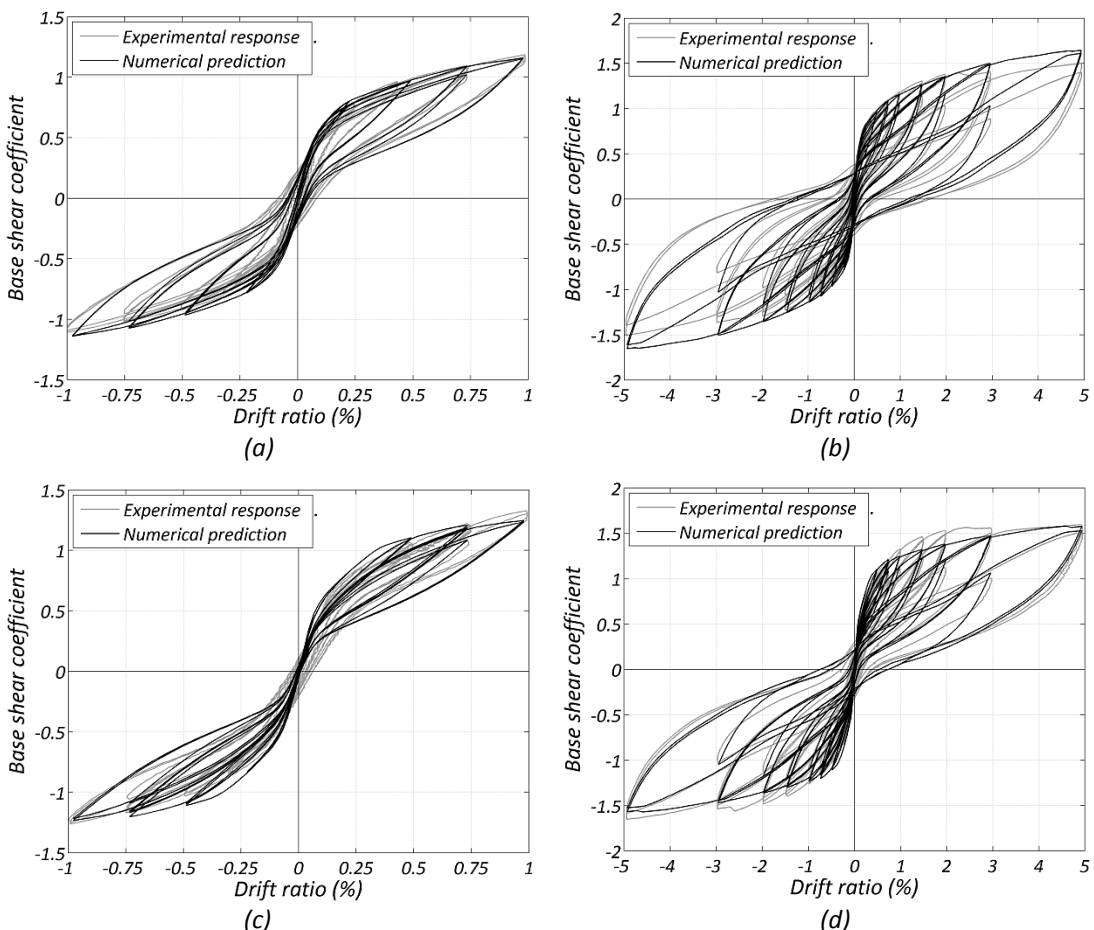


Figure 4.2 – Numerical and experimental lateral force-displacement response: (a) Unit 1A up to 1% drift ratio; (b) Unit 1A up to 5% drift ratio; (c) Unit 1B up to 1% drift ratio; (d) Unit 1B up to 5% drift ratio.



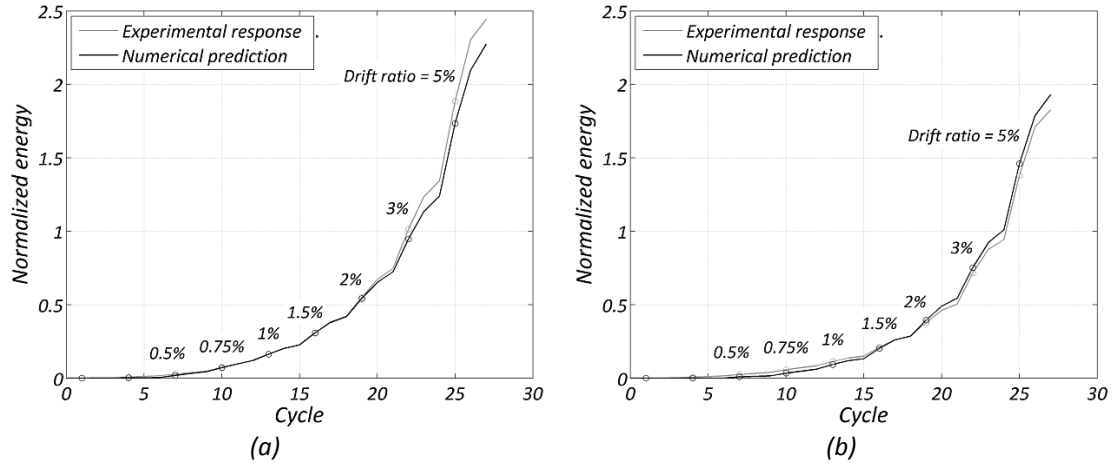


Figure 4.3 – Numerical and experimental cumulative hysteretic energy: (a) Unit 1A; (b) Unit 1B.

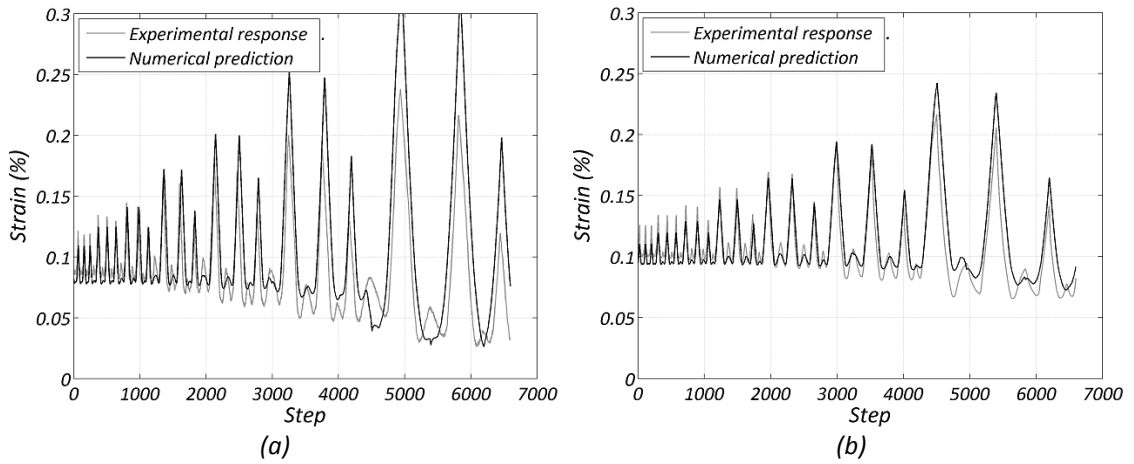
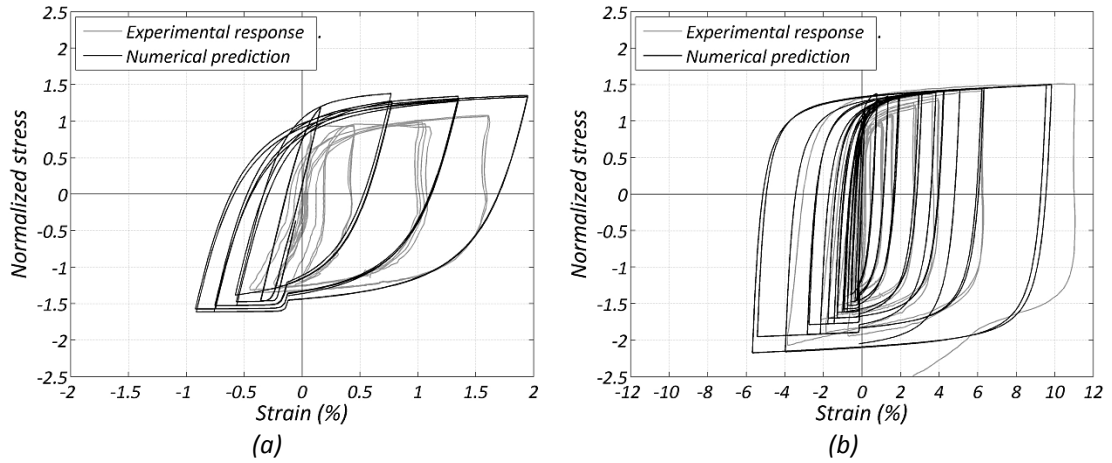
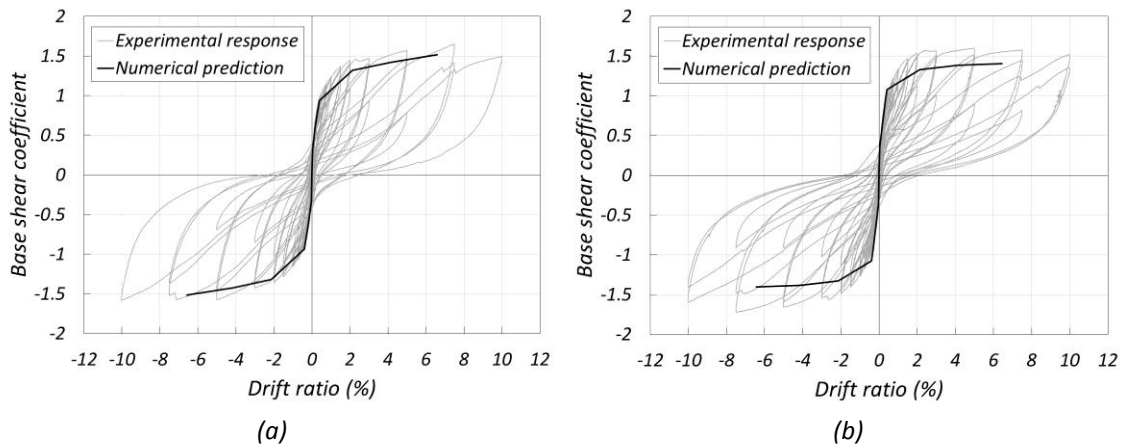


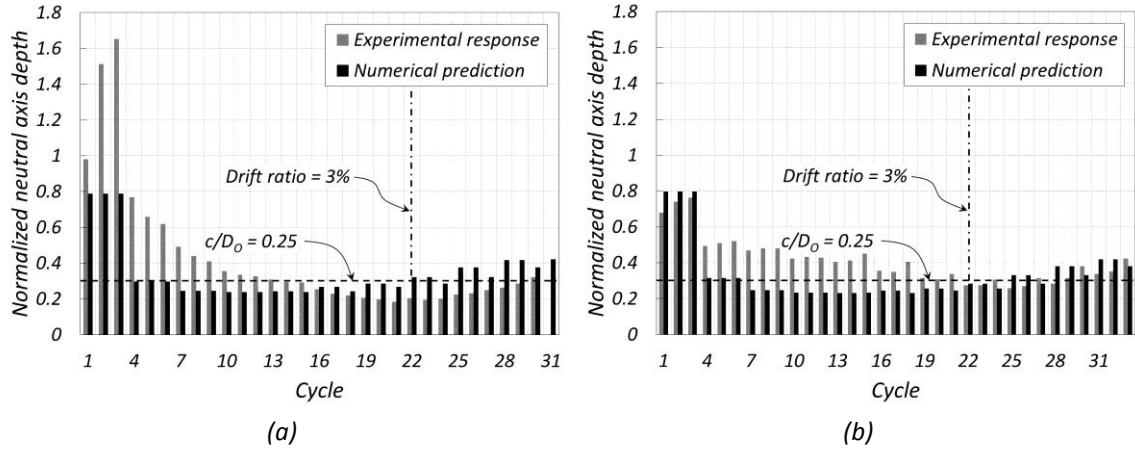
Figure 4.4 – Numerical and experimental post-tensioning bar strain history: (a) Unit 1A, north-east bar; (b) Unit 1B, south-west bar.



**Figure 4.5** – Numerical and experimental hysteretic response of the north-west energy dissipator in Unit 1A: (a) cycles up to 1% drift ratio; (b) cycles up to 5% drift ratio.



**Figure 4.6** – Simplified numerical prediction of the pushover envelope: (a) Unit 1A; (b) Unit 1B.



**Figure 4.7** – Simplified numerical and experimental neutral-axis depth: (a) Unit 1A; (b) Unit 1B. Only positive cycles are shown.

## **Chapter 5**

### **CONCLUSIONS**

This dissertation discussed the design criteria, experimental performance and numerical modeling of composite concrete-dual steel shell bridge column technology. This type of column can be specifically designed to minimize damage at the design earthquake, and to exhibit rocking/self-centering response even after large inelastic displacements. Only minor incipient damage is experienced under the same earthquake demands that would cause extensive damage on conventional columns. Damage is maintained at a minimum level even under demands 50% larger than the design one. This results in a dramatic reduction of repair cost and downtime.

The proposed technology also simplifies and accelerates bridge construction. The use of an external shell makes the conventional reinforcing cage obsolete, whereas the inner shell allows for removing unnecessary concrete volume and weight, making this technology ideal for prefabrication and quick erection.

Attention has been focused on details which make this technology effective and prevent undesired loss of self-centering ability. The mortar bed at the base of the column, required for accommodating construction tolerances between precast elements, needs to

be strong and tough enough to sustain the large compressive strain demands arising upon rocking. Post-tensioning bars need to be protected against premature yielding, especially in short-aspect-ratio columns.

Two units were built and tested with a quasi-static reversed cyclic protocol. The main variables between the two units were: (i) the type of energy-dissipation devices, which were either external buckling-restrained braces, or internal stainless steel dowels grouted into the concrete; (ii) the mortar bed, which was either a plain high-performance metallic-aggregate mix, or a fiber-modified high-performance metallic-aggregate mix ; and (iii) the type of elastomeric bearing placed in series with the post-tensioning bars, either rubber or polyurethane.

The units were designed to display no damage at 3% drift ratio, which was assumed to be the drift ratio corresponding to the design earthquake. Unit 1A, which had a plain metallic-aggregate mortar bed, exhibited mortar crushing and compromised self-centering ability during cycles to 5% drift ratio. In Unit 1B the metallic-aggregate mortar bed incorporated also polypropylene fibers; these fibers improved the mortar toughness and delayed its crushing, allowing this unit to display excellent performance beyond 5% drift ratio. In both units fracture of the energy dissipation devices occurred at drift ratios of 7.5%.

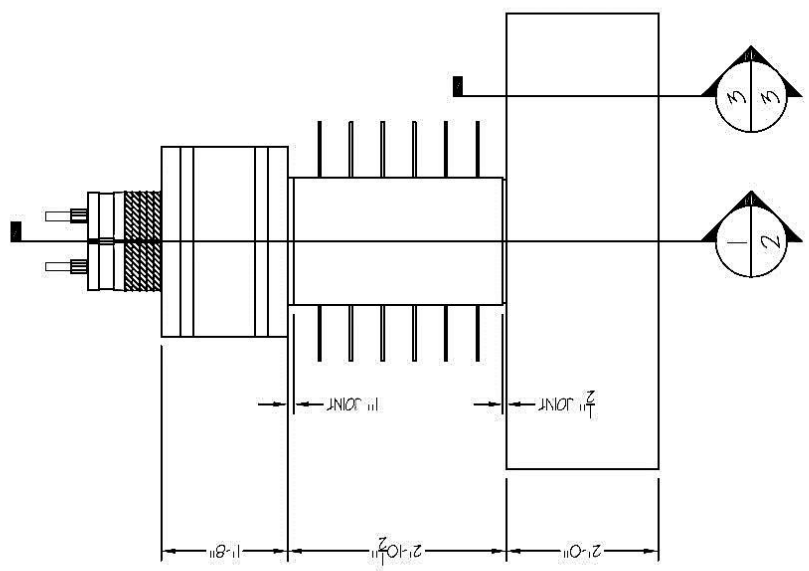
The tests were simulated in OpenSees environment up to a drift ratio of 5%. An accurate representation of the behavior of the two units was obtained in terms of both global response (lateral force-displacement relationship, cumulative hysteretic energy) and local response (post-tensioning bars strain history, energy dissipators stress-strain relationship).

The simplified pushover analysis, proposed for use in the design process, also reproduced satisfactorily the backbone curve of the lateral force-displacement response.

## **Appendix**

### **CONSTRUCTION DRAWINGS**

The construction drawings for Unit 1A and Unit 1B, inclusive of structural details and instrumentation plans, are shown on the next pages. Due to formatting constraints, the drawings are not to scale.



**GENERAL NOTES:**  
 1. THE CLEAR COVER FOR ALL SECTIONS SHALL BE 1" UNLESS OTHERWISE NOTED

**CONCRETE MATERIAL NOTES:**  
 1. ALL CONCRETE SHALL HAVE 28 DAY COMPRESSIVE STRENGTH OF 9,000 PSI  
 2. ALL CONCRETE SHALL HAVE MINIMUM SLUMP OF 8"

**GROUT AND MORTAR MATERIAL NOTES:**  
 1. DRY MIX PROPORTIONS SHALL BE USED  
 2. DURABLE POLYPROPYLENE FIBERS SHALL BE ADDED TO THE MORTAR AT THE COLUMN-FOOTING INTERFACE, WITH FIBER-TO-MORTAR WEIGHT RATIO OF 0.057%

**MILD REINFORCEMENT MATERIAL NOTES:**  
 1. MILD REINFORCEMENT INSIDE FOOTING AND LONG-SIDED SHALL BE A615, GRADE 60 STEEL

**POST-TENSIONING MATERIAL NOTES:**  
 1. ALL POST-TENSIONING SHALL BE AT72, GRADE 150, LOW RELAXATION STEEL  
 2. POST-TENSIONING FORCE AFTER LOSSES SHALL BE 59 KIPS (25% GD) PER POST-TENSIONING BAR

**STEEL SHELL MATERIAL NOTES:**  
 1. OUTER STEEL SHELL SHALL BE A572, GRADE 50

**ENERGY DISSIPATOR MATERIAL NOTES:**  
 1. EXTERNAL BULKING-RESTRAINED ENERGY DISSIPATORS SHALL BE A576, GRADE 1018, HOT ROLLED STEEL ANCHOR BARS FOR EXTERNAL DISSIPATORS SHALL BE AT06, GRADE 60 REINFORCING BARS  
 2. INTERNAL ENERGY DISSIPATORS SHALL BE 316LN, GRADE 60 STAINLESS STEEL REBARS

1 SPECIMEN ELEVATION  
 1/2" = 1'-0"

**APPROVED FOR PRODUCTION**

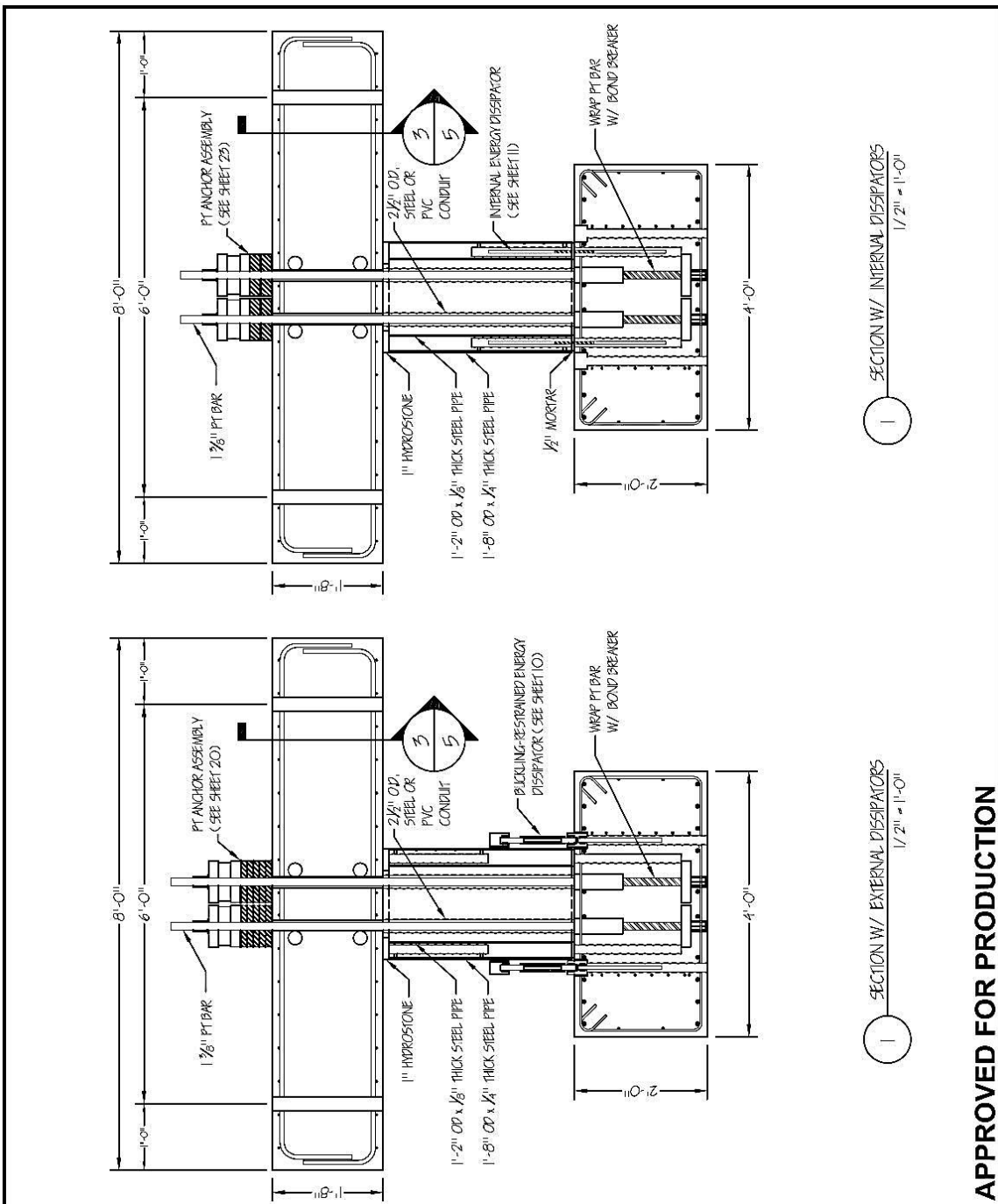


**ADV. PRECAST CONCR. DUAL-SHELL STEEL COLUMNS**

**SPECIMEN ELEVATION**

SPECIMEN:	UNIF: 1	REF:	QUASI STATIC - UCSD	CONNECTION DETAIL:	HYBRID DUAL-SHELL COLUMN			
BY:	CG	CHK:	DATE:	11/08/11	SCALE:	1/2" = 1'-0"	SHEET:	01





SECTION W/ INTERNAL DISSIPATORS  
1/2" = 1'-0"

SECTION W/ EXTERNAL DISSIPATORS  
1/2" = 1'-0"

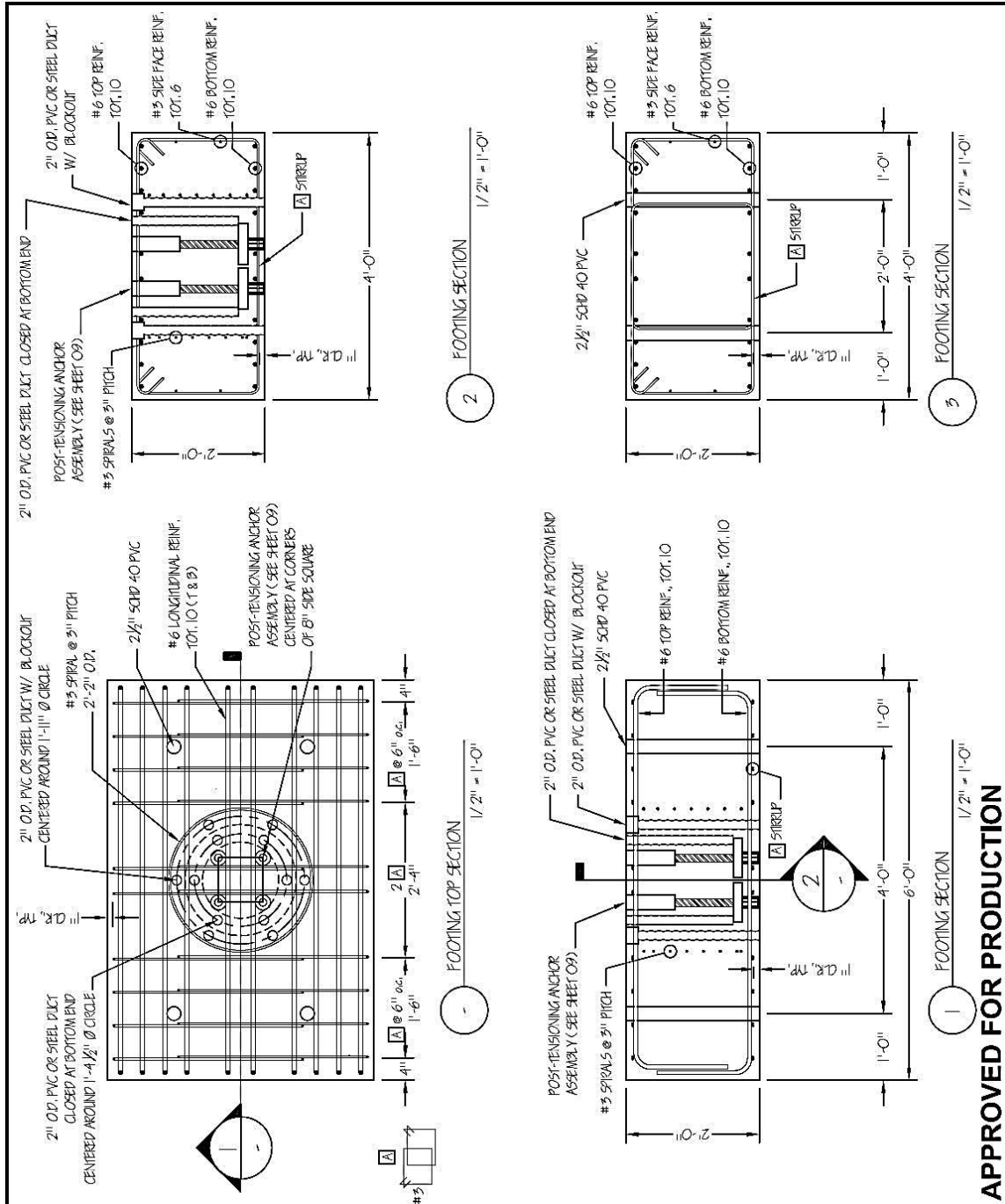
**APPROVED FOR PRODUCTION**



**ADV. PRECAST CONCR. DUAL-SHELL STEEL COLUMNS**

**GENERAL SECTION**

SPECIMEN:	UNIT:	TEST:	CONNECTION DETAIL:
	CG	QUASI STATIC - UCS2	HYBRID DUAL-SHELL COLUMN
BY:	CG	CHK:	DATE:
			11/08/11
		SCALE:	SHEET:
		1/2" = 1'-0"	02

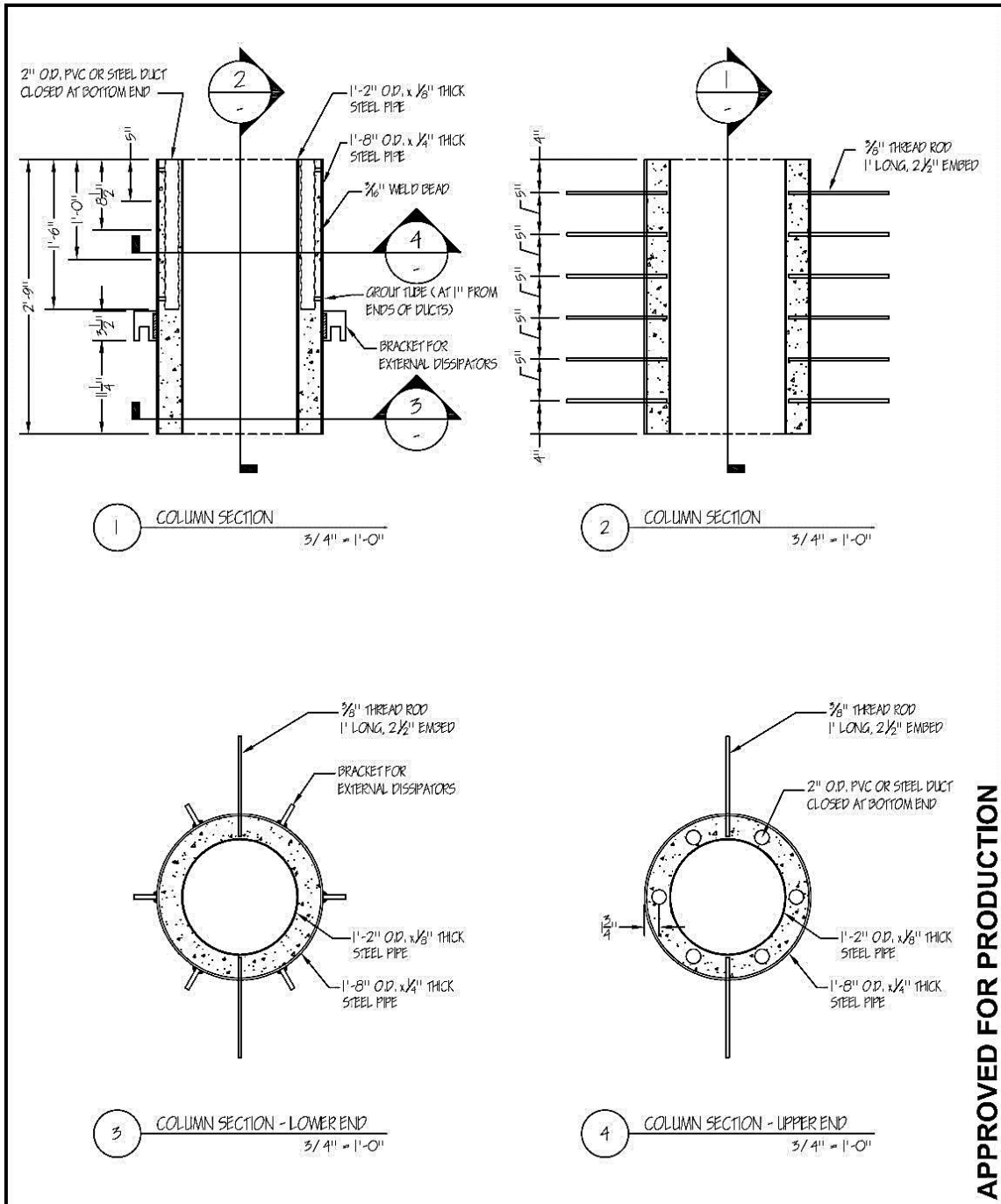


**APPROVED FOR PRODUCTION**



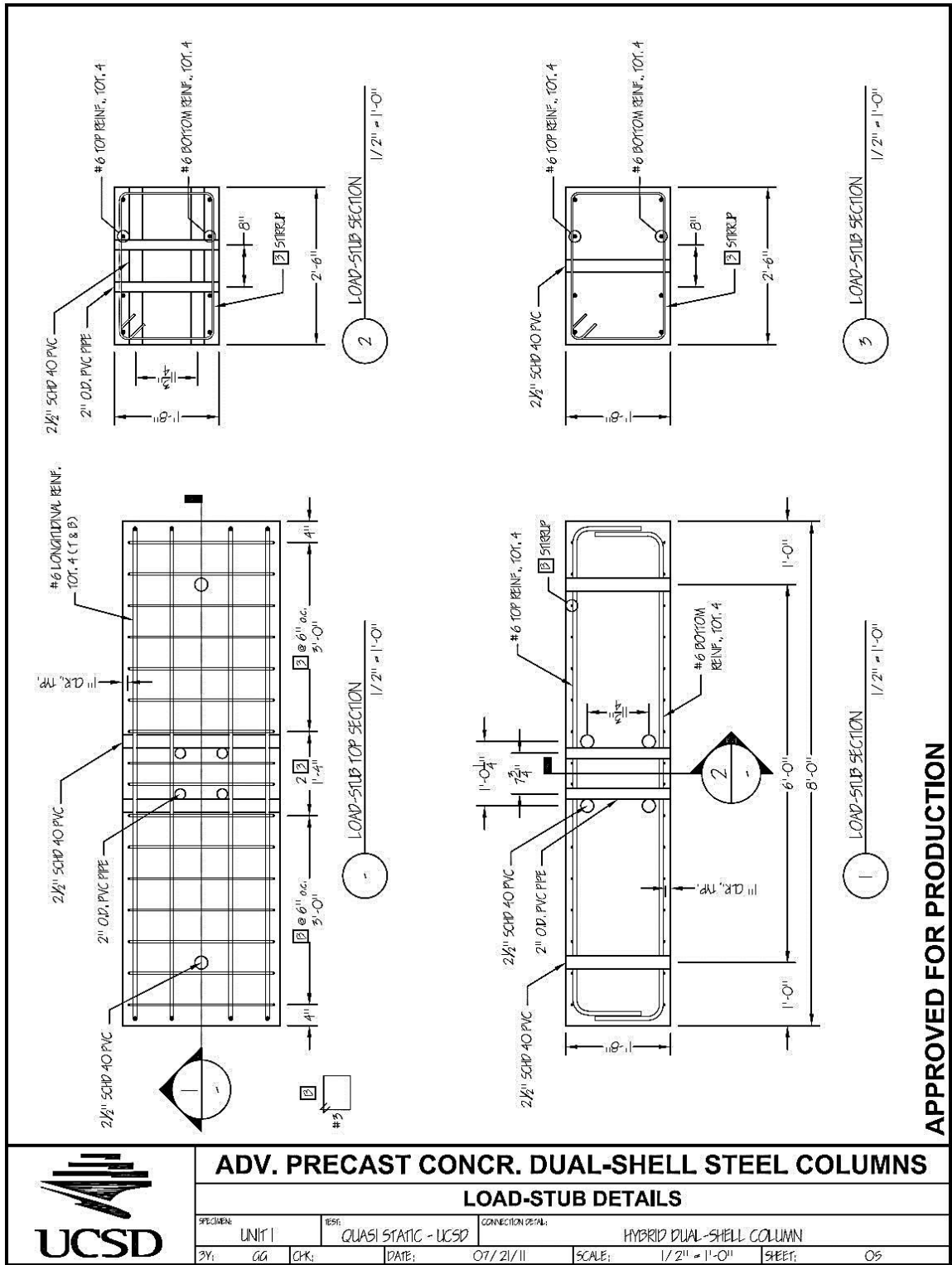
**ADV. PRECAST CONCR. DUAL-SHELL STEEL COLUMNS**  
**FOOTING DETAILS**

SPECIMEN:	UNIF 1	RES:	QUASI-STATIC - UCSD	CONNECTION DETAIL:	HYBRID DUAL-SHELL COLUMN
BY:	GG	CHK:		DATE:	10/25/11
				SCALE:	1/2" = 1'-0"
				SHEET:	03



APPROVED FOR PRODUCTION

	<b>ADV. PRECAST CONCR. DUAL-SHELL STEEL COLUMNS</b>					
	<b>COLUMN SECTIONS</b>					
	SPECIMEN:	UNIT:	ISSUE:	CONNECTION DETAIL:		
	3Y1	CG	CHK:	DATE:	SCALE:	SHEET:
			10/10/11	3/4" = 1'-0"	04	

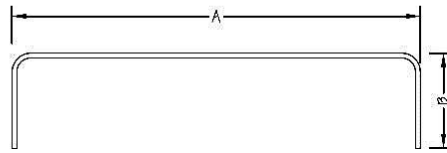


**APPROVED FOR PRODUCTION**

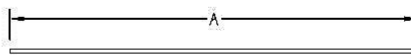


**ADV. PRECAST CONCR. DUAL-SHELL STEEL COLUMNS**  
**LOAD-STUB DETAILS**

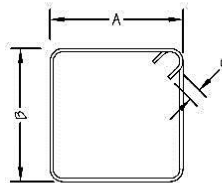
SPECIMEN:	UNIF: 1	REF:	QUASI STATIC - UCSD	CONNECTION DETAIL:	HYBRID DUAL-SHELL COLUMN
BY:	CG	CHK:	DATE:	07/21/11	SCALE:
					1/2" = 1'-0"
					SHEET:
					05



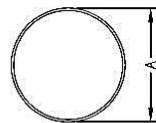
ASTM	GRADE	BAR SIZE	A	B	C	QTY
A615	60	#6	5'-9"	1'-5"	-	20
A615	60	#6	7'-9"	1'-1"	-	8



ASTM	GRADE	BAR SIZE	A	B	C	QTY
A615	60	#3	5'-10"	-	-	4
A706	60	#6	1'-5"	-	-	6



ASTM	GRADE	BAR SIZE	A	B	C	QTY
A615	60	#3	2'-10"	1'-10"	2 1/4"	20
A615	60	#3	2'-4"	1'-6"	2 1/4"	16



\*\*\* SPIRAL REINFORCEMENT \*\*\*

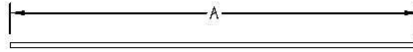
ASTM	GRADE	BAR SIZE	A	TURNS	PITCH	QTY
A615	60	#3	2'-2"	7	3"	1

APPROVED FOR PRODUCTION



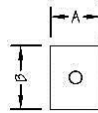
**ADV. PRECAST CONCR. DUAL-SHELL STEEL COLUMNS  
REINFORCEMENT SCHEDULE**

SPECIMEN:	UNIT:	REF:	CONNECTION DETAIL:
	CG	QUASI STATIC - UCSD	HYBRID DUAL-SHELL COLUMN
BY:	CG	CHK:	DATE:
			07/21/11
SCALE:	N15	SHEET:	06



\*\*\* DSI THREADBAR \*\*\*

ASIM	GRADE	BAR SIZE	A	B	C	QTY
A722	150	1 3/8"	9'-5"	-	-	8
A722	150	1 3/8"	1'-7 1/2"	-	-	4



\*\*\* DSI ANCHOR PLATE \*\*\*

BAR SIZE	A	B	THICKNESS	QTY
1 3/8"	7"	7 1/2"	1 3/4"	4

\*\*\* DSI COUPLER \*\*\*

BAR SIZE	LENGTH	DIAMETER	QTY
1 3/8"	8 3/4"	2 3/4"	4

\*\*\* DSI NUT \*\*\*

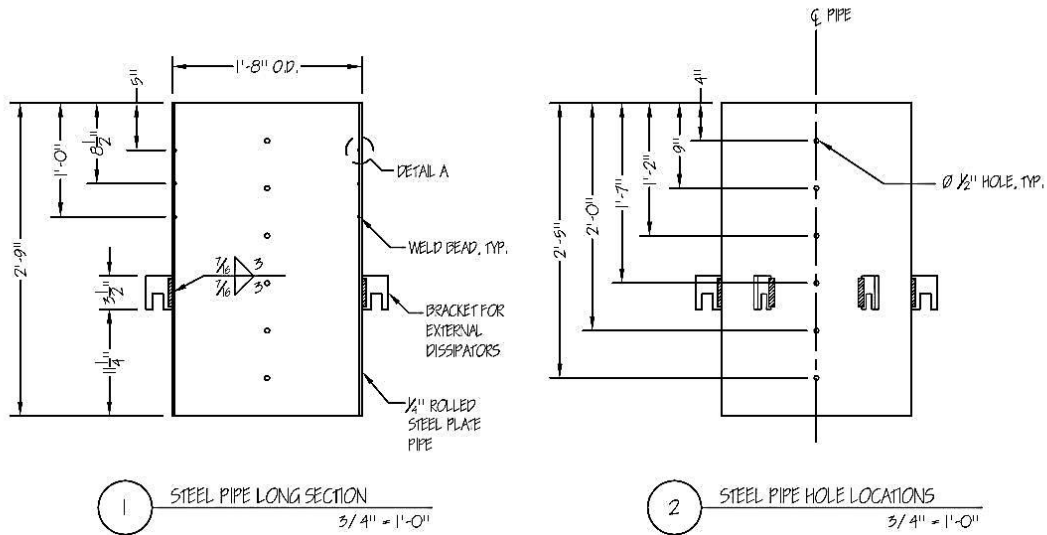
BAR SIZE	QTY
1 3/8"	4

APPROVED FOR PRODUCTION



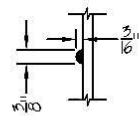
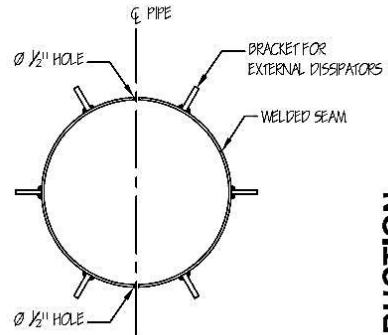
**ADV. PRECAST CONCR. DUAL-SHELL STEEL COLUMNS  
PT BARS AND ACCESSORIES SCHEDULE**

SPECIMEN:	UNIT:	REF:	CONNECTION DETAIL:
	CG	QUASI STATIC - UCSD	HYBRID DUAL-SHELL COLUMN
BY:	CHK:	DATE:	SCALE:
		07/21/11	N15
			SHEET: 07



**NOTES:**

1. ROLLED STEEL PLATE PIPE SHALL BE A572 GRADE 50 AND WELDING SHALL BE COMPLETE JOINT PENETRATION.
2. ALL WELDING SHALL BE USING E70 ELECTRODE.
3. LOCATIONS OF WELD BEAD GIVEN TO CENTER OF BEAD.
4. WELD BEAD SHALL BE PLACED AROUND ENTIRE INNER CIRCUMFERENCE.



**A** WELD BEAD DETAIL  
1/4" = 1"

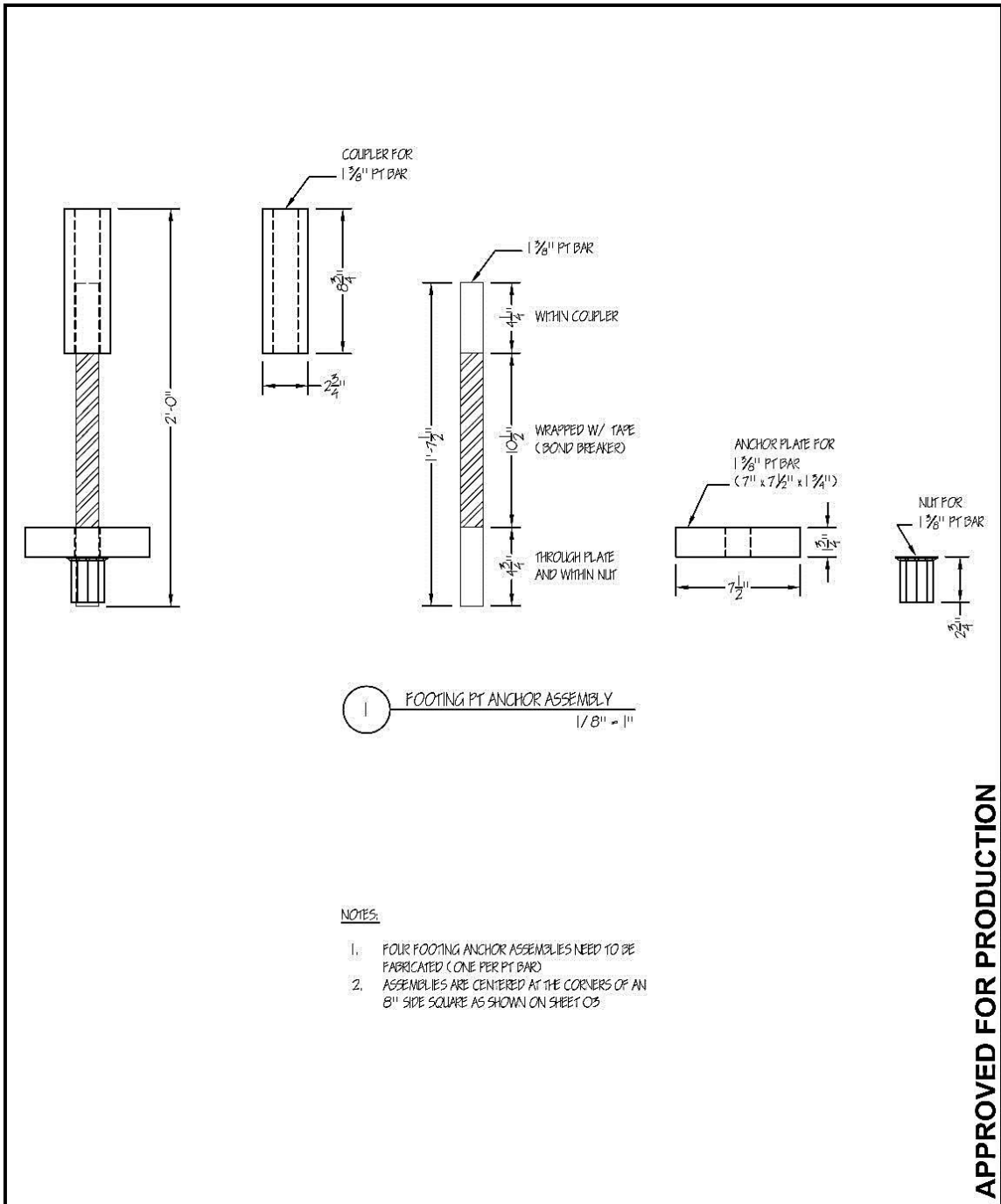
**3** STEEL PIPE SECTION  
3/4" = 1'-0"

**APPROVED FOR PRODUCTION**



**ADV. PRECAST CONCR. DUAL-SHELL STEEL COLUMNS**  
**COLUMN OUTER SHELL DETAIL**


SPECIMEN:	UNIT:	TEST:	CONNECTION DETAIL:
UNIF 1		QUASI STATIC - UCS2	HYBRID DUAL-SHELL COLUMN
BY: CG	CHK:	DATE: 10/10/11	SCALE: AS SHOWN
		SHEET: 08	



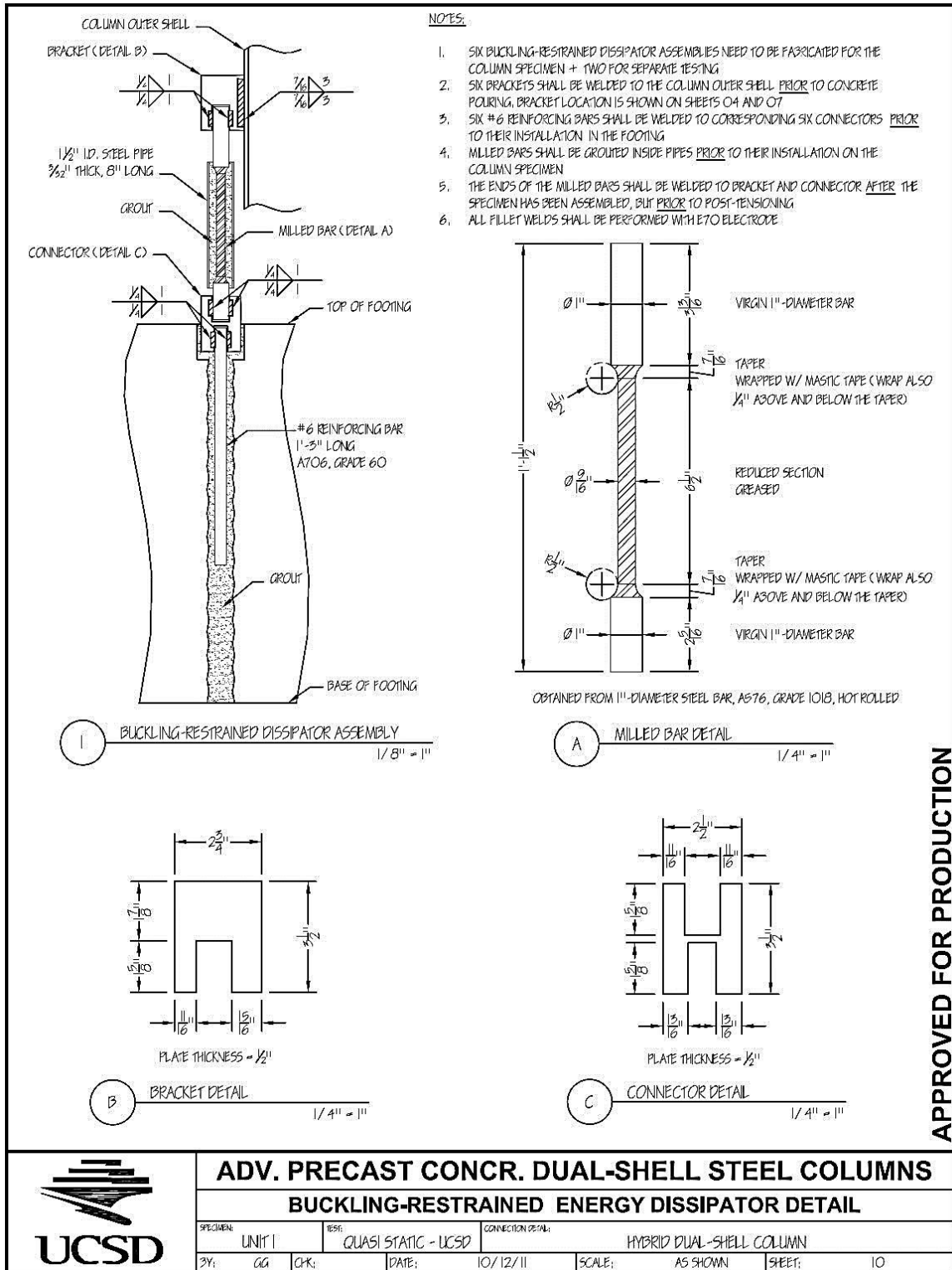
NOTES:

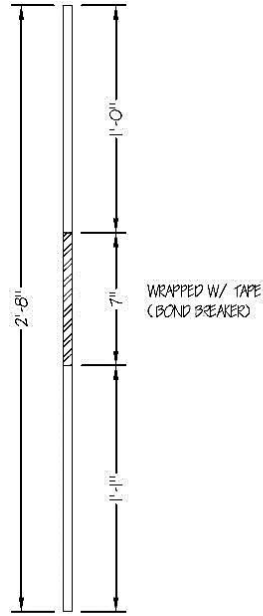
1. FOUR FOOTING ANCHOR ASSEMBLIES NEED TO BE FABRICATED (ONE PER PT BAR)
2. ASSEMBLIES ARE CENTERED AT THE CORNERS OF AN 8" SIDE SQUARE AS SHOWN ON SHEET 05

APPROVED FOR PRODUCTION

	<b>ADV. PRECAST CONCR. DUAL-SHELL STEEL COLUMNS</b>					
	<b>PT-FOOTING ANCHOR SYSTEM DETAIL</b>					
SPECIMEN:	UNIT:	REF:	CONNECTION DETAIL:			
	GG	QUASI STATIC - UCSD	HYBRID DUAL-SHELL COLUMN			
BY:	CHK:	DATE:	SCALE:	SHEET:		
		10/25/11	1/8" = 1"	09		







#4 REBAR, 316LN STAINLESS STEEL

INTERNAL DISSIPATOR ASSEMBLY  
1/8" = 1"

NOTES:

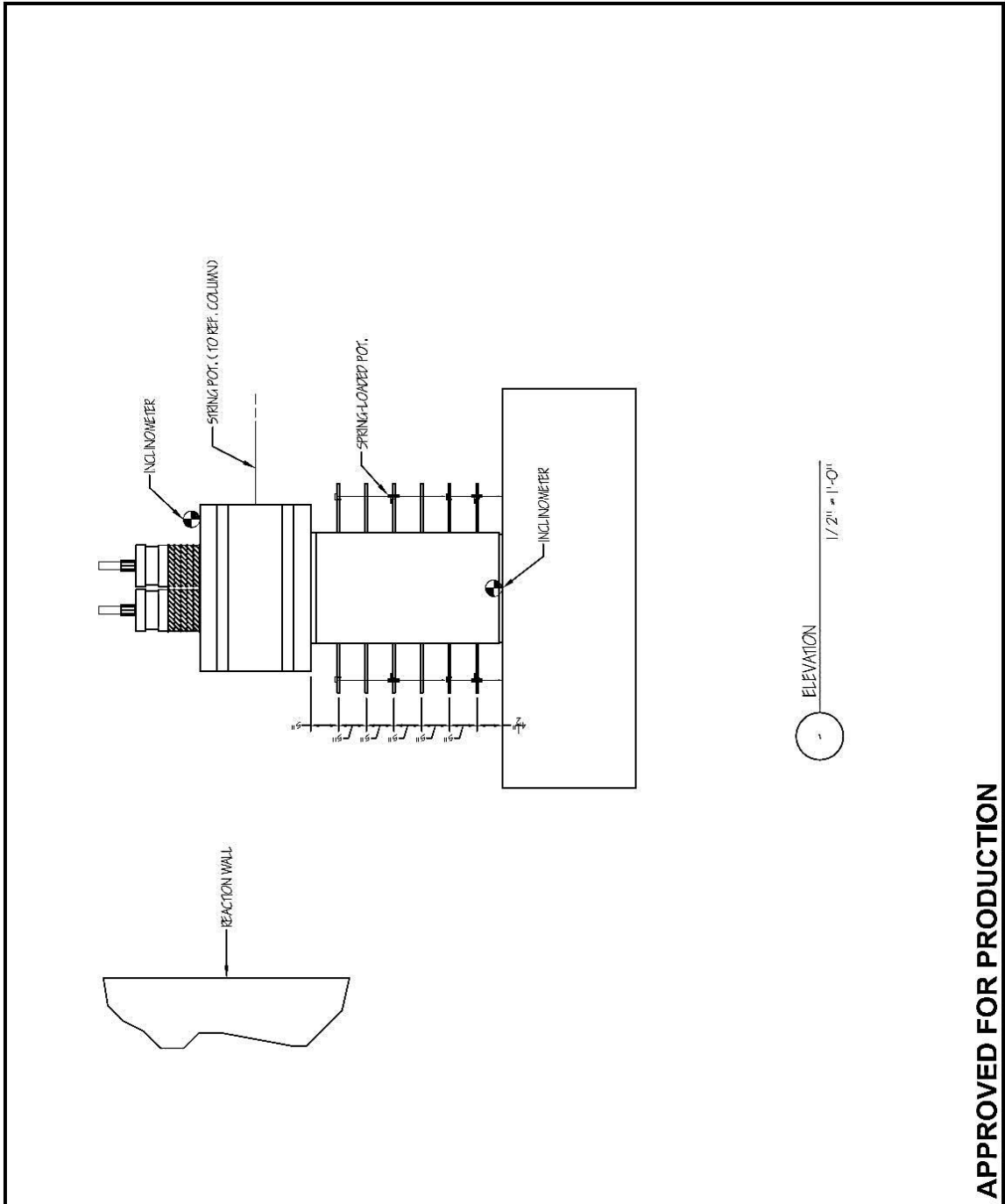
1. SIX INTERNAL DISSIPATORS NEED TO BE PROVIDED FOR THE COLUMN SPECIMEN PLUS THREE FOR MATERIAL TESTING.
2. INTERNAL DISSIPATORS SHALL BE FIRST GROUTED INSIDE THE FOOTING DUCTS.
3. AFTER THE UNIT HAS BEEN PLACED ON THE FOOTING, THE OTHER END OF THE DISSIPATORS SHALL BE GROUTED INSIDE THE COLUMN DUCTS.

APPROVED FOR PRODUCTION




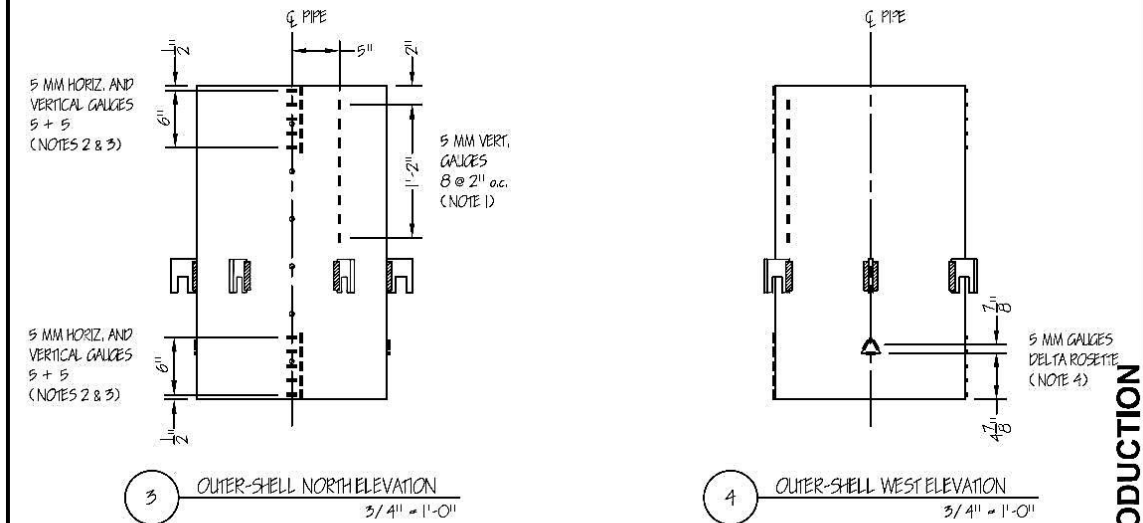
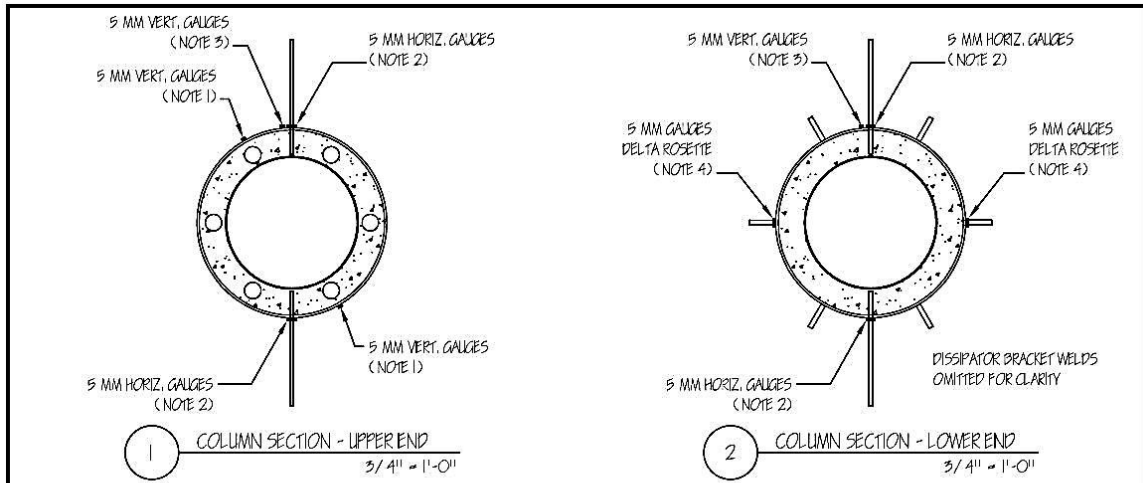
**ADV. PRECAST CONCR. DUAL-SHELL STEEL COLUMNS**  
**INTERNAL ENERGY DISSIPATOR DETAIL**

SPECIMEN: UNIT 1		TEST: QUASI STATIC - UCSD	CONNECTION DETAIL: HYBRID DUAL-SHELL COLUMN		
BY: GG	CHK:	DATE: 12/12/11	SCALE: 1/8" = 1"	SHEET: 11	



APPROVED FOR PRODUCTION

	<b>ADV. PRECAST CONCR. DUAL-SHELL STEEL COLUMNS</b>					
	<b>INSTRUMENTATION PLAN: POTENTIOMETERS AND INCLINOMETERS</b>					
SPECIMEN:	UNIT 1	REF:	QUASI STATIC - UCSD	CONNECTION DETAIL:	HYBRID DUAL-SHELL COLUMN	
DY:	CG	CHK:	DATE:	11/08/11	SCALE:	1/2" = 1'-0"
					SHEET:	12



**NOTES:**

1. VERTICAL STRAIN GAUGES SHALL BE LOCATED ON THE OUTER SHELL, IN FRONT OF TWO DIAMETRICALLY OPPOSITE INTERNAL DISSIPATOR BARS
2. HORIZONTAL STRAIN GAUGES SHALL BE PLACED AT BOTH ENDS, ON THE NORTH AND SOUTH FACES OF THE OUTER SHELL, AT 1/2", 1-3/4", 3", 5", 6-1/2" FROM EACH END
3. VERTICAL STRAIN GAUGES SHALL BE PLACED AT BOTH ENDS, ONLY ON THE NORTH FACE OF THE OUTER SHELL, AT 1/2", 1-3/4", 3", 5", 6-1/2" FROM EACH END
4. ONE DELTA ROSETTE SHALL BE PROVIDED ON THE WEST FACE AND ONE ON THE EAST FACE OF THE OUTER SHELL. STRAIN GAUGES SHALL BE PLACED ALONG THE SIDES OF A 2"-SIDE EQUILATERAL TRIANGLE.

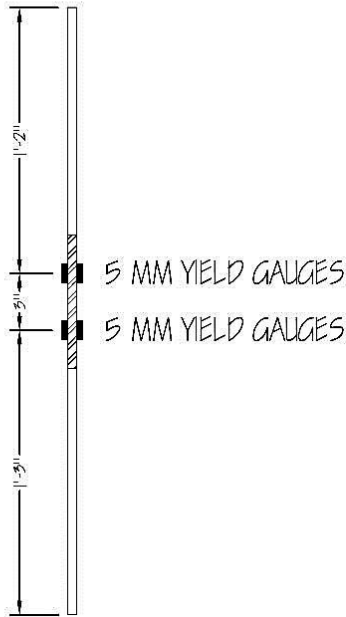
NUMBER OF GAUGES REQUIRED FOR TEST #1:  
5 MM 5 VERT. + 10 HORIZ. (15 TOTAL)

NUMBER OF GAUGES REQUIRED FOR TEST #2:  
5 MM 21 VERT. + 10 HORIZ. (31 TOTAL)

NUMBER OF GAUGES REQUIRED FOR BOTH TESTS:  
5 MM 5 PER ROSETTE (6 TOTAL)

APPROVED FOR PRODUCTION

	<b>ADV. PRECAST CONCR. DUAL-SHELL STEEL COLUMNS</b>							
	<b>INSTRUMENTATION PLAN: OUTER SHELL</b>							
	SPECIMEN:	UNIF 1	TEST:	QUASI STATIC - UCSD	CONNECTION DETAIL:	HYBRID DUAL-SHELL COLUMN		
	BY:	GG	CHK:	DATE:	11/08/11	SCALE:	3/4" = 1'-0"	SHEET:

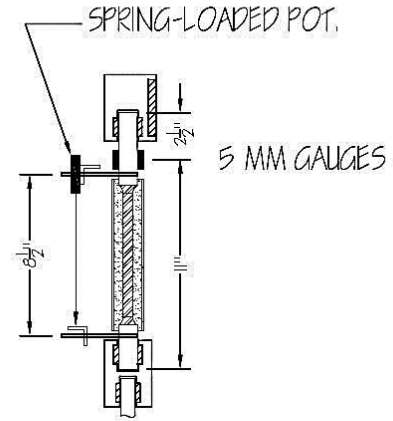


1 INTERNAL DISSIPATOR BAR  
1/8" = 1"

NOTES:

1. TWO DIAMETRICALLY OPPOSITE DISSIPATOR BARS SHALL BE INSTRUMENTED
2. TWO STRAIN GAUGES SHALL BE PROVIDED AT EACH LOCATION, ON OPPOSITE SIDES OF THE BAR

NUMBER OF GAUGES REQUIRED:  
5 MM YIELD 4 EA. BAR (8 TOTAL)



2 BUCKLING-RESTRAINED DISSIPATOR  
1/8" = 1"

NOTES:

1. TWO DIAMETRICALLY OPPOSITE BUCKLING-RESTRAINED DISSIPATORS SHALL BE INSTRUMENTED
2. TWO STRAIN GAUGES SHALL BE PROVIDED AT EACH LOCATION, ON OPPOSITE SIDES OF THE BAR

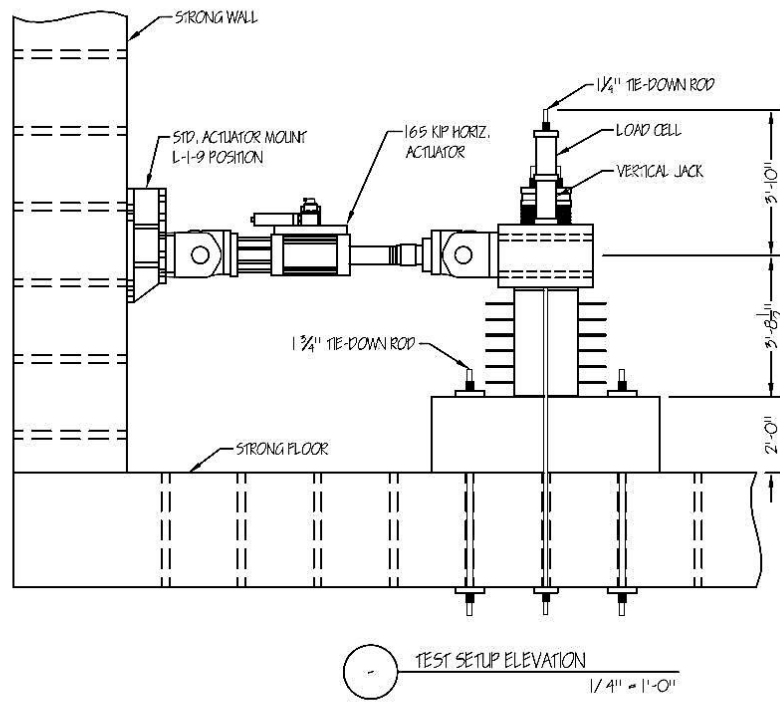
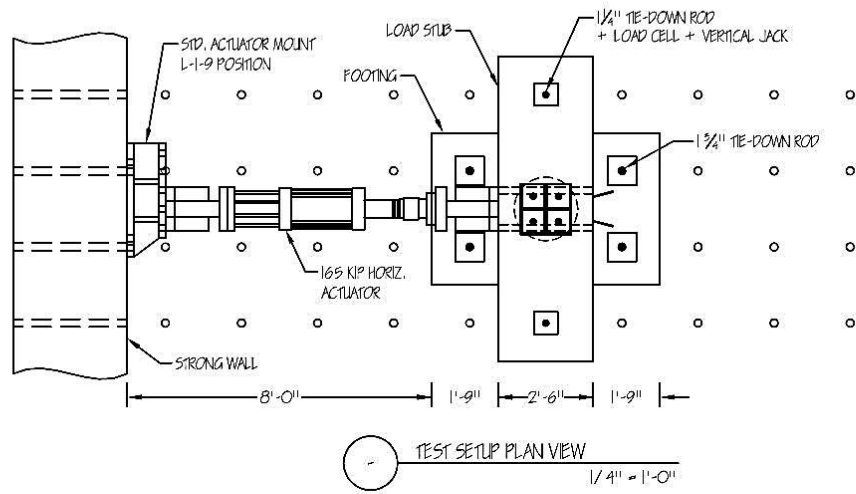
NUMBER OF GAUGES REQUIRED:  
5 MM 2 EA. BAR (4 TOTAL)

APPROVED FOR PRODUCTION



**ADV. PRECAST CONCR. DUAL-SHELL STEEL COLUMNS**  
**INSTRUMENTATION PLAN: ENERGY DISSIPATORS**

SPECIMEN:	UNIT:	TEST:	CONNECTION DETAIL:
	GG	QUASI STATIC - UCSD	HYBRID DUAL-SHELL COLUMN
BY:	CHK:	DATE:	SCALE:
		10/26/11	1/8" = 1"
			SHEET: 14



APPROVED FOR PRODUCTION



**ADV. PRECAST CONCR. DUAL-SHELL STEEL COLUMNS**  
**TEST SETUP OVERVIEW**

SPECIMEN:	UNIT:	TEST:	CONNECTION DETAIL:
	GG	QUASI STATIC - UCSD	HYBRID DUAL-SHELL COLUMN
BY:	GG	CHK:	DATE: 11/08/11
			SCALE: 1/4" = 1'-0"
			SHEET: 15

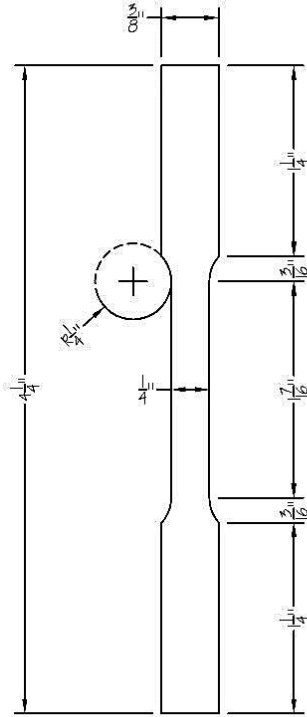


PLATE THICKNESS = 1/2"



NOTES:

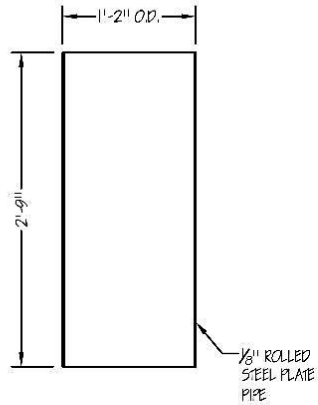
1. THREE COUPONS ARE NEEDED FOR MATERIAL TESTING
2. COUPONS SHALL BE TAKEN FROM THE SAME PLATE USED TO FABRICATE THE COLUMN OUTER SHELL.

APPROVED FOR PRODUCTION

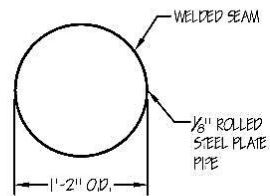


**ADV. PRECAST CONCR. DUAL-SHELL STEEL COLUMNS**  
**OUTER SHELL COUPON DETAIL**

SPECIMEN:	UNIT:	TEST:	CONNECTION DETAIL:
	GG	QUASI STATIC - UCS2	HYBRID DUAL-SHELL COLUMN
BY:	GG	CHK:	DATE: 07/21/11
			SCALE: 1" = 1"
			SHEET: 16



1 STEEL PIPE LONG SECTION  
3/4" = 1'-0"



2 STEEL PIPE SECTION  
3/4" = 1'-0"

NOTES:

1. ROLLED STEEL PLATE PIPE SHALL BE A572 GRADE 50 AND WELDING SHALL BE COMPLETE JOINT PENETRATION.
2. ALL WELDING SHALL BE USING E70 ELECTRODE.

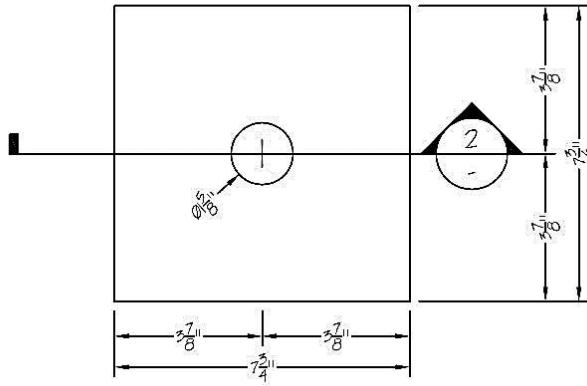
APPROVED FOR PRODUCTION



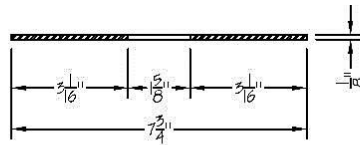
**ADV. PRECAST CONCR. DUAL-SHELL STEEL COLUMNS**  
**COLUMN INNER SHELL DETAIL**

SPECIMEN:	UNIT:	TEST:	CONNECTION DETAIL:
	UNIT 1	QUASI STATIC - UCSD	HYBRID DUAL-SHELL COLUMN
BY:	CG	CHK:	DATE: 08/25/11
			SCALE: 3/4" = 1'-0"
			SHEET: 17





1 SQUARE STEEL PLATE PLAN VIEW  
1/4" = 1"



2 SQUARE STEEL PLATE SECTION  
1/4" = 1"

NOTES:

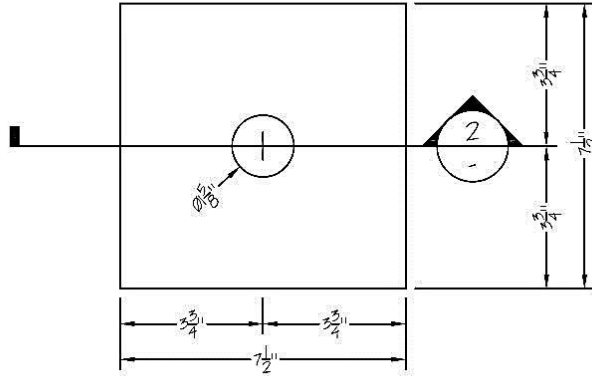
1. PLATES ARE 1/8" THICK
2. PLATES HAVE CENTRAL HOLE WITH 1-5/8" DIAMETER
3. TOLERANCE SMALLER THAN 1/32"
4. 30 PLATES NEED TO BE FABRICATED

APPROVED FOR PRODUCTION

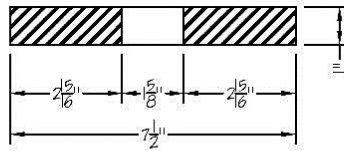


**ADV. PRECAST CONCR. DUAL-SHELL STEEL COLUMNS**  
**SQUARE STEEL PLATE FOR BEARING STACK**

SPECIMEN:	UNIT:	TEST:	CONNECTION DETAIL:
	GG	QUASI STATIC - UCSD	HYBRID DUAL-SHELL COLUMN
BY:	CHK:	DATE:	SCALE:
		10/25/11	1/4" = 1"
			SHEET: 18



1 SQUARE RUBBER PAD PLAN VIEW  
1/4" = 1"



2 SQUARE RUBBER PAD SECTION  
1/4" = 1"

NOTES:

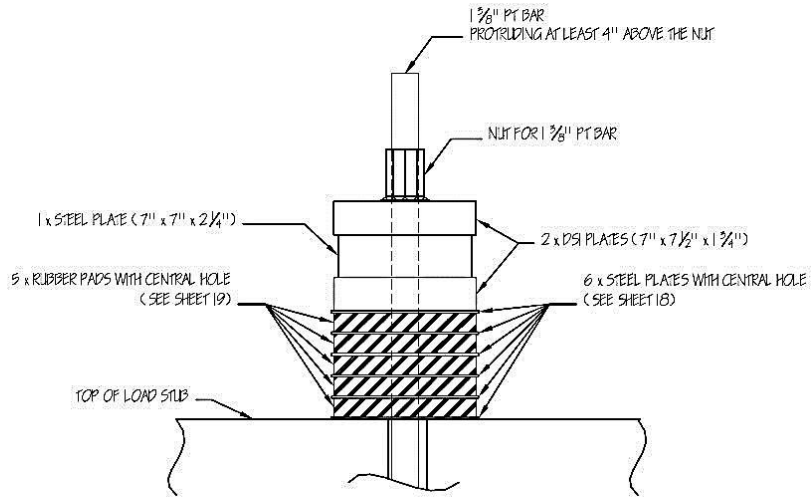
1. PADS ARE 1" THICK
2. PADS HAVE CENTRAL HOLE WITH 1-5/8" DIAMETER
3. SA-47 RUBBER MATERIAL SHALL BE USED
4. TOLERANCE SMALLER THAN 1/32"
5. 23 PADS NEED TO BE FABRICATED, MATERIAL TESTING INCLUDED

APPROVED FOR PRODUCTION



**ADV. PRECAST CONCR. DUAL-SHELL STEEL COLUMNS**  
**SQUARE RUBBER PAD FOR BEARING STACK**

SPECIMEN:	UNIT:	TEST:	CONNECTION DETAIL:
	GG	QUASI STATIC - UCSD	HYBRID DUAL-SHELL COLUMN
BY:	CHK:	DATE:	SCALE:
		10/25/11	1/4" = 1"
			SHEET: 19



LOAD-STUB PT ANCHOR ASSEMBLY  
1/8" = 1"

NOTES:

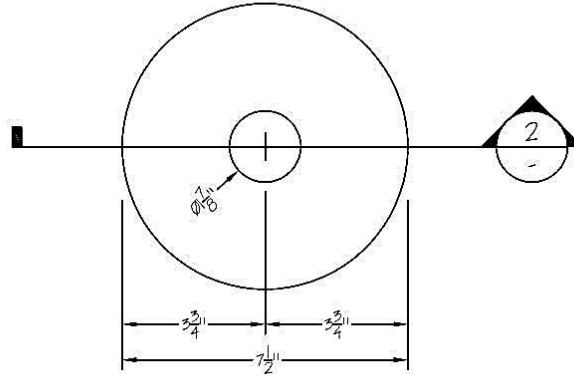
1. THIS SOLUTION IS FOR THE TEST SETUP WITH EXTERNAL DISSIPATORS
2. FOUR LOAD-STUB ANCHOR ASSEMBLIES NEED TO BE PROVIDED (ONE PER PT BAR)

APPROVED FOR PRODUCTION

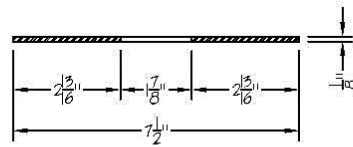


**ADV. PRECAST CONCR. DUAL-SHELL STEEL COLUMNS  
PT-LOAD-STUB ANCHOR SYSTEM DETAIL (W/ EXTERNAL DISSIP.)**

SPECIMEN:	UNIT:	TEST:	CONNECTION DETAIL:
	GG	QUASI STATIC - UCSD	HYBRID DUAL-SHELL COLUMN
DATE:	11/08/11	SCALE:	1/8" = 1"
CHEK:		SHEET:	20



1 CIRCULAR STEEL PLATE PLAN VIEW  
1/4" = 1"



2 CIRCULAR STEEL PLATE SECTION  
1/4" = 1"

NOTES:

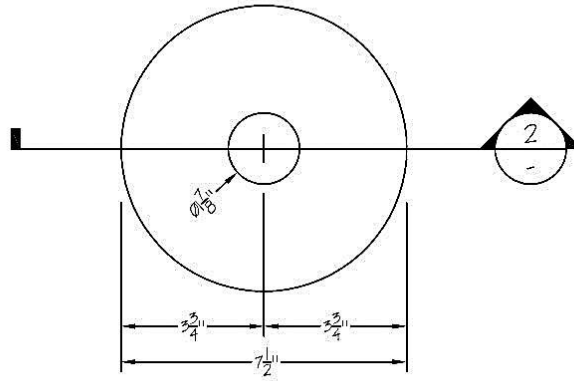
1. PLATES ARE 1/8" THICK
2. PLATES HAVE CENTRAL HOLE WITH 1-3/8" DIAMETER
3. TOLERANCE SMALLER THAN 1/32"
4. 28 PLATES NEED TO BE FABRICATED

APPROVED FOR PRODUCTION

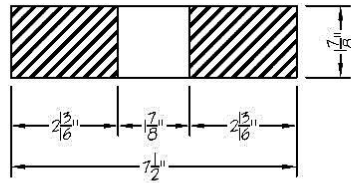


**ADV. PRECAST CONCR. DUAL-SHELL STEEL COLUMNS**  
**CIRCULAR STEEL PLATE FOR BEARING STACK**

SPECIMEN:	UNIT:	TEST:	CONNECTION DETAIL:
		QUASI STATIC - UCSD	HYBRID DUAL-SHELL COLUMN
BY: GG	CHK:	DATE: 10/25/11	SCALE: 1/4" = 1"
			SHEET: 21



1 CIRCULAR FYFE DISC PLAN VIEW  
1/4" = 1"



2 CIRCULAR FYFE DISC SECTION  
1/4" = 1"

NOTES:

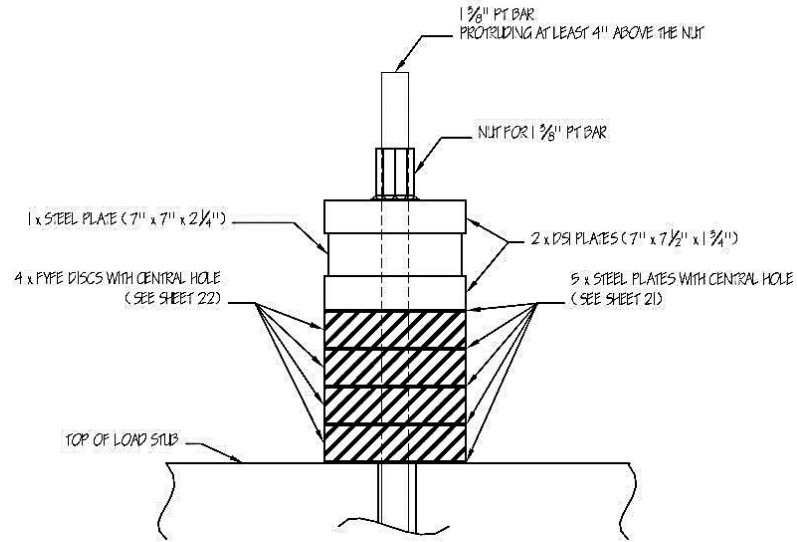
1. DISCS ARE 1-3/8" THICK
2. DISCS HAVE CENTRAL HOLE WITH 1-3/8" DIAMETER
3. 90-DIAMETER-A ADIPRENE MATERIAL SHALL BE USED
4. TOLERANCE SMALLER THAN 1/32"
5. 20 DISCS NEED TO BE FABRICATED, MATERIAL TESTING INCLUDED

APPROVED FOR PRODUCTION



**ADV. PRECAST CONCR. DUAL-SHELL STEEL COLUMNS**  
**CIRCULAR FYFE DISC FOR BEARING STACK**

SPECIMEN:	UNIT:	TEST:	CONNECTION DETAIL:
	GG	QUASI STATIC - UCSD	HYBRID DUAL-SHELL COLUMN
BY:	GG	CHK:	DATE: 10/25/11
			SCALE: 1/4" = 1"
			SHEET: 22



LOAD-STUB PT ANCHOR ASSEMBLY  
1/8" = 1"

NOTES:

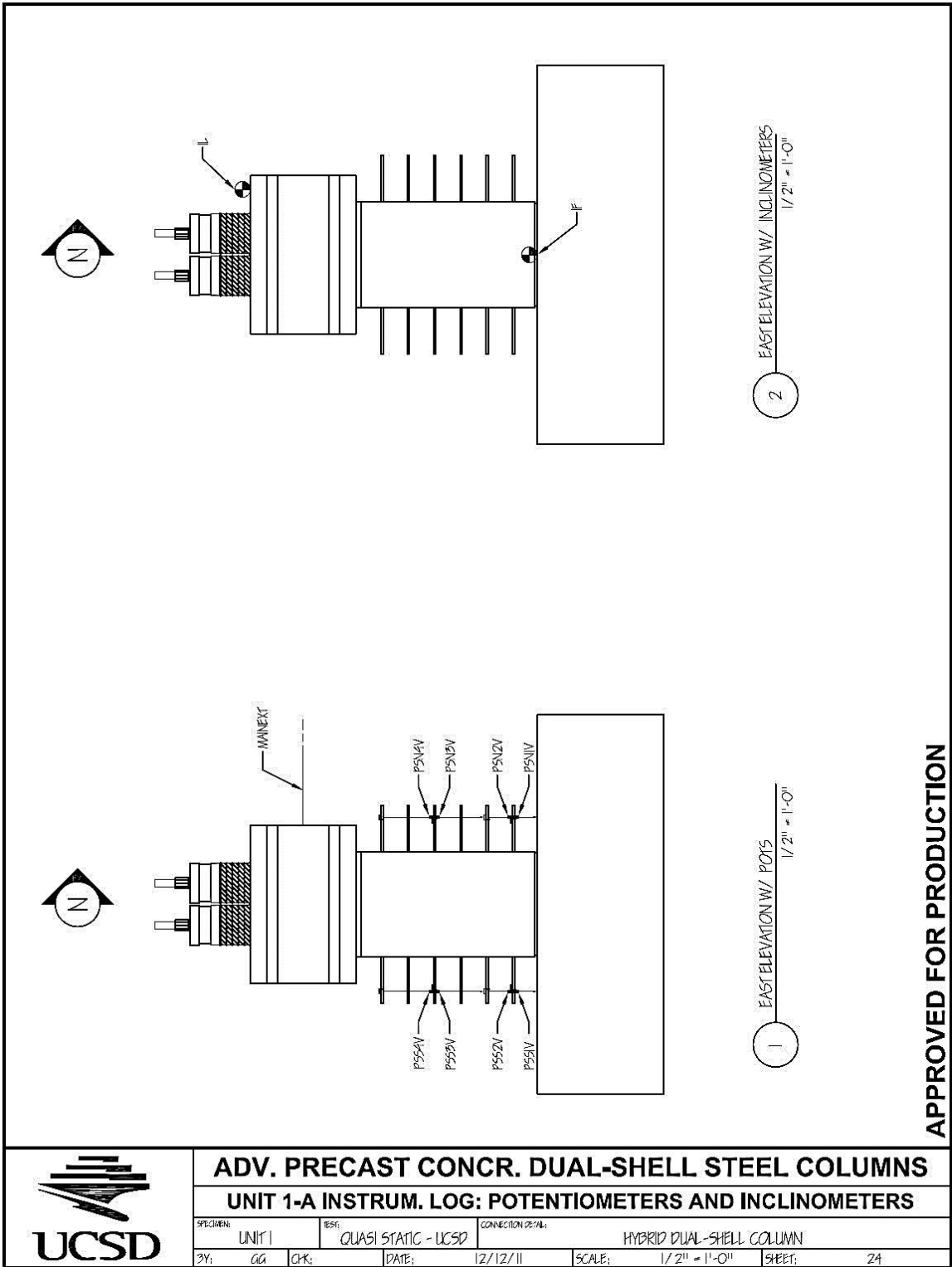
1. THIS SOLUTION IS FOR THE SETUP WITH INTERNAL ENERGY DISSIPATORS
2. FOUR LOAD-STUB ANCHOR ASSEMBLIES NEED TO BE PROVIDED (ONE PER PT BAR)

APPROVED FOR PRODUCTION



**ADV. PRECAST CONCR. DUAL-SHELL STEEL COLUMNS  
PT-LOAD-STUB ANCHOR SYSTEM DETAIL (W/ INTERNAL DISSIP.)**

SPECIMEN:	UNIT:	TEST:	CONNECTION DETAIL:
	GG	QUASI STATIC - UCSD	HYBRID DUAL-SHELL COLUMN
DATE:	SCALE:	SHEET:	
12/12/11	1/8" = 1"	23	

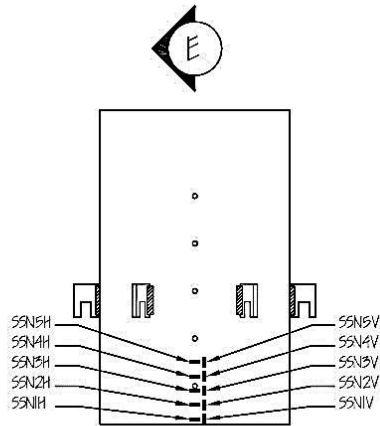


APPROVED FOR PRODUCTION

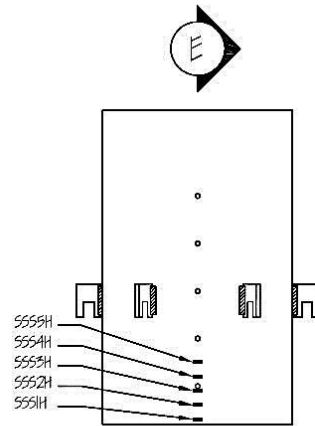


**ADV. PRECAST CONCR. DUAL-SHELL STEEL COLUMNS**  
**UNIT 1-A INSTRUM. LOG: POTENTIOMETERS AND INCLINOMETERS**

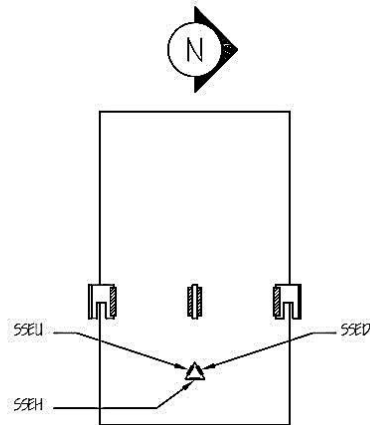
SPECIMEN:	UNIT: 1	TEST:	QUASI STATIC - UCSD	CONNECTION DETAIL:	HYBRID DUAL-SHELL COLUMN
BY:	GG	CHK:		DATE:	12/12/11
			SCALE:	1/2" = 1'-0"	SHEET: 24



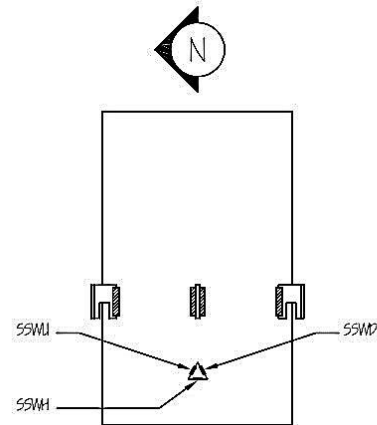
1 OUTER-SHELL NORTH ELEVATION  
3/4" = 1'-0"



2 OUTER-SHELL SOUTH ELEVATION  
3/4" = 1'-0"



3 OUTER-SHELL EAST ELEVATION  
3/4" = 1'-0"



4 OUTER-SHELL WEST ELEVATION  
3/4" = 1'-0"

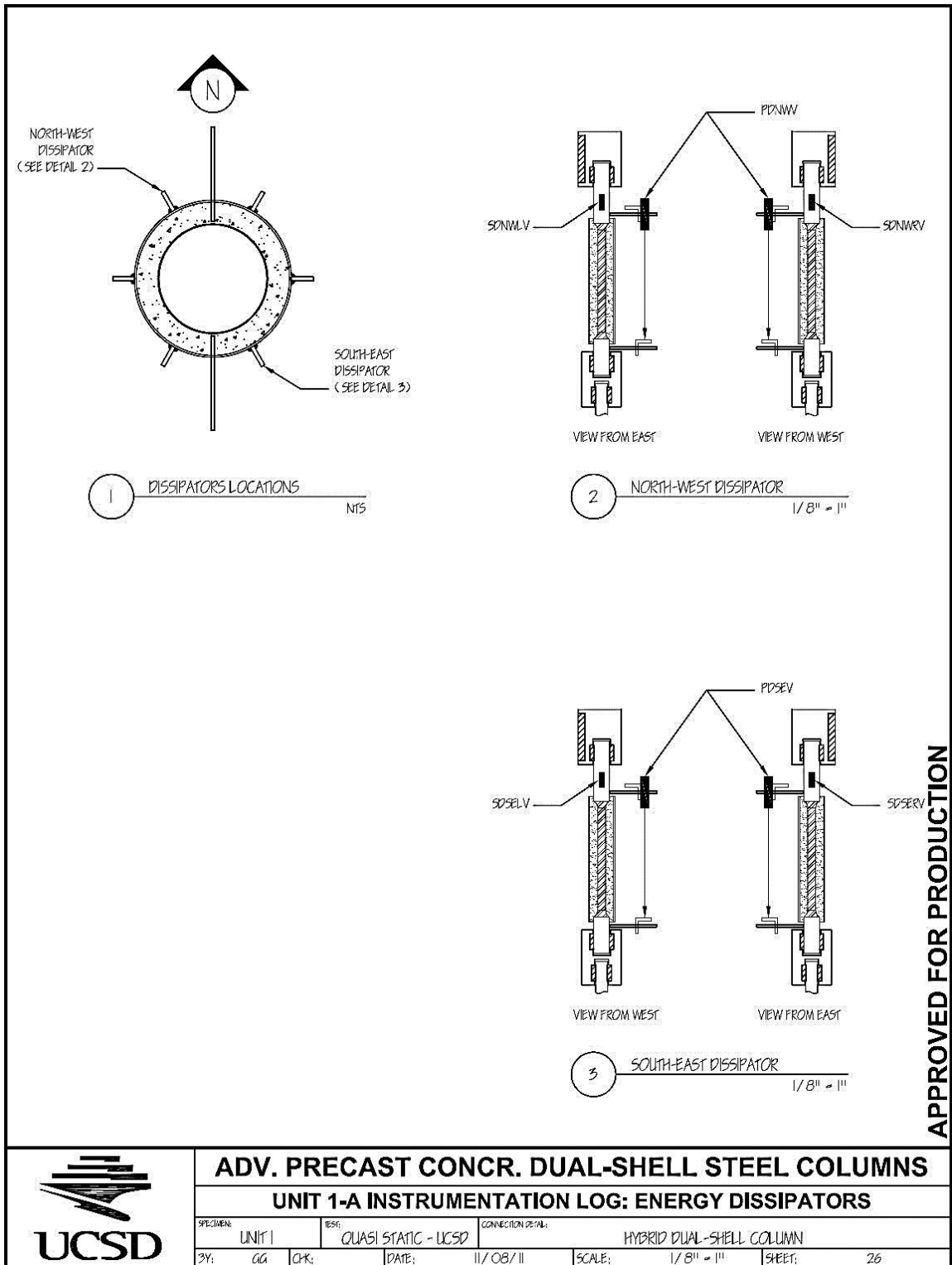
APPROVED FOR PRODUCTION

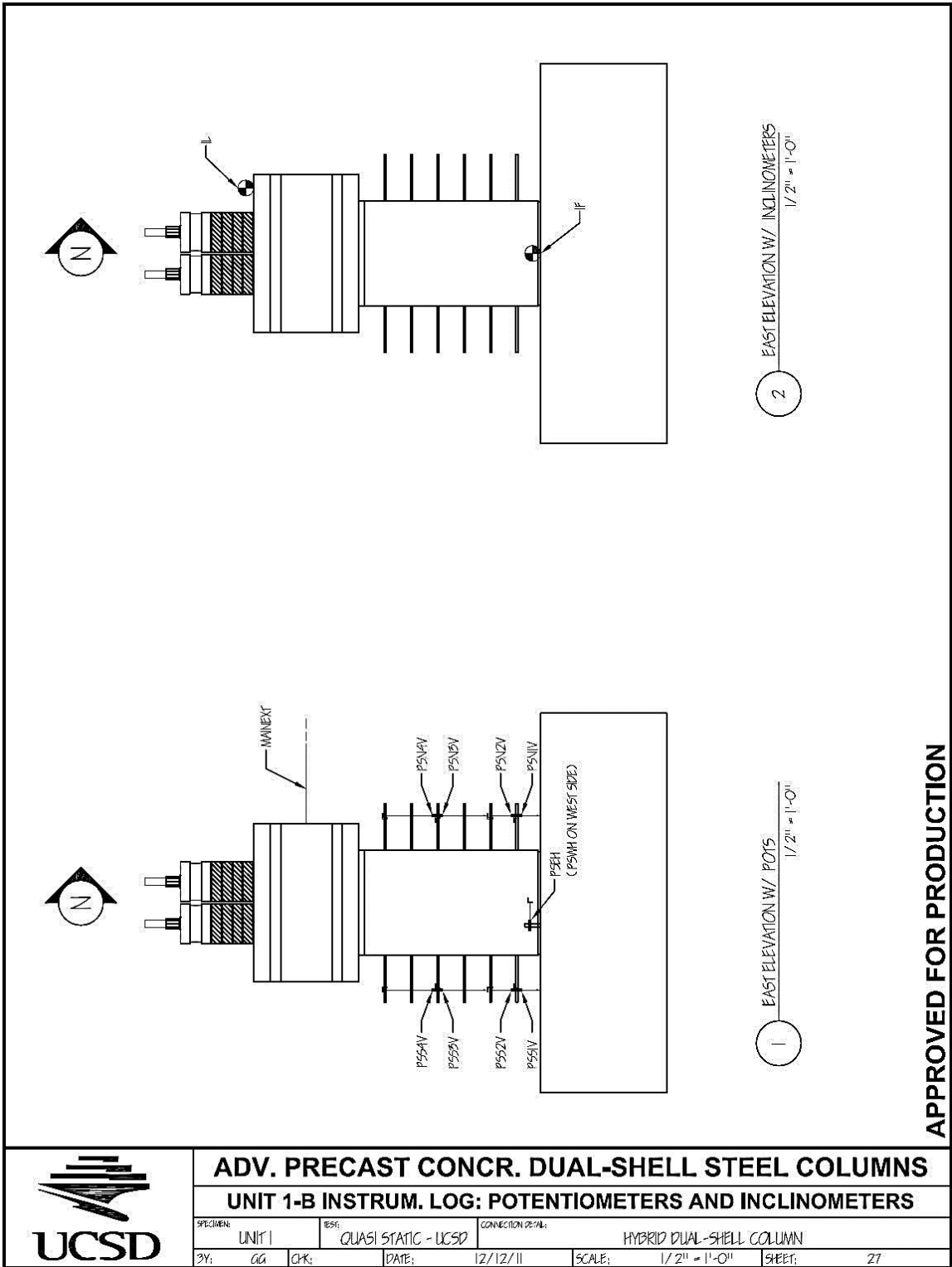


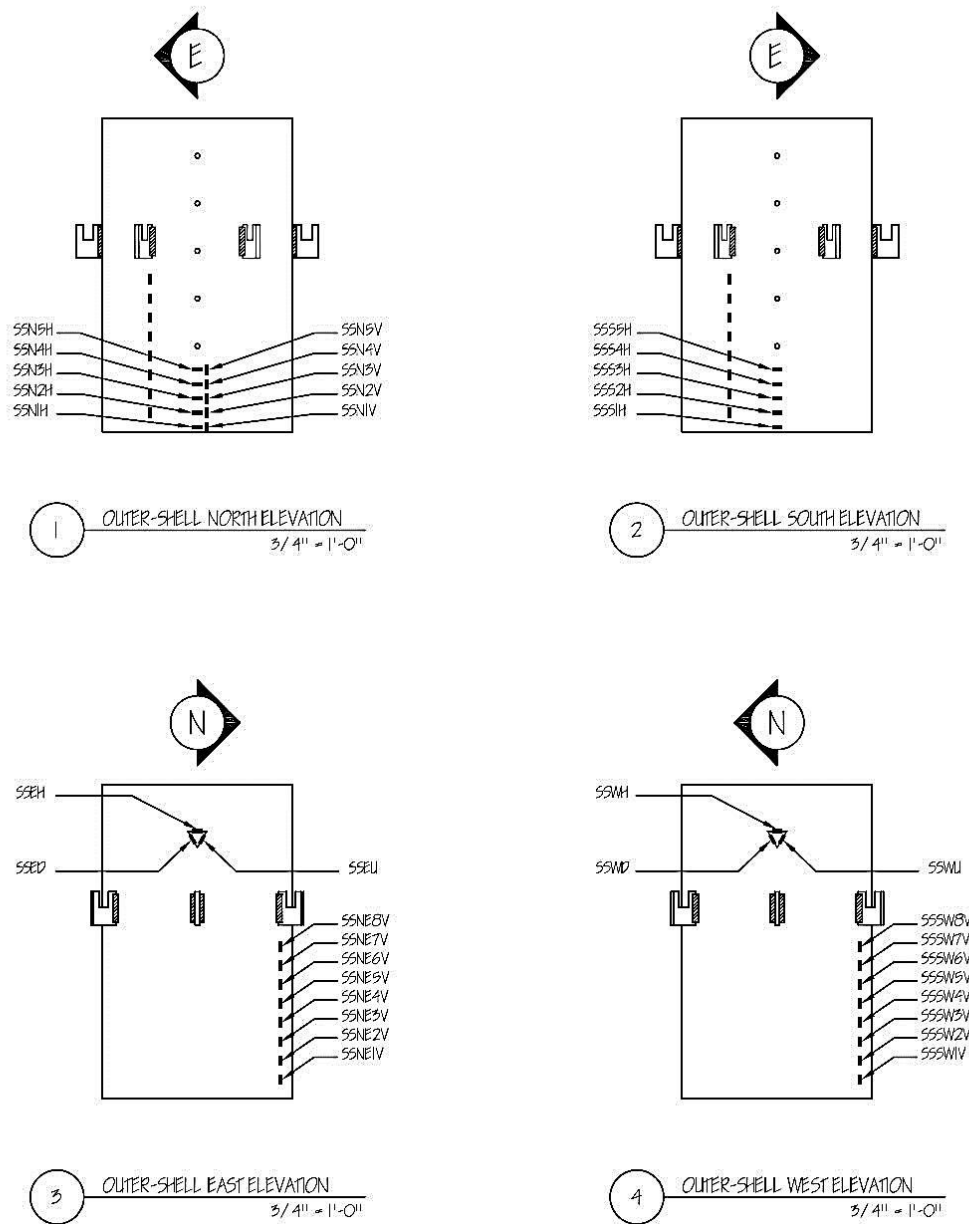
**ADV. PRECAST CONCR. DUAL-SHELL STEEL COLUMNS**  
**UNIT 1-A INSTRUMENTATION LOG: OUTER SHELL**

SPECIMEN:	UNIT 1	TEST:	QUASI STATIC - UCSD	CONNECTION DETAIL:	HYBRID DUAL-SHELL COLUMN
BY:	GG	CHK:		DATE:	12/12/11
				SCALE:	3/4" = 1'-0"
				SHEET:	25




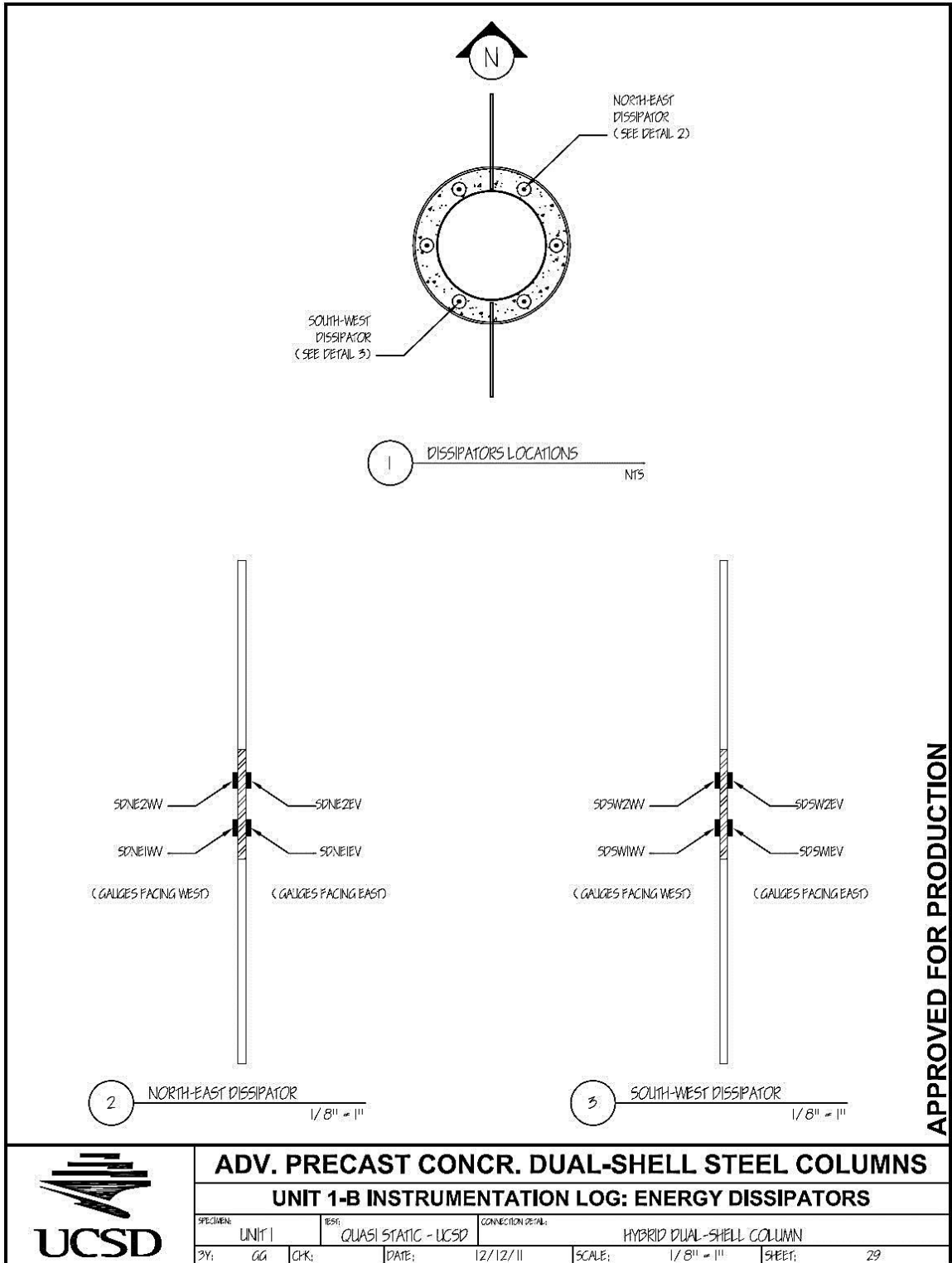






APPROVED FOR PRODUCTION

	<b>ADV. PRECAST CONCR. DUAL-SHELL STEEL COLUMNS</b>					
	<b>UNIT 1-B INSTRUMENTATION LOG: OUTER SHELL</b>					
	SPECIMEN: UNIT 1		TEST: QUASI STATIC - UCSD		CONNECTION DETAIL: HYBRID DUAL-SHELL COLUMN	
	BY: GG	CHK:	DATE: 12/12/11	SCALE: 3/4" = 1'-0"	SHEET: 28	

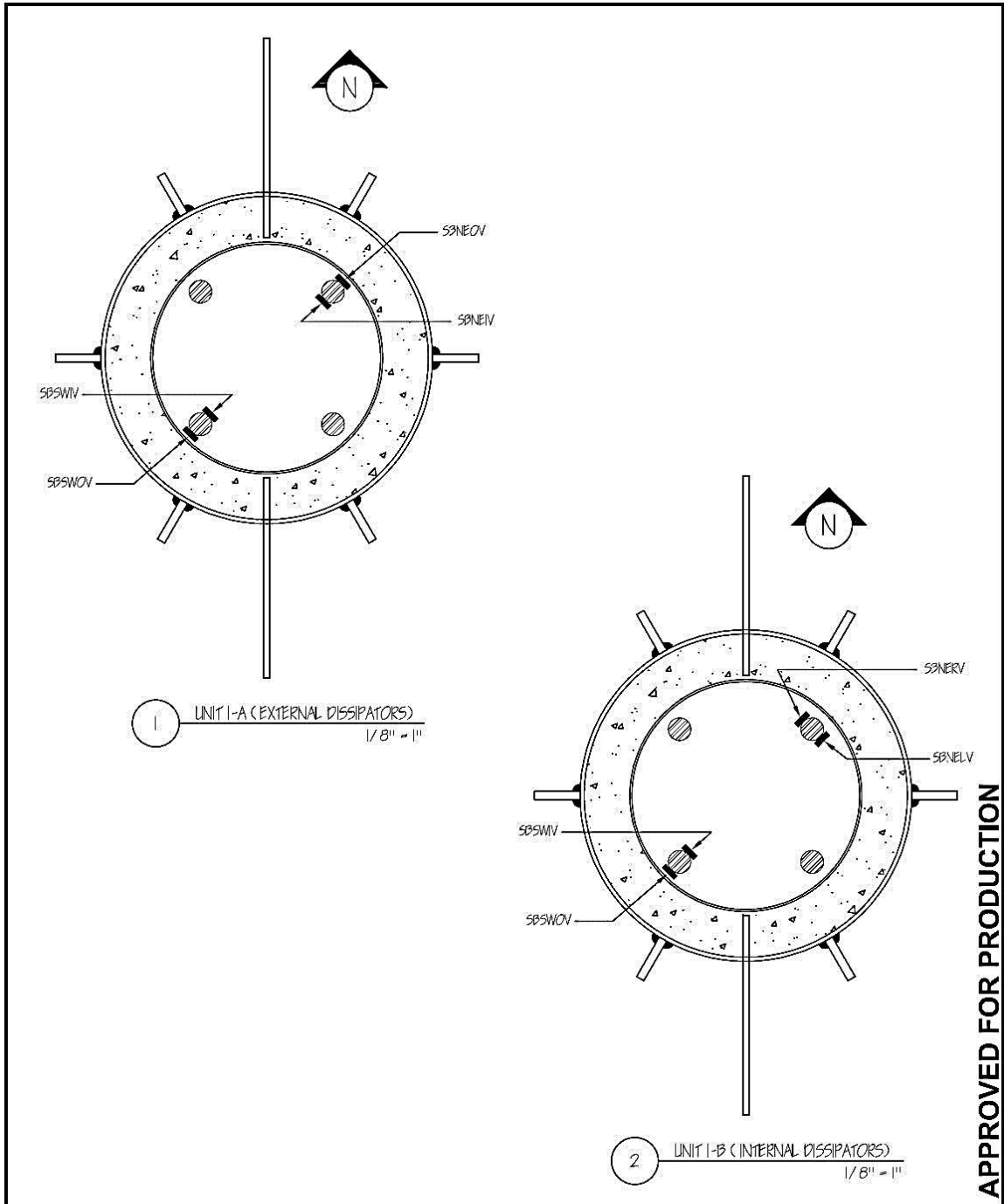


APPROVED FOR PRODUCTION



**ADV. PRECAST CONCR. DUAL-SHELL STEEL COLUMNS**  
**UNIT 1-B INSTRUMENTATION LOG: ENERGY DISSIPATORS**

SPECIMEN:	UNIT 1	TEST:	QUASI STATIC - UCSD	CONNECTION DETAIL:	HYBRID DUAL-SHELL COLUMN
BY:	GG	CHK:		DATE:	12/12/11
			SCALE:	1/8" = 1"	SHEET: 29



APPROVED FOR PRODUCTION

	<b>ADV. PRECAST CONCR. DUAL-SHELL STEEL COLUMNS</b>						
	<b>UNITS 1-A &amp; 1-B INSTRUMENTATION LOG: PT BAR STRAIN GAUGES</b>						
	SPECIMEN:	UNIT 1	TEST:	QUASI STATIC - UCSD	CONNECTION DETAIL:	HYBRID DUAL-SHELL COLUMN	
	BY:	GG	CHK:		DATE:	12/12/11	SCALE:
		SHEET:	30				

## REFERENCES

- AASHTO (2012). "AASHTO LRFD Bridge Design Specifications, 6th Edition". American Association of State Highway and Transportation Officials, Washington, DC.
- ASTM (2010). "Standard Specification for Corrugated Steel Pipe, Metallic-Coated for Sewers and Drains". *ASTM Designation A760/A760M-10*, American Society for Testing and Materials, Philadelphia, PA.
- Boyd, P.F., Cofer, W.F., and McLean, D.I. (1995). "Seismic Performance of Steel-Encased Composite Columns under Flexural Loading". *ACI Structural Journal*. **92:3**, 335-364.
- Bradford, M.A. (1996). "Design Strength of Slender Concrete-Filled Rectangular Steel Tubes". *ACI Structural Journal*. **93:2**, 229-235.
- Caltrans (2010). "Seismic Design Criteria". California Dept. of Transportation, Sacramento, CA.
- Carr, A.J. (2008). "Ruaumoko Manual". Department of Civil Engineering, University of Canterbury, Christchurch, New Zealand.
- Christopoulos, C., Filiatrault, A., Uang, C.-M., and Folz, B. (2002). "Post-Tensioned Energy Dissipating Connections for Moment Resisting Steel Frames". *ASCE Journal of Structural Engineering*. **128:9**, 1111-1120.
- Cormack, L.G. (1998). "The Design and Construction of the Major Bridges on the Mangaweka Rail Deviation." *Transactions of the Institute of Professional Engineers of New Zealand*. **15**, 6-23.
- Culmo, M.P. (2011). "Accelerated Bridge Construction - Experience in Design, Fabrication and Erection of Prefabricated Bridge Elements and Systems". *FHWA Report HIF-12-013*.
- El-Sheikh, M.T., Sause, R., Pessiki, S., and Lu, L.-W. (1999). "Seismic Behaviour and Design of Unbonded Post-Tensioned Precast Concrete Frames". *PCI Journal*, **44:3**, 54-71.

- FHWA (2012). <http://www.fhwa.dot.gov/bridge/abc/index.cfm>
- Filippou, F.C., Popov, E.P., and Bertero, V.V (1983). "Effects of Bond Deterioration on Hysteretic Behavior of Reinforced Concrete Joints". *Report No. UCB/EERC-83/19*, Earthquake Engineering Research Center, University of California at Berkeley, Berkeley, CA.
- Ge, H. and Usami, T. (1992). "Strength of Concrete-Filled Thin Walled Steel Box Columns: Experiment". *ASCE Journal of Structural Engineering*. **118:11**, 3036-3054.
- Ge, H. and Usami, T. (1994). "Strength Analysis of Concrete Filled Thin Walled Steel Box Columns". *Journal of Constructional Steel Research*. **37**, 607-612.
- Gebman, M., Ashford, S., and Restrepo, J.I. (2006). "Axial Force Transfer Mechanisms within Cast-In-Steel-Shell Piles". *Report No. SSRP-94/10*, Department of Structural Engineering, University of California at San Diego, La Jolla, CA.
- Ghosh, R.S. (1977). "Strengthening of Slender Hollow Steel Columns by Filling with Concrete". *Canadian Journal of Civil Engineering*. **4:2**, 127-133.
- Guerrini, G., and Restrepo, J.I., (2011). "Advanced Precast Concrete Dual-Shell Steel Columns". *Proceedings of the 8th International Conference on Urban Earthquake Engineering*. **Vol I**, 1125-1129, Tokyo, Japan.
- Heiber D.G., (2005). "Precast Concrete Pier Systems for Rapid Construction of Bridges in Seismic Regions". *Report No. WA-RD 611.1*, Washington Department of Transportation, Olympia, WA.
- Hewes, J.T. and Priestley, M.J.N. (2002). "Seismic Design and Performance of Precast Concrete Segmental Bridge Columns". *Report No. SSRO-2001/25*, Department of Structural Engineering, University of California at San Diego, La Jolla, CA.
- Holden, T., Restrepo, J.I., and Mander, J.B (2003). "Seismic Performance of Precast Reinforced and Prestressed Concrete Walls". *ASCE Journal of Structural Engineering*. **129:3**, 286-296.
- Itani, A.M. (1996). "Future Use of Composite Steel-Concrete Columns in Highway Bridges". *AISC Engineering Journal*. **33:3**, 110-115.
- Karthik, M.M. and Mander, J.B. (2011). "Stress-Block Parameters for Unconfined and Confined Concrete Based on a Unified Stress-Strain Model". *ASCE Journal of Structural Engineering*. **137:2**, 270-273.
- Kato, B. (1996). "Column Curves of Steel-Concrete Composite Members". *Journal of Constructional Steel Research*. **39:2**, 121-135.

- Kitada, T. (1998). "Ultimate Strength and Ductility of State-of-the-Art Concrete-Filled Steel Bridges Piers in Japan". *Engineering Structures*. **20:4-6**, 347-354.
- Knowles, R.B. and Park, R. (1969). "Strength of Concrete Filled Steel Tubular Columns". *ASCE Journal of the Structural Division*. **95:12**, 2565-2587.
- Kurama, Y., Sause, R., Pessiki, S., and Lu, L.-W. (1999). "Lateral Load Behavior and Seismic Design of Unbonded Post-Tensioned Precast Concrete Walls". *ACI Structural Journal*, **96:4**, 622-632.
- Kwan, W.P. and Billington, S. (2003). "Unbonded Posttensioned Concrete Bridge Piers. I: Monotonic and Cyclic Analyses". *ASCE Journal of Bridge Engineering*, **8:2**, 92-101.
- Kwan, W.P. and Billington, S. (2003). "Unbonded Posttensioned Concrete Bridge Piers. II: Seismic Analyses". *ASCE Journal of Bridge Engineering*, **8:2**, 102-111.
- Leon, R.T., Kim, D.K., and Hajjar, J.F. (2007). "Limit State Response of Composite Columns and Beam-Columns: Formulation of Design Provisions for the 2005 AISC Specification". *AISC Engineering Journal*, **44:4**, 341-358.
- Li, B., Park, R., and Tanaka, H. (1994). "Strength and Ductility of Reinforced Concrete Members and Frames Constructed Using High-Strength Concrete". *Research Report 94-5*, Department of Civil Engineering, University of Canterbury, Christchurch, New Zealand.
- MacRae, G.A., and Priestley, M.J.N. (1994). "Precast Post-Tensioned UngROUTED Concrete Beam-Column Subassembly Tests". *Report No. SSRP-94/10*, Department of Applied Mechanics and Engineering Sciences, University of California at San Diego, La Jolla, CA.
- Makris, N. and Roussos, Y. (1998). "Rocking response and overturning of equipment under horizontal-type pulses". *Report No PEER 1998/05*, Pacific Earthquake Engineering Research Center, Berkeley, CA.
- Mander, J.B., Priestley, M.J.N., and Park, R. (1988). "Theoretical Stress-Strain Model for Confined Concrete". *ASCE Journal of Structural Engineering*. **114:8**, 1804-1826.
- Mander, J.B. and Cheng, C.-T. (1997). "Seismic Resistance of Bridge Piers Based on Damage Avoidance Design". *Technical Report NCEER-97-0014*, NCEER, Department of Civil and Environmental Engineering, State University of New York at Buffalo, Buffalo, NY.
- Marriott, D., Pampanin, S., and Palermo, A. (2009). "Quasi-Static and Pseudo-Dynamic Testing of Unbonded Post-Tensioned Rocking Bridge Piers with External Replaceable Dissipaters". *Earthquake Engineering and Structural Dynamics*. **38**, 331-354.



- Marriott, D., Pampanin, S., and Palermo, A. (2011). "Biaxial Testing of Unbonded Post-Tensioned Rocking Bridge Piers with External Replaceable Dissipaters". *Earthquake Engineering and Structural Dynamics*. **40**, 1723–1741.
- Matsui, C., Tsuda, K., and Ishibashi, Y. (1995). "Slender Concrete Filled Steel Tubular Columns under Combined Compression and Bending". *Proceedings of the 4th Pacific Structural Steel Conference*. **Vol. III**, 29-36, Steel-Concrete Composite Structures.
- Mazzoni, S., McKenna, F., Scott, M.H., Fenves, G.L. et al. (2007), "Opensees Command Language Manual". Pacific Earthquake Engineering Research Center, Berkeley, CA.
- McKenna, F., Scott, M.H., and Fenves, G.L. (2010). "Nonlinear Finite Element Analysis Software Architecture Using Object Composition". *ASCE Journal of Computing in Civil Engineering*. **24:1**, 95-107.
- Nakaki, S.D., Stanton, J. F., and Sritharan, S. (1999). "An Overview of the PRESSS Five-Story Precast Test Building". *PCI Journal*, **44:2**, 26-39.
- Neogi, P.K., Sen, H.K., and Chapman, J.C. (1969). "Concrete-Filled Tubular Steel Columns Under Eccentric Loading". *The Structural Engineer*. **47:5**, 187-195.
- O'Brien, A.D. and Rangan, B.V. (1993). "Tests on Slender Tubular Steel Columns Filled with High-Strength Concrete". *Australian Civil Engineering Transactions*. **35:4**, 287-292.
- O'Shea, M.D. and Bridge, R.Q. (1995). "Circular Thin Walled Concrete Filled Steel Tubes". *Proceedings of the 4th Pacific Structural Steel Conference*. **Vol. III**, 53-60, Steel-Concrete Composite Structures.
- Ou, Y.-C., Chiewanichakorn, M., Ahn, I.-S., Aref, A.J., Chen, S.S., Filiatrault, A., and Lee, G.C. (2006). "Cyclic Performance of Precast Concrete Segmental Bridge Columns: Simplified Analytical and Finite Element Studies". *Transportation Research Record: Journal of the Transportation Research Board*. **1976**, 66-74.
- Ou, Y.-C., Wang, P.-H., Tsai, M.-S., Chang, K.-C., and Lee, G.C. (2010). "Large-Scale Experimental Study of Precast Segmental Unbonded Posttensioned Concrete Bridge Columns for Seismic Regions". *ASCE Journal of Structural Engineering*. **136:3**, 255-264.
- Palermo, A. and Pampanin, S. (2008). "Enhanced Seismic Performance of Hybrid Bridge Systems: Comparison with Traditional Monolithic Solutions". *Journal of Earthquake Engineering*. **12:8**, 1267-1295.
- Palermo, A., Pampanin, S., and Calvi, G.M. (2005). "Concept and Development of Hybrid Solutions for Seismic Resistant Bridge Systems". *Journal of Earthquake Engineering*. **9:6**, 899-921.

- Palermo, A., Pampanin, S., and Marriott, D. (2007). "Design, Modeling, and Experimental Response of Seismic Resistant Bridge Piers with Posttensioned Dissipating Connections". *ASCE Journal of Structural Engineering*. **133:11**, 1648-1661.
- Park, R.J.T. and Paulay, T. (1990). "Strength and Ductility of Concrete Substructures of Bridges". *Transit New Zealand - Road Research Unit Bulletin*. **84:1**, 14-29.
- Park, R.J.T., Priestley, M.J.N., and Walpole, W.R. (1983). "The Seismic Performance of Steel Encased Reinforced Concrete Bridge Piles". *Bulletin of the New Zealand National Society for Earthquake Engineering*. **16:2**, 123-140.
- Paulay, T. and Priestley, M.J.N. (1992). *Seismic Design of Reinforced Concrete and Masonry Buildings*. John Wiley and Sons, New York, NY.
- Pérez, F.J., Pessiki, S., Sause, R., and Lu, L.-W. (2003). "Lateral Load Tests of Unbonded Post-Tensioned Precast Concrete Walls". *Special Publication of Large-Scale Structural Testing, Paper No. SP 211-8*, American Concrete Institute, Detroit, 161-182.
- Priestley, M.J.N., Sritharan, S., Conley, J.R., and Pampanin, S. (1999). "Preliminary Results and Conclusions from the PRESSS Five-Story Precast Concrete Test Building". *PCI Journal*, **44:6**, 42-67.
- Priestley, M.J.N. and Tao, J.R.T. (1993). "Seismic Response of Precast Prestressed Concrete Frames with Partially Debonded Tendons". *PCI Journal*. **38:1**, 58-69.
- Prion, H.G.L. and Boehme J. (1989). "Beam-Column Behaviour of Steel Tubes Filled with High-Strength Concrete". *Fourth International Colloquium*, SSRC, New York, 439-449.
- Rangan, B.V. and Joyce, M. (1992). "Strength of Eccentrically Loaded Slender Steel Tubular Columns Filled with High Strength Concrete". *ACI Structural Journal*. **89:6**, 676-681.
- Restrepo, J.I. and Rahman, A. (2007). "Seismic Performance of Self-Centering Structural Walls Incorporating Energy Dissipators". *ASCE Journal of Structural Engineering*. **133:11**, 1560-1570.
- Restrepo, J.I., Tobolski, M.J., and Matsumoto, E.E. (2011). "Development of a Precast Bent Cap System for Seismic Regions". *NCHRP Report 681*.
- Sakai, J. and Mahin, S.A. (2004). "Analytical Investigations of New Methods for Reducing Residual Displacements of Reinforced Concrete Bridge Columns". *Report No. PEER 2004/02*, Pacific Earthquake Engineering Research Center, Berkeley, CA.
- Sakai, J., Jeong, H., and Mahin, S.A. (2006). "Reinforced Concrete Bridge Columns that

- Recenter Following Earthquakes". *Proceedings of the 8th U.S. National Conference on Earthquake Engineering*, Paper No. 1421, San Francisco, CA.
- Sakino, K. and Ishibashi, H. (1985). "Experimental Studies on Concrete Filled Square Steel Tubular Short Columns subjected to Cyclic Shearing Force and Constant Axial Force". *Transactions, Architectural Institute of Japan*. **353(July)**, 81-89, Tokyo, Japan.
- Sakino, K. and Tomii, M. (1981). "Hysteretic Behaviour of Concrete Filled Square Shell Tubular Beam-Columns Failed in Flexure". *Transactions, Japan Concrete Institute*. **3**, 439-446, Tokyo, Japan.
- Shakir-Khalil, H. and Zeghiche, J. (1989). "Experimental Behaviour of Concrete-Filled Rolled Rectangular Hollow Section Columns". *The Structural Engineer*. **67:19**, 346-353.
- Shakir-Khalil, H. and Mouli, M. (1990). "Further Tests on Concrete-Filled Rectangular Hollow Section Columns". *The Structural Engineer*. **68:20**, 405-413.
- Shanmugam, N.E. and Lakshmi, B. (2001). "State of the Art Report on Steel-Concrete Composite Columns". *Journal of Constructional Steel Research*. **57**, 1041-1080.
- Sharpe, R.D. and Skinner, R.I. (1983). "The Seismic Design of an Industrial Chimney with Rocking Base". *Bulletin of the New Zealand National Society for Earthquake Engineering*, **16:2**, 98-106.
- Solberg, K. Mashiko, N., Mander, J.B., and Dhakal, R.P. (2009). "Performance of a Damage-Protected Highway Bridge Pier Subjected to Bidirectional Earthquake Attack". *ASCE Journal of Structural Engineering*. **135:5**, 469-478.
- Stone, W.C., Cheok, G.S., and Stanton, J.F. (1995). "Performance of Hybrid Moment-Resisting Precast Beam-Column Concrete Connections Subjected to Cyclic Loading". *ACI Structural Journal*. **91:2**, 229-249.
- Suzuki, H. and Kato, B. (1981). "Shear Strength of Concrete Filled Box Elements". *Proceedings of the Conference on Joints in Structural Steelwork*, Middlesborough, England.
- Taylor, R.G. (1977). "The Nonlinear Seismic Response of Tall Shear Wall Structures". *Ph.D. Thesis*, Department of Civil Engineering, University of Canterbury, Christchurch, New Zealand.
- Tobolski, M.J. (2010). "Improving the Design and Performance of Concrete Bridges in Seismic Regions". *Ph.D. Thesis*, Department of Structural Engineering, University of California at San Diego, La Jolla, CA.
- Toranzo, L.A., Restrepo, J.I., Mander, J.B., and Carr, A.J. (2009). "Shake-Table Tests of

- Confined-Masonry Rocking Walls with Supplementary Hysteretic Damping”. *Journal of Earthquake Engineering*. **13:6**, 882-898.
- Uy, B. and Patil, S.B. (1996). “Concrete-Filled High Strength Steel Box Columns for Tall Buildings: Behaviour and Design”. *The Structural Design of Tall Buildings*. **5**, 75-93.
- Virdi, K.S. and Dowling, P.J. (1973). “The Ultimate Strength of Composite Columns in Biaxial Bending”. *Proceedings of the Institution of Civil Engineers, Part 2*. **55(Mar.)**, 251-272.
- Vulcano, A. and Bertero, V.V. (1987). “Analytical Models for Predicting the Lateral Response of RC Shear Walls: Evaluation of Their Reliability”. *Report No. UCB/EERC-87/19*, Earthquake Engineering Research Center, University of California at Berkeley, Berkeley, CA.
- Wang, Y.C. and Moore, D.B. (1997). “A Design Method for Concrete-Filled Hollow Section Composite Columns”. *The Structural Engineer*. **75:21**, 368-372.